Summer 2012

# Nanowire giant magnetoresistance thin films for magnetic sensors

Bryan Cox

# NANOWIRE GIANT MAGNETORESISTANCE

# THIN FILMS FOR MAGNETIC SENSORS

by

Bryan Cox, B.S. EE, M.S. Engr.

A Dissertation Presented in Partial Fulfillment
of the Requirements for the Degree
Doctor of Philosophy in Engineering

COLLEGE OF ENGINEERING AND SCIENCE
LOUISIANA TECH UNIVERSITY

August 2012

UMI Number: 3580368

UMI

Dissertation Publishing

UMI 3580368

ProQuest

# LOUISIANA TECH UNIVERSITY

## THE GRADUATE SCHOOL

August 16, 2012
_____
Date

     We hereby recommend that the dissertation prepared under our supervision

by **Bryan Cox**
_____

entitled _____

**Nanowire Giant Magnetoresistance Thin Films for Magnetic Sensors**
_____

_____

_____

be accepted in partial fulfillment of the requirements for the Degree of
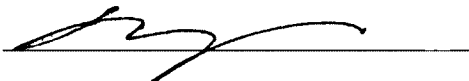
**PhD Engineering**
_____

_____
Supervisor of Dissertation Research

_____
Head of Department

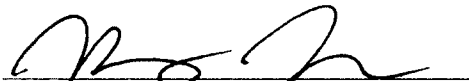**College of Engineering and Science**
_____
Department

Recommendation concurred in:

_____

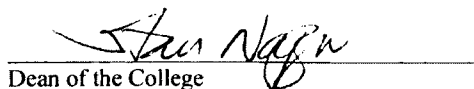_____

Advisory Committee

_____

**Approved:**
_____
Director of Graduate Studies

**Approved:**
_____
Dean of the Graduate School

_____
Dean of the College

# ABSTRACT

This dissertation details a novel method to fabricate magnetic sensors using nanowire giant magnetoresistance (GMR) thin films. In 1988, Albert Fert and Peter Grünberg both independently discovered a new physical phenomenon called GMR. GMR is a quantum mechanical effect found in thin film materials that are composed of alternating nanoscale ferromagnetic and non-magnetic conductive layers. When a GMR material is in the presence of a magnetic field, a change in electrical resistance is observed. The GMR effect has been utilized to produce magnetic sensors that have been used in a variety of applications, such as computer hard drive read heads, position sensors, proximity detectors, and biosensing devices. Although there are other types of magnetic sensors that have greater sensitivity and lower magnetic detection limits, such as the SQUID magnetometer, GMR sensors have more commercial potential due to their small size, low power requirements, low fabrication cost, and reproducible operation in very narrow magnetic ranges.

The purpose of this research is to create nanowire GMR thin films for magnetic sensing applications. Using an electrodeposition technique, CoNiFeCu/Cu multilayer nanowires are fabricated inside of anodic aluminum oxide (AAO) templates. Parameters, such as electrolyte concentration, current density, and deposition times were studied in a previous study to determine the values that achieve the highest change in resistance in an applied magnetic field. After GMR nanowires are fabricated inside the template, they are

removed and transferred to flexible and transparent polyethylene terephthalate (PET)

substrates using a variety of techniques including vacuum filtration and metering rod

methods. This will be the first study on GMR nanowire thin films for magnetic sensors

that are inexpensive, transparent and flexible.

# APPROVAL FOR SCHOLARLY DISSEMINATION

The author grants to the Prescott Memorial Library of Louisiana Tech University the right to reproduce, by appropriate methods, upon request, any or all portions of this Dissertation. It is understood that "proper request" consists of the agreement, on the part of the requesting party, that said reproduction is for his personal use and that subsequent reproduction will not occur without written approval of the author of this Dissertation. Further, any portions of the Dissertation used in books, papers, and other works must be appropriately referenced to this Dissertation.

Finally, the author of this Dissertation reserves the right to publish freely, in the literature, at any time, any or all portions of this Dissertation.

Author _Bryan Cox_

Date _8-16-2012_

# DEDICATION

I would like to dedicate this work to my Mom, Dad, Grandparents, and family who have

supported me throughout my educational journey and life.

# TABLE OF CONTENTS

# LIST OF TABLES

# LIST OF FIGURES

# ACKNOWLEDGEMENTS

I would like to thank my advisor, Dr. Niel Crews, for believing in me and for providing needed advice and support as well as him giving me the opportunity to work on some exciting research projects that allowed me to gain valuable skills as an engineer.

I especially would like to thank Dr. Long Que, Dr. Hisham Hegab, Dr. Chad O'Neal, Dr. Erica Murray and Dr. Despina Davis for agreeing to serve on my advisory committee and providing guidance and input for my research. I acknowledge Dr. Alfred Gunasekaran and Ms. Deborah Wood along with the rest of the Institute of Micromanufacturing (IFM) staff and faculty for their assistance throughout my time at Louisiana Tech University. Thanks to my colleagues Mr. Ilija Pjescic, Mr. James Haywood, Mr. Collin Tranter and Mr. Prajon Shakya for all of their help and suggestions.

# CHAPTER 1

## INTRODUCTION

### 1.1 Background

Over the last two decades, the research of micro/nanotechnology has increased almost exponentially as vast potential benefits are being realized along with new supporting technology that helps make research possible [1]. As the appeal and interest grows for nanotechnology and microtechnology to be introduced into practical applications, researchers are discovering new phenomenons and producing new micro/nanostructures to create new technologies. Many analysts predict that in the future micro/nanotechnology will significantly change how society operates [2].

In 1988, Albert Fert and Peter Grünberg, independently discovered a new physical effect named giant magnetoresistance (GMR) [3]. Using this effect, they were able to construct material systems that exhibited large changes in electrical resistances in weak magnetic fields. At first, this sensing effect was promising for magnetic sensors in computer read heads to satisfy the ever-increasing demand of high density data storage, but later on other application areas also found this effect valuable [4-6]. Due to their sensing versatility, GMR materials make good candidates as magnetic field sensors, magnetometers, compass systems, and position detection devices.

GMR materials can be fabricated from most of the thin film fabrication techniques, which can be broadly classified into physical and chemical processes.

Physical processes entail emitting atoms from a target by means of high-speed electrons, ions, or molecules and then directing the target material to a substrate. Alternatively, chemical and electrochemical processes are characterized by the occurrence of a chemical reaction at the substrate surface. Each fabrication method has advantages and disadvantages, with both the cost of fabrication and quality of the GMR material being affected by the choice. At room temperatures, GMR materials can have resistance changes up to 70 %; however, GMR materials at very low temperatures (~4.2 K) can experience resistance changes close to 100 %.

There are two types of GMR geometries, which are named current in plane (CIP) and current perpendicular to plane (CPP). Each geometry has a different quantum mechanical effect that changes the probability of conduction electrons scattering throughout their layers. CIP GMR describes a geometry whereby the magnetic field must be applied in the same direction as the current flow for a change in resistance to be experienced by the material and the mean free path of conduction electrons determines the amount of resistance change. Alternatively, CPP GMR refers to a geometry that requires multilayers in high aspect ratio configurations. With CPP GMR, a magnetic field must be applied perpendicular to the current flow for resistance changes in magnetic fields, where by the spin-flip diffusion length of conduction electrons influences the magnitude of the resistance change. CPP GMR performance is partially a function of the number of alternating material layers with a higher number of layers giving higher changes in resistances in magnetic fields. Researchers have shown that CPP GMR can have higher changes in resistances at lower magnetic field than their CIP GMR counterparts [7, 8].

For CIP and CPP GMR, the uniformity of the layers is critical to sensor performance. Therefore, the layers are typically formed on silicon substrates using high-precision sputtering deposition techniques. These fabrication methods are suitable for parallel manufacture of small sensors. However, other fabrication methods have been explored such as electrodeposition. Electrodeposition provides a greater versatility regarding template size and a more economical way to produce large area GMR sensors. Electrodeposition fabrication techniques have demonstrated poor performance with CIP GMR, due to a poor control over layer uniformity and the fact that CIP GMR requires very small layers (~2 nm) [9, 10]. However, CPP GMR makes a good candidate for electrodeposition fabrication because the layers can be considerably larger (up to ~50 nm) than CIP GMR and a large number of layers can be created in high aspect ratio structures, such as those found in nanowires, to offset any GMR degradation due to non-uniformity of the multilayers.

The great majority of CPP GMR nanowire research considers the nanowires from within their template. Unfortunately, this approach limits the utility of these sensors. This also means geometrical scaling up in geometry has an exponential cost increase with larger sensor size. In addition, all of the CPP GMR nanowires are essentially in a parallel electrical configuration while within the fabrication template. This creates a very low sensor resistance, which has a severely detrimental effect on the measurable GMR effect even when percent changes in resistance exceed those of their CIP counterparts [11].

## 1.2 Research Goal

The purpose of this research is to produce GMR nanowires that will be used to create thin films for magnetic sensors. Using a pulsed electrodeposition technique, CoNiFeCu/Cu multilayer nanowires are fabricated inside of anodic aluminum oxide (AAO) templates. Parameters, such as electrolyte concentration, current density, and deposition times were studied previously to determine the values that allowed the GMR nanowires to achieve the highest change in resistance in a magnetic field. After the GMR nanowires are fabricated inside the template, they are removed and transferred to flexible and transparent PET substrates using a variety of techniques including vacuum filtration and metering rod methods. Magnetic sensors created by these techniques can be used to construct large inexpensive magnetic sensing arrays for a variety of applications.

The change in resistance of the magnetic sensors was determined by placing nanowire GMR thin film samples into a hall effect system capable of generating a variable magnetic field and measuring the thin films sheet resistance. To characterize the thin film visually, a scanning electron microscope (SEM) was used to determine the density and integrity of the nanowire network. Percolation theory was used to create a mathematical model to determine the optimal density of GMR nanowires for conductivity. The goals of this research were to create magnetic sensors that are inexpensive to fabricate, optically transparent, flexible, with versatile shapes and sizes.

CHAPTER 2

MAGNETORESISTANCE

## 2.1 Magnetoresistance Overview

Magnetoresistance (MR) is the ability of a material to change its electrical resistance in the presence of a magnetic field. William Thomson first revealed the effect in 1856 while experimenting with iron and electrical currents [12]. He discovered that when current flow was parallel with a magnetic field a drop in electrical resistance was observed, however, when the magnetic field was turned 90° perpendicular to the current flow, the resistance returned to normal.

Magnetic sensors based on the MR effect can measure the strengths of magnetic fields and the relative direction of the fields. One of the most significant applications of MR sensors is their incorporation into read heads for magnetic recording devices [13, 14]. Five distinct types of MR are ordinary magnetoresistance (OMR), anisotropic magnetoresistance (AMR), giant magnetoresistance (GMR), tunneling magnetoresistance (TMR) and colossal magnetoresistance (CMR).

## 2.1 Ordinary Magnetoresistance (OMR)

The OMR effect is found in non-magnetic metals and is considerably small at low magnetic fields. Changes in resistivity, $\Delta\rho$, are positive for magnetic fields that are applied both parallel and perpendicular relative to the current direction. OMR changes in

resistance are relatively smaller than the other types of magnetoresistance. There are three different mechanisms for the OMR effect, depending on the structure of the electron orbitals at the Fermi surfaces.

i.  Metals with closed Fermi surfaces have their electrons constrained to their orbit in $k$ space and the magnetic field has the ability to increase the cyclotron frequency of the electron in its closed orbit. Metals that exhibit this effect include In, Al, Na, and Li.

ii. When a metal has an equal number of electrons and holes, their magnetoresistance increases with an increasing magnetic field up to the highest known magnetic field levels able to be attained. The magnetoresistance is not dependent on the crystallographic orientation of the metal lattice. Metals with this behavior include Bi, Sb, W, and Mo.

iii. When metals have Fermi surfaces with open orbits in some crystallographic directions, a large magnetoresistance effect will be observed for magnetic fields applied in the open directions, and the resistance will saturate in the closed directions. Metals with this characteristic are Cu, Ag, Au, Mg, An, Cd, Ga, Tl, Sn, Pb, and Pt.

## 2.2 Anisotropic Magnetoresistance (AMR)

The AMR effect is seen in ferromagnetic metals and alloys, and MR effects of 2% can be obtained in low magnetic fields. As opposed to OMR, the AMR effect is anisotropic, which means that when a magnetic field is applied parallel to the current flow there is an increase in the resistivity ($\rho_{\parallel}$) of the metal and when a magnetic field is

applied perpendicular to the current flow, there is a decrease in the resistivity ($\rho_T$) of the metal. Figure 1 gives a visual representation of this concept.
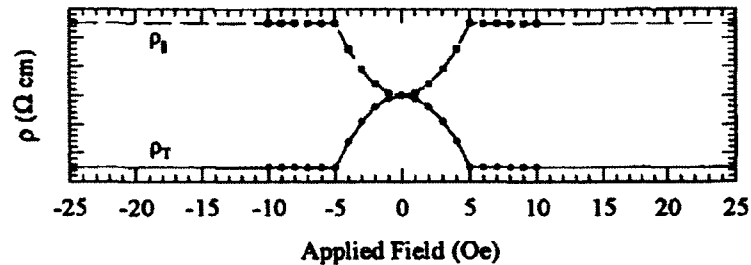


Figure 1: Visual representation of anisotropic magnetoresistance for a magnetic field applied parallel ($\rho_{\parallel}$) and perpendicular ($\rho_T$) to the current direction [13]

The change in resistivities arises from the change in the probabilities of conduction electrons scattering throughout the metals due to spin orbit coupling. When a magnetic field is applied to a metal, there is a slight deformation of the electron clouds throughout the atoms that make up the metal. This deformation changes the amount of scattering the conduction electrons experiences as they transverse the lattice.

Early on, AMR based magnetic sensors were widely used in recording heads for systems, such as audio and video cassette players. Normally, the sensors were made from NiFe (permalloy) and possessed a 2% resistance change at low saturation fields between 5 to 10 Oe.

## 2.3 Giant Magnetoresistance (GMR)

The GMR effect is seen in antiferromagnetically coupled multilayers and can have up to 70% MR at room temperature [15]. The layers consist of magnetic metals separated by non-magnetic metal layers. When no magnetic field is applied to the layers, the magnetic layers couple through the non-magnetic layers in an anitferromagnetic configuration, if the thickness of the non-magnetic layers is small enough. The resistivity

of the GMR material is determined by the amount of scattering at the interfaces of the metal layers. Conduction electrons experience relatively high probabilities of scattering when the magnetic layers are antiferromagnetically coupled. When a magnetic field is applied to the multilayers to force the layers into a ferromagnetic configuration, only half of the conduction electrons experience strong scattering, and the other half have weak scattering with an overall decrease in the resistance of the GMR material. The use of GMR in computer read heads led to an increase in storage densities from 1 gigabyte per square inch with AMR read heads to over 20 gigabyte per square inch with GMR read heads [16].

## 2.4 Tunneling Magnetoresistance (TMR)

The TMR effect is observed in material systems that have two magnetic layers separated by a thin insulating layer. When an external magnetic field is used to align the magnetic layers, electrons have a greater probability of tunneling through the insulating material. The TMR effect was first discovered in 1975 by M. Jullière at the University of Rennes in France [17]. Jullière used Fe/Ge-O/Co junctions at 4.2 K to create changes in resistance of 14%. Figure 2 illustrates the TMR concept.

Magnetic layer →
Insulating layer →

(a)                (b)
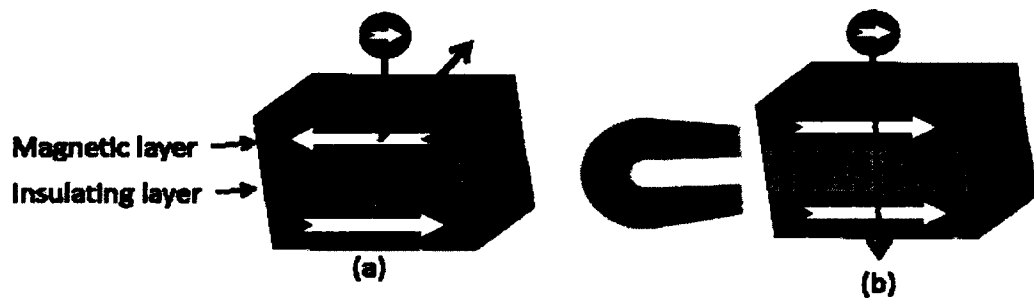
Figure 2: Schematic showing the TMR effect (a) the magnetic layers are not aligned leading to low tunneling currents and high resistance (b) magnetic layers are aligned creating a higher probability of electrons tunneling and a lower resistance of the TMR material

## 2.5 Colossal Magnetoresistance (CMR)

CMR is a material property seen in mostly manganese-based perovskite oxides that have extremely large % MR changes (upwards of 99.9%). CMR was first discovered in 1950 by G.H. Jonker and J.H van Santen in mixed-valance peroskite magnanities [18]. The resistivity of the CMR material undergoes a low temperature transition from an insulating to a metallic behavior. The colossal magnetoresistance effect is observed in the metallic region. The CMR effect differs from the mechanisms that govern the GMR effect. In CMR materials, conductivity occurs due to electron hopping (metallic ions switching states) instead of metallic conduction, as seen in GMR materials [13].

The CMR effect is more pronounced at certain critical temperatures ($T_C$). When a magnetic field is applied to a CMR material, the peak resistivity of the material shifts to a higher temperature, but there is a decrease in the maximum peak resistivity. Figure 3 highlights this concept.
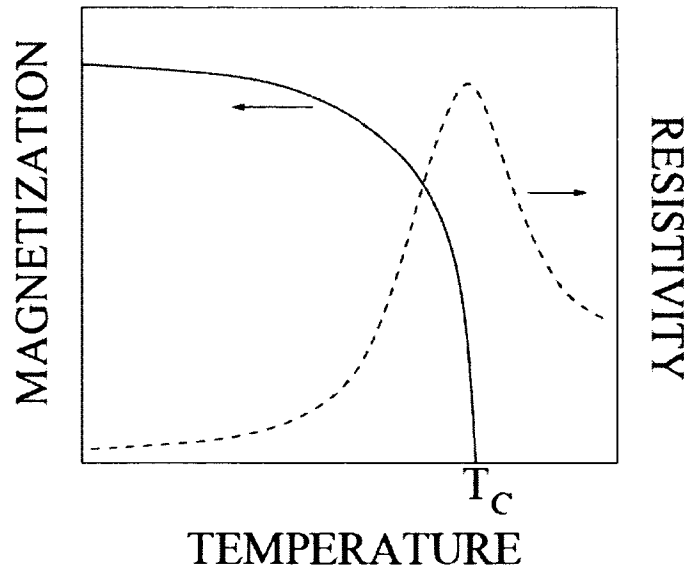


Figure 3: Graph showing how temperature affects the resistivity of CMR materials. When a magnetic field is applied, the peak on the resistivity moves toward a higher temperature and noticeably decreases in height [14]

CMR has a tremendous upside with MR ratio magnitudes larger than GMR, but CMR has many technical hurdles that must be overcome before it can be used in commercial magnetic sensors. CMR thin films can only be grown epitaxially, which is a slow and expensive process. In addition, high % MR values can only be achieved at certain critical temperatures and raising the critical temperature close to room temperature lowers the MR drastically, which mean large impractical magnetic fields (4 T) are needed for large MR ratios.

# CHAPTER 3

# GMR OVERVIEW

## 3.1 GMR Literature Review

Baibich's research group was the first to observe the GMR effect in Fe(30 Å)/Cr(9 Å) superlattices prepared by molecular beam epitaxy on GaAs substrates [19]. He proposed that the magnetoresistance arises from spin-dependent transmissions of the conduction electrons through the thin Cr layers. Electrical current consists of two different conduction channels that carry either spin-up or spin-down s-p electrons, respectively [20]. Normally, the resistivities of the two conduction channels are equal in GMR materials when there is no magnetic field present, however, the resistivities of two conduction channels change when an external magnetic field is present. The conduction channel shift in resistance is due to a magnetic field ability to change the probability of an electron scattering throughout the conduction channels inside GMR materials. For instance, both spin-up and spin-down electrons will experience the same amount of scattering as they travel throughout the layers of a GMR material when no magnetic field is present. However, when a magnetic field is applied, the ferromagnetic layer electrons in the GMR material will orientate themselves parallel with either the spin-up or spin-down conduction electrons, decreasing their probability of the electrons scattering. While the magnetic field decreases one electron spin probability of scattering, there is an increase in the other electron spin probability. The change in electron scattering

11

probability creates an overall lower resistance to current passing through the multilayered material [19]. Figure 4 illustrates the two-conduction channel concept in GMR materials with the top two resistors in (a) and (b) representing the spin-up conduction channel and the bottom two resistors representing the spin-down channel.

**No Magnetic Field**          **External Magnetic Field**



(a)                                    (b)
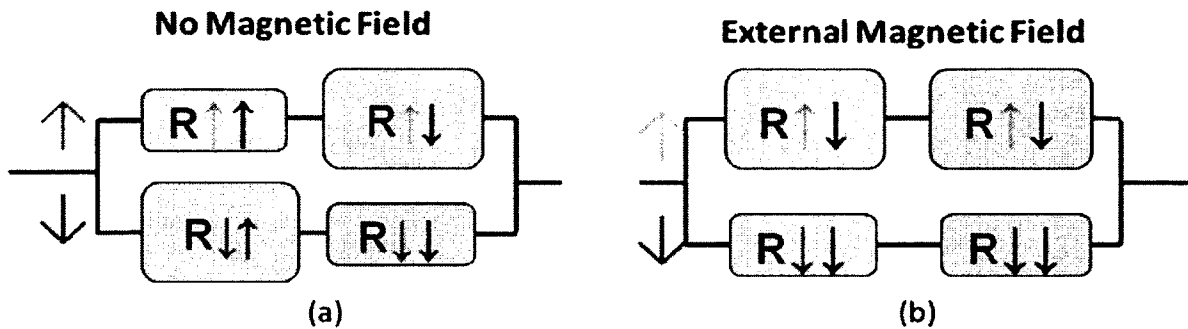
Figure 4: Electrical schematic representation of GMR material (a) with no magnetic field, spin up and spin down electrons experience equal resistance (b) with an external magnetic field present, spin up electrons experience less resistance than spin down electrons

It is important to note that for thicker magnetic layers and higher temperatures, the likelihood of spin-flip scattering within the channels increases, and the two conduction channels start to combine, therefore weakening the magnetoresistance effect.

A number of research groups have fabricated and characterized GMR with great success. With a focus on thin film magnetic layers inserted in-between non-magnetic layers, Parkin reviewed the magnetoresistance effect in layered structures [21]. In the review, the author calls attention to the layered material requirements for magnetic data storage applications, which are magnetic stability against increased temperatures, no electromigration at high current density usage, and minimal environmental corrosion. The review also notes that a decrease in GMR is observed when the alternating magnetic layers were not completely antiferromagnetically coupled, which occurs when the layer

sizes are too large or not uniform. At room temperature, 70% GMR was reported for Co/Cu thin films obtained by DC magnetron sputtering. Co/Cu multilayers have some of the largest values of GMR for any materials systems due to the large distinctions in spin-dependent scattering of majority and minority carriers at the Co/Cu interfaces.

As the evolution of GMR research evolved, a new more affordable technique of GMR fabrication was developed to create multilayer thin films using electrodeposition techniques. Ross reviewed multilayer GMR fabricated using electrodeposition techniques and found that the capability to tailor the deposit composition and crystallographic structures in electrodepositited GMR yielded advantages over GMR fabricated using other mechanisms [10]. Electrodeposited GMR also eliminated the need for ultra high vacuum, which is a requirement for other fabrication methods. Ross established that the electrolyte composition, pH, agitation and current regime all affect the formation of the multilayers during the fabrication process. In the US, two leading groups, E. J. Podlaha [22] and G. Zangari [23] focused on the electrodeposition of multilayered thin films for GMR applications and reported 11% GMR in CoNi/Cu and 9% GMR in CoNiFe/Cu multilayered systems.

## 3.2 GMR Structures and Measurements

Current in plane (CIP) and current perpendicular to plane (CPP) are two types of GMR configurations, each having a different orientation of the current flow with respect to the alignment of the multilayers and the application of a magnetic field for %MR measurements. Both configurations of GMR also have a different type of scattering mechanism for conduction electrons in its layered structures.

### 3.2.1 Current in Plane (CIP) GMR

Current in plane (CIP) multilayer GMR receives its name from the fact that resistance measurements are taken by applying a magnetic field in the plane or in line with the current traveling through the GMR material. It consists of nonmagnetic conductive layers sandwiched between magnetic conductive layers. The nonmagnetic conductive layers are made of materials that have a higher conductivity than the magnetic conductive layers. The multilayer thicknesses must be small, similar to the mean free path of an electron (~2 nm), in order for electrons to be scattered due to the antiferromagnetically coupled layers and experience a higher resistance than if the layers were not coupled. Figure 5 shows CIP GMR with no magnetic field (a) and with a magnetic field applied parallel (b) to the current flow.
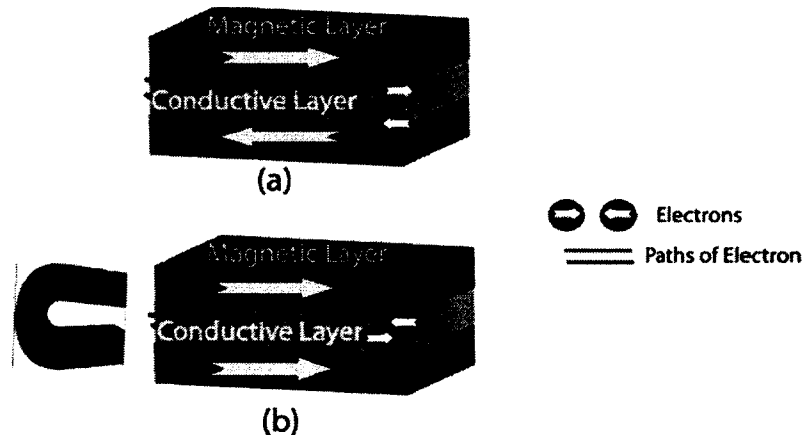


Figure 5: (a) CIP thin film GMR material with no magnetic field applied, both electron types have high scattering (b) CIP GMR with a magnetic field applied parallel to the current. Notice that one electron type has less scattering, while the other has increased scattering

When the magnetic layers are not aligned, the probability of an electron scattering is higher. An external magnetic field can align the magnetic layers and in the process

reduce the probability of one type of the electrons scattering, and therefore the material will have a lower resistance, as seen in Figure 5 (b).

### 3.2.2 Current Perpendicular (CPP) GMR

Current perpendicular to plane (CPP) GMR resistance measurements are taken by applying a magnetic field perpendicular to the current traveling through the GMR material. CPP GMR is common in high aspect ratio materials, such as nanowires. Figure 6 (a) shows how CPP GMR electrons respond when no magnetic field is present and part (b) shows what happens when the layers are aligned due to a magnetic field being applied perpendicular to the layers.
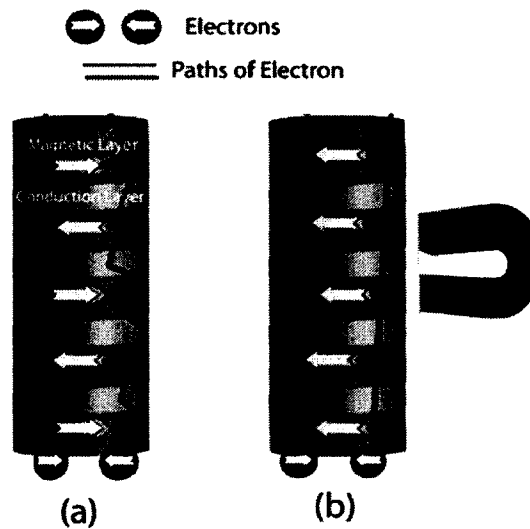


Figure 6: (a) CPP nanowire GMR material with no magnetic field applied. Both conduction electrons have equal scattering throughout the layers (b) CPP nanowire GMR material with magnetic field applied perpendicular to the current. One electron type has a increased probability of scattering, while the other electron type a decreased probability of scattering

Unlike CIP GMR, which is limited by the mean free path of an electron, the spin diffusion length (~ 50 nm) of electrons confines CPP %MR measurements. This means that the layers can be thicker in CPP GMR versus CIP GMR, making CPP GMR more

popular with electrodeposition fabrication techniques. The greater the amount of multilayers in CPP GMR, the higher the %MR will be. Table 1 compares CIP and CPP GMR.

Table 1: Comparison of CIP and CPP GMR configurations

|  | CIP | CPP |
|---|---|---|
| **Measurement orientation** | Current flow parallel to magnetic field | Current flow perpendicular to magnetic field |
| **Limiting effect** | Mean free path of electrons | Spin diffusion length of electrons |
| **Layer thickness max** | ~2 nm | ~50 nm |
| **Fabrication configuration** | Thin film materials | High aspect ratios materials |

### 3.3 GMR Fabrication Techniques

GMR can be fabricated from any one of the many thin film fabrication techniques, which can be broadly classified into physical and chemical processes. Figure 7 shows several multilayer thin film deposition techniques. Physical deposition processes entail emitting atoms from a target by means of high-speed electrons, ions, or molecules and then directing the material to a substrate. Alternatively, chemical and electrochemical processes are characterized by the occurrence of chemical reaction at the substrate surface. Each fabrication method has its advantages and disadvantages, with the cost of fabrication and quality of the GMR materials both being affected by the fabrication method.
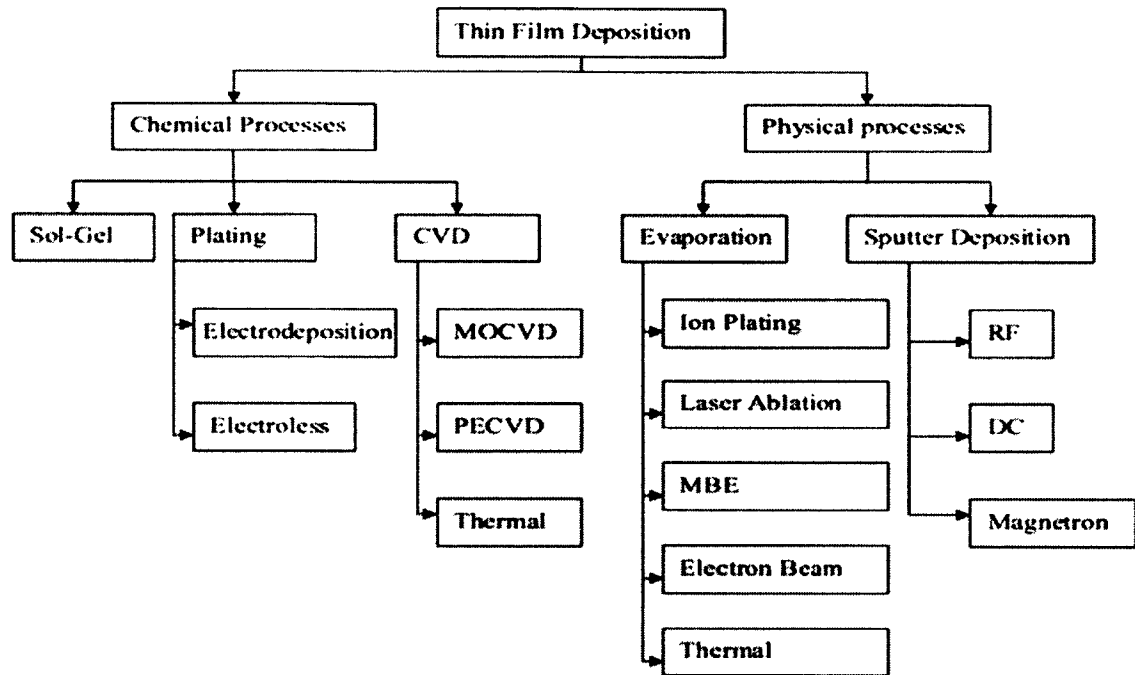
Figure 7: Classification of multilayered thin film deposition processes [24]

### 3.3.1 Physical Methods

*Molecular Beam Epitaxy*

Molecular Bean Epitaxy (MBE) was introduced in the 1970s to make high quality films of semiconductors, metals, or insulators. Either an effusion cell or electron heated metal is used to heat the atoms, molecules, or clusters of extremely pure form until they evaporate and sputter onto a substrate at the bottom of a MBE chamber. Figure 8 shows an example schematic of a MBE system. Multiple materials each having its own effusion cell can be sputtered onto the substrate with great precision. The materials take on the crystal orientation of the substrate producing highly ordered layers of atoms.
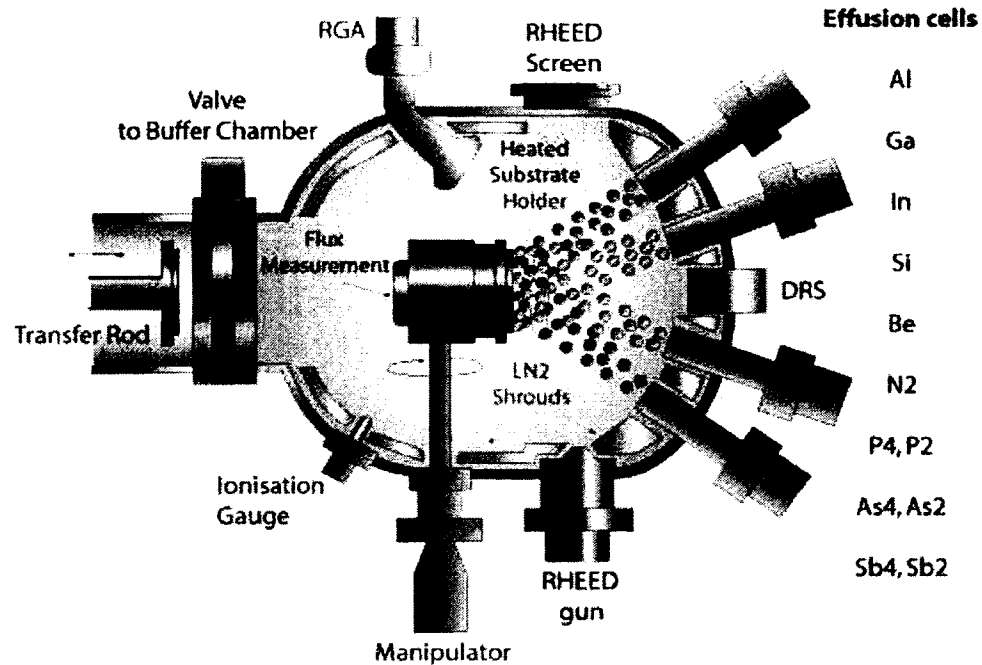
Figure 8: A schematic diagram of a MBE system [25]

The components can be sputtered one at a time or multiple components can be sputtered together. Being able to control precisely which components make up the film and exact deposition rates make MBE great for CIP GMR thin films.

MBE only works when the mean free path $\lambda$ of atoms, molecules, or clusters is larger than the geometric dimension of the chamber. This is possible with the use of ultrahigh vacuums (approximately $10^{-10}$ torr) used in MBE chambers. The ultra high vacuum also ensures that the environment of the chamber is contaminant-free and gives fabricators the ability to monitor the film growth in real time using electron beam techniques, such as reflection high-energy electron diffraction (RHEED), low-energy electron diffraction (LEED) and various compositions (Auger electron spectroscopy and X-ray photoelectron spectroscopy). MBE deposition is relatively slow compared with other deposition techniques with growth rates approximately 1 $\mu m \cdot h^{-1}$.

Researchers have tried different approaches to decrease the number of defects in the lattices that make up the multilayers in GMR grown by MBE. Camarero et al. [26] experimented with adding Pb as a surfactant that mediated modification of the magnetic properties of Co/Cu superlattices. He found that the surfactants improved the magnetic properties of the thin Co films and Co/Cu superlattices by substantially reducing the layer roughness and eliminating structural defects, such as twins and stacking faults.

## DC Magnetron Sputtering

Another common physical method for obtaining layers in GMR materials is DC magnetron sputtering. This method entails bombarding a target made of the material to be sputtered with high-energy gas particles and ejecting atoms or molecules on to a substrate above the target in a vacuum chamber. The sputtered atoms ejected from the target have a wide variety of energy distributions, usually in the tens of eV. The molecular weights of the gas particles are usually close to the material that is being sputtered, so for lighter materials neon gas is used while for heavier materials krypton or xenon is used for sputtering. Fullerton's group studied $Ni_{81}Fe_{10}/Cu$ magnetic multilayer GMR, deposited with a four-source DC magnetron sputtering system, and achieved a maximum of 9.5% MR with a sensitivity of 0.44%/Oe [27]. Fullerton's group was able to anneal the multilayers at temperatures up to 250 °C. They observed a large change in GMR values depending on deposition conditions, such as base and deposition pressures.

### 3.3.2 Chemical Methods

*Electrodeposited Thin Films*

Electrodeposition has been examined as an alternative fabrication technique for GMR materials. In addition to the cost-effectiveness, electrodeposition can overcome the geometric restrictions of inserting metals into deep nanometric grooves. Moreover, electrodeposition methods eliminate the need for the ultra high vacuum required by vapor techniques, thus reducing fabrication cost. Ross [10] assessed electrodeposition as an alternative technique for making multilayer films, and emphasized that electrochemical fabrication techniques have the ability to tailor the deposit composition and crystallographic structure, which permits the manipulation of the deposited material mechanical properties. Compared to vapor techniques, electrodeposited CIP GMR thin films showed lower %MR values due to rough interfaces and heterogeneous growth. As stated earlier, CIP multilayers must be on the order of 2 nm, which is difficult to achieve with electrodeposition. In general, electrochemical process parameters, such as electrolyte composition, pH, agitation and current regime affected multilayer fabrication and %MR values. In the US, two leading groups, E. J. Podlaha [22] and G. Zangari [23] focused on the electrodeposition of multilayered thin films for GMR applications and reported 11% MR in CoNi/Cu and 9% MR in CoNiFe/Cu.

*Electrodeposited Nanowires*

Using a template assisted fabrication method, CPP GMR nanowires can be created using electrodeposition techniques. Theoretically, electroplated GMR nanowires yield higher %MR values than their electrodeposited thin film counterparts [28]. Aside from the fact that nanoscale materials exhibit different behavior compared to bulk

materials, nanowires are structures of enormous surface area and high aspect ratios, which give them unique properties.

European groups, including [15, 29-32] Piraux, Dubois, Ansermet, Schwarzacher, and Blondel, were the first to take advantage of the multilayer nanowire geometry for CPP GMR. Piraux et al. reported 15% CPP-GMR at room temperature in a Co/Cu system electrodeposited in the form of nanowires [32]. Dubois et al. studied NiFe/Cu nanowires and reported 78% GMR at very low temperatures [30]. Schwarzacher et al. achieved 60% GMR at room temperature for CoNi/Cu multilayered nanowires [15]. In the US, Davis and Podlaha were the first to study the CoNiFeCu quaternary system in the form of nanowires and reported 20% MR at room temperature with a 0.025 T magnetic field saturation [33].

Liu et al. [34] successfully fabricated multilayered Co/Cu nanowires with varying diameters and layer thickness. Cu and Co were deposited at -.16 V and -1.00 V, respectively, against an Ag/AgCl reference electrode. Due to the fact that Cu tends to deposit quickly at high potentials, the Cu concentration was kept very low in the electrolyte solution. A value of 11% MR was observed at room temperature and 22% MR was observed at 5 K. The Co layer was held at a constant 50 Å thickness, and the Cu layer was varied from a few to many hundreds of angstroms. When the Cu layer thicknesses reached 210 Å, there was no GMR effect observed. The vanishing of the GMR effect for larger Cu layers was due to the Cu layers starting to exceed the spin diffusion length of the conduction electrons. Figure 9 shows SEM and TEM micrographs of GMR multilayered nanowires obtained by pulsed electrodeposition techniques.
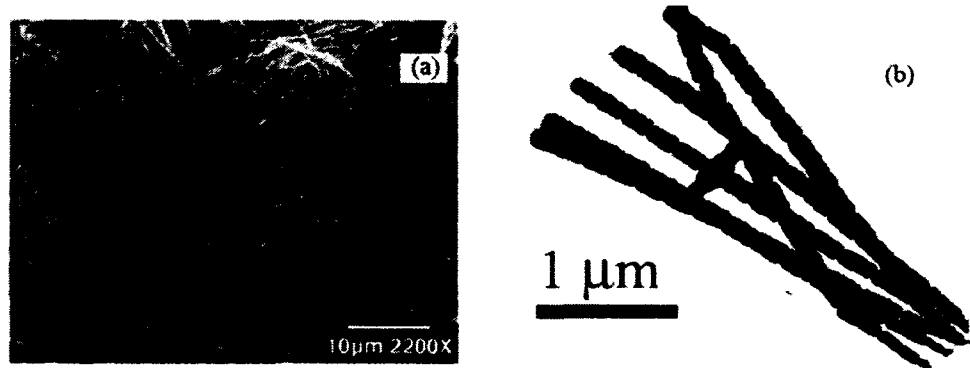
Figure 9: (a) SEM of CoNi/Cu nanowire GMR nanowires (b) TEM of CoNiFe/Cu GMR nanowires [35]

## 3.4 GMR Sensors

GMR sensors have the best combination of favorable sensor characteristics when compared with other magnetic sensors. They can be used to detect magnetic fields as small as 10 nT. Figure 10 shows a comparison of the sensitivity for a variety of magnetic sensors including GMR sensors.
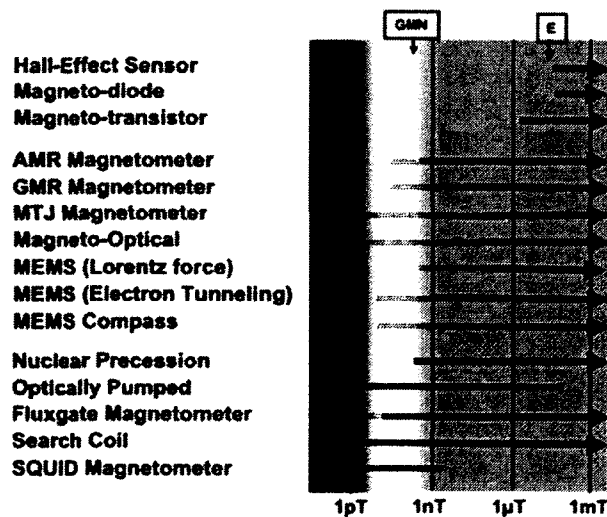


Figure 10: Chart giving the estimated sensitivity of different magnetic sensors. The symbols GMN and E indicate geomagnetic noise and the strength of Earth's magnetic field, respectively [36]

Although there are some magnetic sensors that have greater sensitivity and lower detection limits (eg. The SQUID Magnetometer), GMR sensors have more commercial potential due to their small size, low power requirements, low cost, and their operation in very narrow reproducible magnetic ranges [36]. In addition, GMR sensors have very low magnetic hysteresis, near zero voltage operation, wide range frequency response (DC to > 1 Mhz) and the ability to be incorporated into small profile packages. These qualities have helped GMR sensors to be introduced into a number of applications.

GMR materials themselves are very temperature dependent; however, simple arrangements, such as Wheatstone bridge circuits, can be applied to eliminate the temperature dependence. Many commercial GMR sensors are configured in the Wheatstone bridge configuration to decrease the temperature dependence, reduce noise, as well create a linear output for the sensor, as seen in Figure 11 [37].
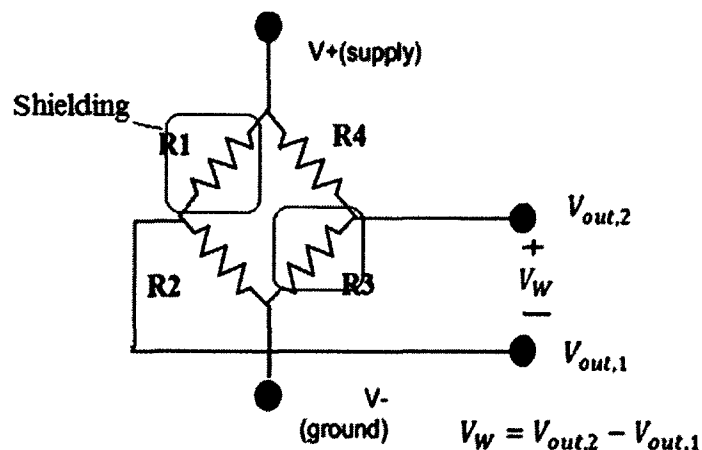


Figure 11: GMR resistors in a Wheatstone bridge configuration. Notice that two of the GMR resistors are active and the other two are shielded

In the design of GMR sensors, flux concentrators, usually made out of soft magnetic materials, can be used to concentrate the magnetic field in the preferred direction across the GMR sensors to achieve optimal sensor performance [38].

### 3.4.1 GMR Sensor Characteristics

The GMR effect is measured by applying a magnetic field to a GMR material and measuring the electrical resistance change. The equation below is used to calculate %MR, which is the percent resistance change a GMR material experiences in a magnetic field.

$$\%MR = \frac{R-R(0)}{R(0)} .$$ 

(Eq. 1)

*R* represents the GMR resistance in the presence of a magnetic field and *R(0)* represents the resistance when no magnetic field is applied. Typically, the quickest and easiest way to characterize GMR is to look at its MR curve. The curve is obtained by applying a variable magnetic field and measuring the GMR material resistance. Figure 12 shows a typical MR curve.
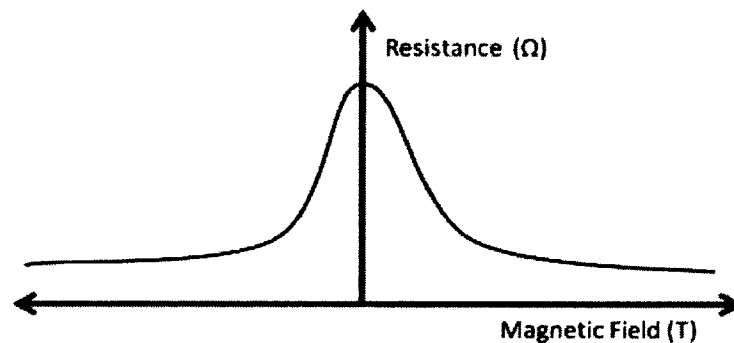
Figure 12: Typical MR Curve

The magnetic saturation point, sensitivity and hysteresis of a GMR material can be deciphered from its MR curve. A GMR material magnetic saturation point can be determined by finding the magnetic field when the slope of the MR curve approaches

zero. The maximum slope of the MR curve corresponds to the sensitivity of the GMR material. The greater the slope, the more sensitive the GMR material will be to a changing magnetic field. Hysteresis is measured by applying increasing and decreasing magnetic fields and measuring the difference in resistance at the same magnetic field values.

### 3.4.2 Types of GMR Sensors

Magnetometers and gradiometers are two types of commercially available GMR based magnetic sensors. The sensors can be packaged in a variety of ways depending on the specific application of the sensor. In nontraditional applications, such as biosensing, GMR sensors can be packaged inside a microfluidic device to detect small magnetic particles.

### *Magnetometers*

Magnetometers measure the strength or direction of a magnetic field and output a signal accordingly. A Wheatstone bridge configuration with two active GMR resistors and two shielded GMR resistors is used to eliminate temperature dependence and create a linear output. By employing flux concentrators, the sensitivity of GMR materials can be increased by a factor of 2 to 100. Figure 13 shows a typical magnetometer sensor layout on a silicon substrate from NVE Corporation.
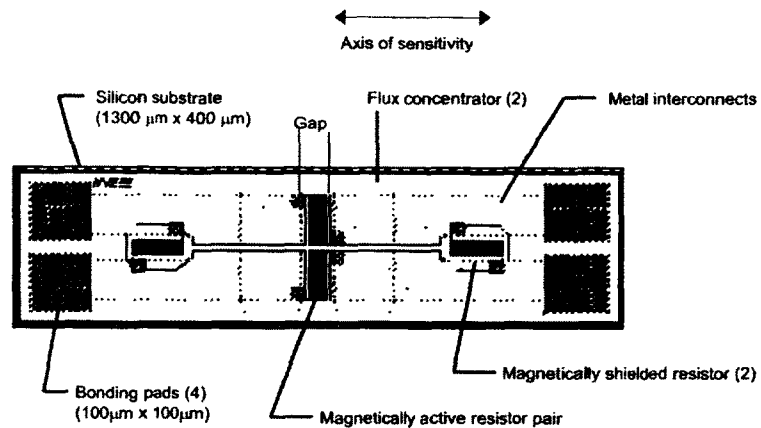
Figure 13: GMR magnetic field sensor layout from NVE Corporation [39]

## Gradiometers

Gradiometers are used to detect magnetic field gradients found between GMR resistors in a Wheatstone bridge configuration. Unlike the magnetometer, gradiometer devices are unshielded allowing all four resistors in the Wheatstone bridge to be active. The gradiometer output can be bipolar versus unipolar and can be shaped by the use of a biasing magnet or flux guides. Figure 14 shows a typical gradiometer sensor layout on a silicon substrate from NVE Corporation.
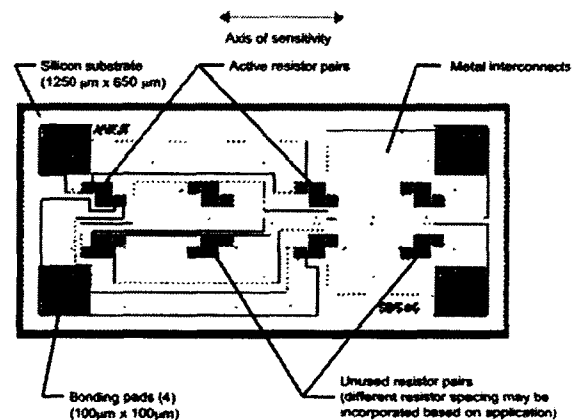


Figure 14: GMR gradiometer bridge sensor layout from NVE Corporation [39]

## 3.5 GMR Sensor Applications

Since the discovery of GMR, there has been a variety of applications developed to utilize the effect. At first, this sensing effect was promising for computer hard drive read heads to satisfy the never-ending and ever-increasing demand of high density data storage, but now many other application areas find the effect valuable [4-6]. Due to their sensing versatility, GMR materials make good candidates as magnetic field sensors, magnetometers, compass systems, and position detection devices. The sensors are designed to possess high sensitivity, enhanced signal-to-noise ratios and low mechanical wear. The next evolution of GMR sensors is their incorporation into microfluidic and medical devices for chemical and bio-sensing applications [40-42].

### 3.5.1 GMR Sensor Applications in Industry

The most basic applications of GMR sensors in the industrial setting are found in magnetic switches, proximity detectors, and linear position transducers [39]. GMR sensors make excellent switches because they are non-contact, which means they have virtually no wear and tear. GMR sensors can also successfully supply positional information of actuating components in machinery. Positional information can be obtained in one of two ways. First, a magnet can be placed on a moving component, such as a pneumatic cylinder. When the magnet comes in close proximity to a stationary GMR sensor or array of GMR sensors, located along the path of the magnet, changes in resistance can correspond to the exact position of the actuator. The second way position information can be measured is by having a stationary magnet and a moving GMR sensor. For instance, if a magnet strip is embedded in a doorway, a moving robot with a

GMR sensor can detect when it enters the doorway and take the appropriate action, as

seen in Figure 15.



Embedded Magnetic Strip

GMR Magnetic Sensor
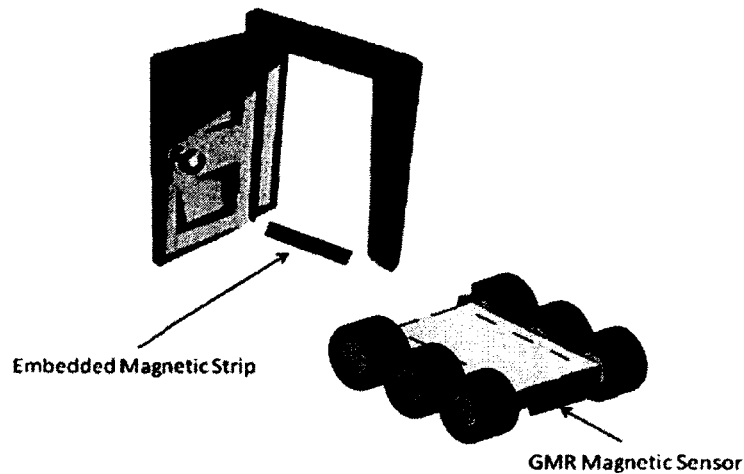
Figure 15: A GMR magnetic sensor is attached to an autonomous robot, to alert the robot
when it crosses a magnetic strip located in a doorway

Present day automobiles have numerous magnetic sensors for a variety of

functions, as seen in Figure 16. Analysts expect the number to grow in the future as more

complex systems are added to make driving easier and safer [43].
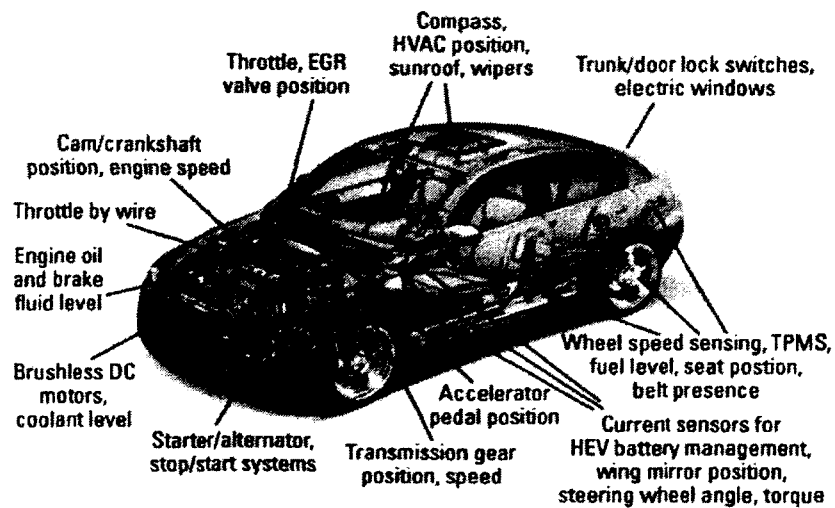


Figure 16: Magnetic sensing applications in a standard car [43]

GMR sensors are also used for rotation detection devices, such as gear tooth sensors and magnetic encoders. Gear tooth sensors are made up of a magnetic gradiometer and a magnetic field created by a biasing magnet that is influenced by the teeth of the gear, as seen in Figure 17.
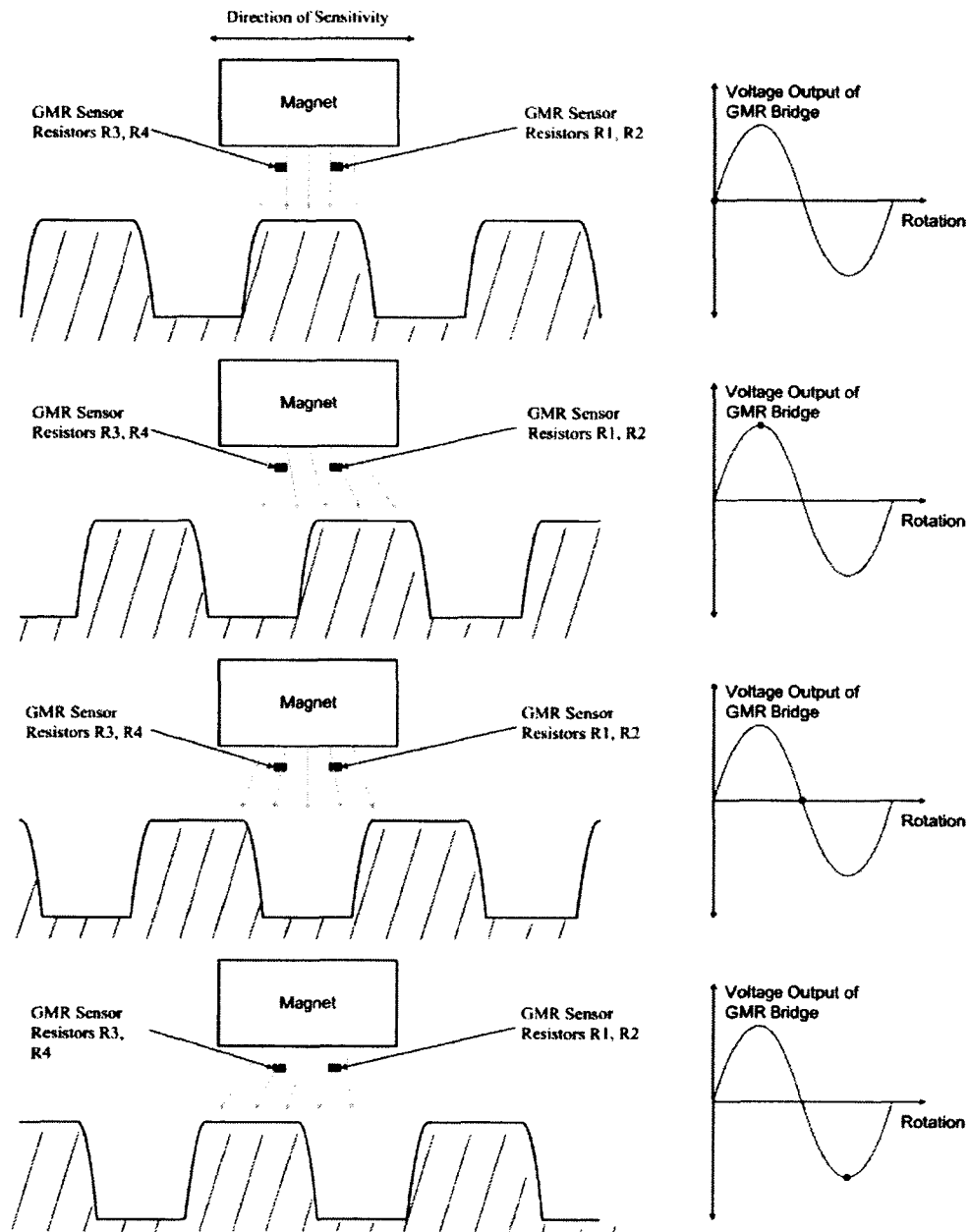


Figure 17: Gear tooth sensor detecting teeth at different points [39]

### 3.5.2 GMR Sensors in Electronics

Computer hard drive read heads have seen large improvements made in their design by incorporating GMR sensors and it is predicted that storage densities of over 300 Gbit/in$^2$ are achievable [44]. Information is stored along tracks on the hard drive disk in magnetic regions called magnetic domains [45]. At the intersection of the magnetic domains are domain walls that produce magnetic fields that extend either in a positive or negative direction outside of the magnetic domains. These domain walls are detectable by a GMR sensor located perpendicular to the magnetic field. Magnetization is stored as a "0" in negative domain walls and as a "1" in positive domain walls. Figure 18 shows a schematic representation of a GMR read head.
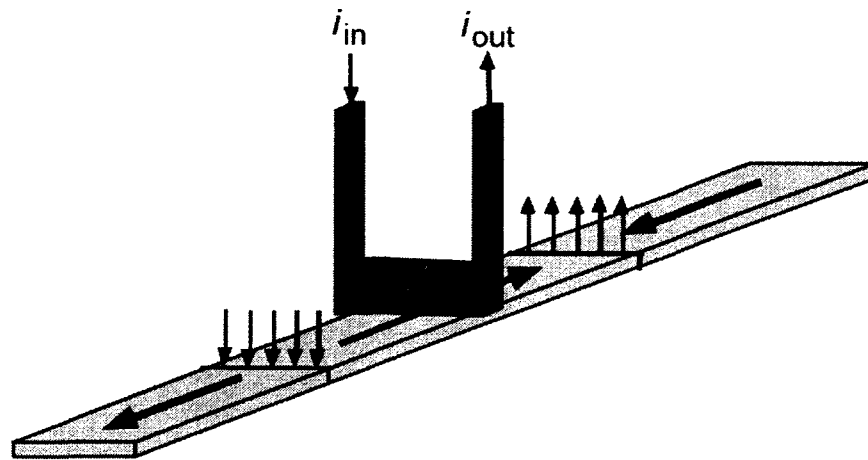


Figure 18: Schematic depiction of a GMR read head (green) that passes over recording media containing magnetized regions [46]

GMR sensors can also be used to detect the magnetic field generated from current carrying wires and PCB traces to provide a contactless and no load resistance technique for current to voltage conversion [46]. Current carrying wires produces "circles" of magnetic fields that follow the right-hand-rule, with the amplitude of the field decreasing

with a 1/r relationship as you move away from the center of the wire. Figure 19 shows an

example setup of a GMR sensor detecting a magnetic field from a current carrying wire.
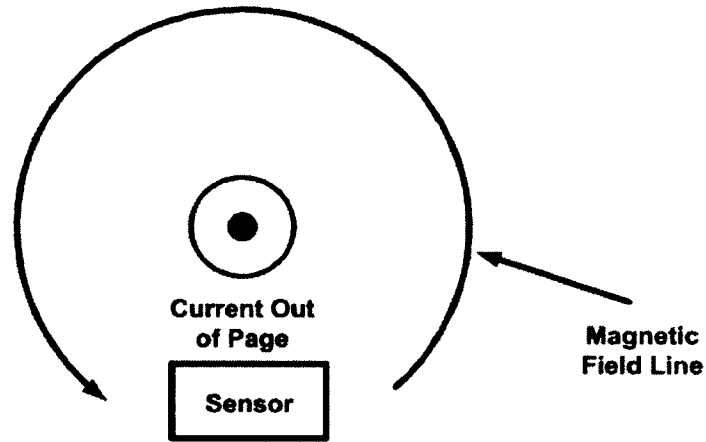


Figure 19: Magnetic field from current carrying wire and GMR sensor [45]

Other application areas for GMR sensors include magnetic stripe readers for

credit cards, currency and magnetic ink detection.
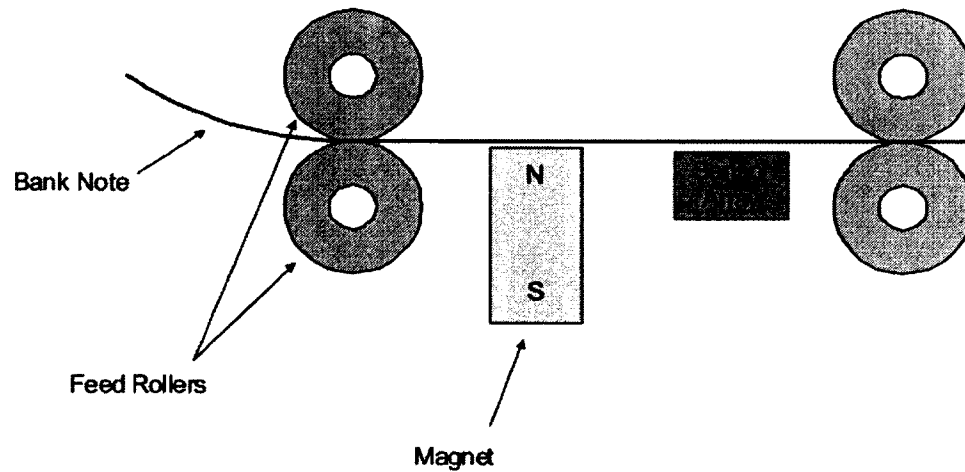


**Figure 20**: Simple illustration of currency detection with GMR sensor Array [39]

### 3.5.3 GMR Sensor Applications in Medicine

Over the past decade, the number of GMR sensor applications in medicine has increased due to the sensors small footprint, good sensitivity, low power usage, and low cost. Medical diagnostics is a research field continuously advancing modern medicine. With the help of biosensors and biochips, it is possible to build medical diagnostic devices that can detect one cancer cell out of a billion healthy cells or count the number of white blood cells in a microliter of blood [47, 48].

With advancements in magnetic labeling technology for biosening applications, GMR sensors are becoming the method of choice for detection of magnetic micro/nanoparticles due to their ability to be integrated into high density arrays for multi-analyte detection, and their high sensitivity even at room temperatures and weak magnetic fields [49]. The Naval Research Laboratory was one of the first groups to explore the use of GMR in biosensors and test the limits of detection of GMR sensors with their Bead Array Counter (BARC) system [50-53]. The BARC III was able to detect a single 3.3 $\mu$m microparticle of ($Ni_{30}Fe_{70}$), and since then, there have been a number of magnetic biosensors which have been highlighted in review articles [54, 55].

*Magnetic Immunoassays*

By placing GMR sensors in an array that allows for easy multiplexing, magnetic immunoassays (MIAs) can be created to detect multiple biochemical compounds in a complex mixture using magnetic labeling [56]. Lankvelt et al. [57] filed a patent describing this technique and proposed a GMR sensor matrix array directly integrated with a microfluidic device containing channels filled with a fluid containing target biomolecules and labeling magnetic particles. Each GMR element in the matrix was

electrically coupled in series and combined with a magnetic coil extending into the plane of the sensors. The fluid channels were placed over a contact surface covered with binding sites that captured particular target particles for detection. Lankvelt's design is promising for fabrication of robust inexpensive diagnostic chips with the capability to detect small amounts of multiple biological target particles. Figure 21 shows an illustration of biodetection scheme using GMR sensors and magnetic nanoparticles.
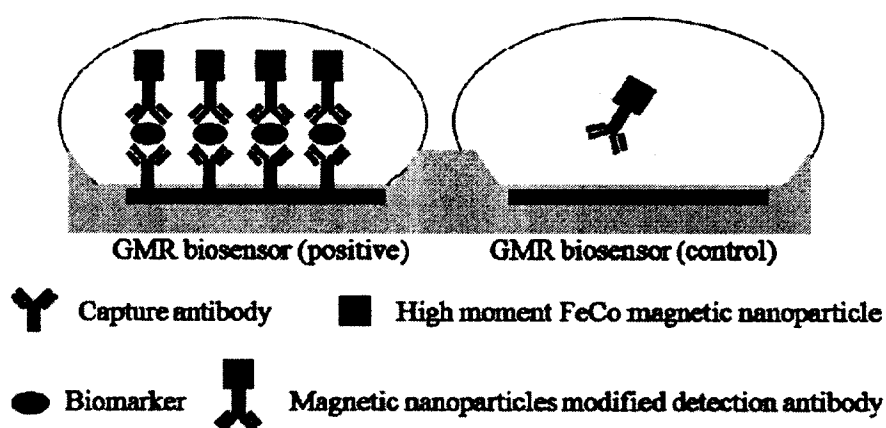


Figure 21: A biomarker detection method using GMR sensors and high magnetic moment FeCo magnetic nanoparticles [58]

*Magnetic Sorting*

In the event particles need sorting or quantifying individually, high precision sorting techniques have been developed [59]. Magnetic sorting for biomedical applications involves attaching magnetic particles to a biological component to separate it from the rest of the population. The separation is done by flowing the magnetic labeled particles inside a narrow fluid channel located over a magnetic detection region. Depending on the sensor output, the particles can be categorized appropriately [60]. Once magnetic sensors detect magnetically labeled biological components, a magnetic field can be used to divert them into a specific flow stream.

Utilizing the magnetic properties of an analyte and using GMR sensors, Porter et al. [61] patented a device that performed flow cytometer in a microfluidic device with embedded GMR sensors used to monitor the flow stream. This method eliminated the need to immobilize captured particles over GMR surfaces, making the device reusable. By detecting analytes in flow streams, the inventors were able to incorporate a direct and indirect detection mode on a single device. Direct mode sensed magnetic particles attached to an analyte using magnetic labeling, while in indirect mode a magnetic fluid created a background magnetic field that GMR sensors could detect. In the indirect mode, an external magnetic field (20 Oe) was applied over the channel. When a non-magnetic target particle flowed over the GMR sensor, it caused a decrease in the background magnetic field creating a detectable change in the sensor output. The indirect mode worked best for monitoring the purity of a solution.

Microchannels located over embedded GMR sensors can also be used for counting biological components. Pekas et al. [62] demonstrated this principle by creating a microfluidic device that counted magnetic ferrofluid droplets with volumes in the picoliter range (20 ±3 pL). The GMR sensors consisted of four GMRs (20 x 4 μm) arranged in a Wheatstone bridge circuit configuration with a sensitivity of 0.077% per Oe. The GMR material was located 300 nm beneath a microfabricated channel. A 15 Oe external magnetic field was used to magnetize the droplets before passing over the sensing area. The sensors were able to count the droplets of ferrofluid individually as well as determine their velocity and size.

*Implant Communication*

Medical researchers currently have the ability to program medical implants for optimal performance by inserting magnetic sensors inside the implant for magnetic communication, which takes place between the medical implant and an external device that generates low frequency magnetic signals [63]. In the case of magnetic communications, the body does not attenuate low frequency signals, eliminating the need for complex antennas inside medical implants. The communication with the implant can include real-time data monitoring (e.g. amount of medicine released in a drug delivery implant), diagnostic data (e.g. pacemaker battery life) and instructions to change the implant operating mode [64].

Prutchi et al. [65] patented an implantable medical device that used GMR sensors to detect the presence of a modulated magnetic field that can be used to program an implanted medical device or switch the device into different modes of operation. The invention was described as being capable of working with different types of implantable medical devices including cardiac pacemakers, defibrillators, cardioverters, drug delivery devices and neural stimulators.

Digby et al. patented a magnetic resonance imaging (MRI) magnetic field detector, used to sense when a patient is undergoing an MRI procedure [66]. The detector is needed because medical implants are sensitive to large magnetic fields and can malfunction in their presence, such as those generated by MRI machines. With Digby's et al. device, the medical implant automatically enters an MRI safe mode protecting the implant as well as the patient.

Hearing Aids are one of the many medical devices that has seen improvements made in their design by incorporating GMR sensors [67]. Sacha et al. [68] patented a new hearing aid concept that integrated a magnetic sensor to serve as a switch. Depending on the source of the incoming audio, hearing aids need switches in order to adjust the amplifier output. For instance, if the signal is coming from the user direct environment or if the signal is coming from a communication device such as a telephone, the hearing aid will appropriately switch. Traditionally, switching takes place manually or with a reed switch, however Sacha et al. incorporated a magnetic sensor that switches automatically in the presence of slight magnetic fields (1-100 Oe). A speaker on a cell phone can generate a large enough magnetic field for a GMR sensor to detect and signal a microprocessor to switch a hearing aid to the appropriate mode without the user interaction. Figure 22 shows a schematic outline of Sacha's hearing aid design. The GMR switching circuit has the advantage of using less power (31μW in pulsing mode) compared to traditional reed switches.
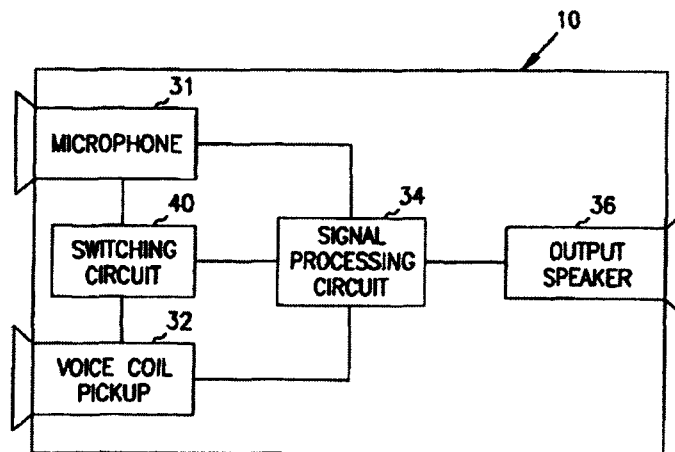
Figure 22: Schematic view of hearing aid design by Sacha [68]

# CHAPTER 4

# ELECTROCHEMICAL DEPOSITION OVERVIEW

## 4.1 Electrochemical Deposition Brief History

Electrochemical deposition has progressed, over the past century, from an art to an exact science [69]. With the discovery of the linear relationship between the over potential $\eta$ and $\log(i)$ in 1905 by Tafel [70], much research has been done to understand the electrodeposition process better. The key benefit of electrodeposition for micro/nanosciences is the ability to effectively deposit metals into nanometric size spaces. Electrodeposition is often used to bestow certain qualities to material surfaces, such as abrasion and wear resistance, corrosion protection, lubricity, and aesthetic qualities. Electrodeposition for integrated circuit fabrication, magnetic recording devices, and multilayer structures are three current technologies driving the development of electrodeposition processes [71-75].

## 4.2 Electroplating Overview

Electrodeposition of metals and alloys entail the use of an electrical current to reduce metal ions from aqueous fused-salt electrolytes to coat a conductive object, called the cathode, with a thin layer of the metal. Reduction of metal ions $M^{z+}$ in an aqueous solution can be represented by

$$M^{z+}_{solution} + ze \longrightarrow M_{lattice}$$
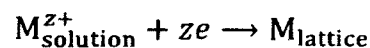
where $z$ represents the net charge number and $e$ represents electrons. Reduction of metal

ions can be accomplished in two different ways: (1) $z$ electrons can be provided by a

reducing agent in the solution, with no external power supply (electroless deposition) or

(2) $z$ electrons can be provided from an external power supply. Figure 23 shows a

standard electrochemical cell setup with electrolyte solution, cathode, anode, and a power

supply.
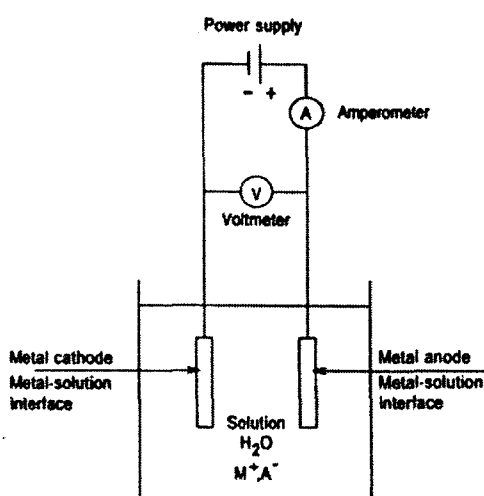


Figure 23: Standard electrochemical setup [76]
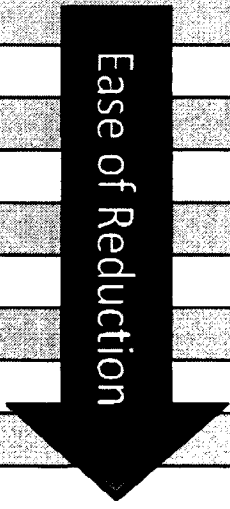
When no external power is supplied to the electrodes in Figure 23, a potential

difference exists across the electrodes called the redox electrode potential. This potential

is completely reversible and the net current flow is zero. The redox electrode potential

arises from the fact that when two dissimilar conductors come into contact, their Fermi

energy levels try to equalize, creating a flow of electrons that charges one conductor

relative to the other. When an external voltage is applied to the electrodes in the redox

setup, a current passes from the anode to metal atoms causing the atoms to oxidize and

dissolve in the electrolyte solution. The metal anode must be made of an inert metal, such

as platinum, so there is no exchange of metal ions but only electrons between the metal and electrolyte. After the anode turns the metal atoms to ions, the metal ions can be deposited at the cathode by being reduced at the interface between the electrolyte and cathode.

## 4.3 Standard Electrode Potentials

To compare different electrolyte solutions in redox systems, the standard electrode potential $(E^0)$ is found for a particular electrolyte at standard conditions and compared with a standard hydrogen reference electrode at standard conditions. Table 2 list the standard electrode potential of common metals used in the electrodeposition process.

Table 2: Standard electrode potentials of different metals

| Metal | Oxidation Reaction | Standard Electrode Potential | |
|---|---|---|---|
| Aluminum | $Al(s) \rightarrow Al^{3+}(aq) + 3e^-$ | -1.66 V | |
| Chromium | $Cr(s) \rightarrow Cr^{3+}(aq) + 3e^-$ | -.74 V | |
| Iron | $Fe(s) \rightarrow Fe^{2+}(aq) + 2e^-$ | -.409V | |
| Cobalt | $Co(s) \rightarrow Co2^+(aq) + 2e^-$ | -.28 V | Ease of Reduction |
| Nickel | $Ni(s) \rightarrow Ni2^+(aq) + 2e^-$ | -.25 V | |
| Hydrogen | $H(s) \rightarrow 2H^+(aq) + 2e^-$ | 0V | |
| Copper | $Cu(s) \rightarrow Cu2^+(aq) + 2e^-$ | +.34 V | |
| Silver | $Ag(s) \rightarrow Ag^+(aq) + e^-$ | +.799 V | |
| Platinum | $Pt(s) \rightarrow Pt^{2+}(aq) + 2e^-$ | +1.2 V | |
| Gold | $Au(s) \rightarrow Au^{3+}(aq) + 3e^-$ | +1.52 V | |

Ordinarily, a metal with a lower standard electrode potential will reduce the ions of a metal with a higher standard electrode potential. This means a high positive standard

electrode potential has a strong tendency toward reduction while a low negative standard electrode potential has a strong tendency toward oxidation.

## 4.4 Nernst Equation

The redox electrode potential is a function of temperature and the concentration of the electrolyte solution. The Nernst equation can be used to find the concentration and temperature dependence of the redox potential when the standard electrode potential is known for the electrolyte.

$$E = E^0 + \frac{RT}{zF} ln \left(\frac{Ox}{Red}\right).$$

Eq. (2)

Where $E^0$ is the standard electrode potential, $R$ is the gas constant, $T$ is the absolute temperature, $z$ is the number of electrons in the reaction, and $F$ is Faraday's number.

## 4.5 Overpotential

When an external power supply forces a current through the electrochemical cell there will be a change in the electrode potential from its equilibrium potential. This new potential is called the overpotential, $\eta$, and is represented by

$$\eta = E(I) - E.$$

Eq. (3)

Where $E$ is the equilibrium potential and $E(I)$ represents the potential applied to the cell from an external power supply. The overpotential $\eta$ is necessary to overcome the resistance of the overall electrode reaction, which is typically composed of a series of partial reactions that control the rate of deposition. The four partial reactions that control the rate of deposition are charge transfer, diffusion, chemical reaction, and crystallization. Therefore, the overpotential can be thought of as the summation of four different kinds of overpotentials:

$$\eta = \eta_{ct} + \eta_d + \eta_r + \eta_c \qquad \text{Eq. (4)}$$

where, $\eta_{ct}$, $\eta_d$, $\eta_r$, $\eta_c$ represent charge-transfer, diffusion, chemical reaction, and crystallization overpotentials, respectively. Each partial reaction has different variables and conditions that affect its rate constant and, consequently, the overall rate deposition of the electrochemical setup. Tafel established the experimental relationship between current density and overpotential in 1905:

$$\eta = a \pm b \log|i| \qquad \text{Eq. (5)}$$

with $a$ and $b$ being constants given by

$$\vec{a} = \frac{2.303RT}{\alpha zF} \log i_0 , \qquad \vec{b} = \frac{2.303RT}{\alpha zF}$$

for a cathodic process and

$$\overleftarrow{a} = -\frac{2.303RT}{(1-\alpha)zF} \log i_0 , \qquad \overleftarrow{b} = \frac{2.303RT}{(1-\alpha)zF}$$

for anodic processes where $\alpha$ and $i_0$ represents the charge transfer coefficient and exchange current density, respectively. When a cathodic process is used to determine the relationship in Equation 4, subtraction is required while an anodic process requires addition. In a redox system there is a constant exchange of electrons or current between the metal-solution interfaces given by the following equations.

$$\vec{i} = i_0 exp\left(-\frac{\alpha zF\eta}{RT}\right). \qquad \text{Eq. (6)}$$

$$\overleftarrow{i} = i_0 exp\left(\frac{(1-\alpha)zF\eta}{RT}\right). \qquad \text{Eq. (7)}$$

In the equations, $\overleftarrow{i}$ represents the cathodic partial current density and $\overrightarrow{i}$ is the anodic partial current density. When the overpotential, $\eta$, is zero, the two exchange currents are equal and are both equal to the current exchange density, $i_0$. The current exchange density is the amount of current that flows between redox electrodes at equilibrium due to electrons crossing the metal-solution interface equally in both directions. It is an important parameter of electrochemical kinetics because it can be used to characterize the electrochemical reaction and the electrode material. When the potential difference departs from equilibrium there is a net current flow or $i = \overrightarrow{i} - \overleftarrow{i}$. The net current can be found by using the Butler-Volmer equation given below.

$$i = \overrightarrow{i} - \overleftarrow{i} = i_0 \left[ exp\left(\frac{(1-\alpha)zF\eta}{RT}\right) - exp\left(-\frac{\alpha zF\eta}{RT}\right) \right]. \qquad \text{Eq. (8)}$$

Equation 7 gives the relationship between the current density $i$ and the charge transfer overpotential $\eta$ in terms of the exchange current density $i_0$ and the transfer coefficient $\alpha$.

## 4.6 Current-Potential Relationship

When an overpotential voltage is applied to an electrode in an electrochemical setup, there are three possible cases in the current-potential relationship, as seen in Figure 24.
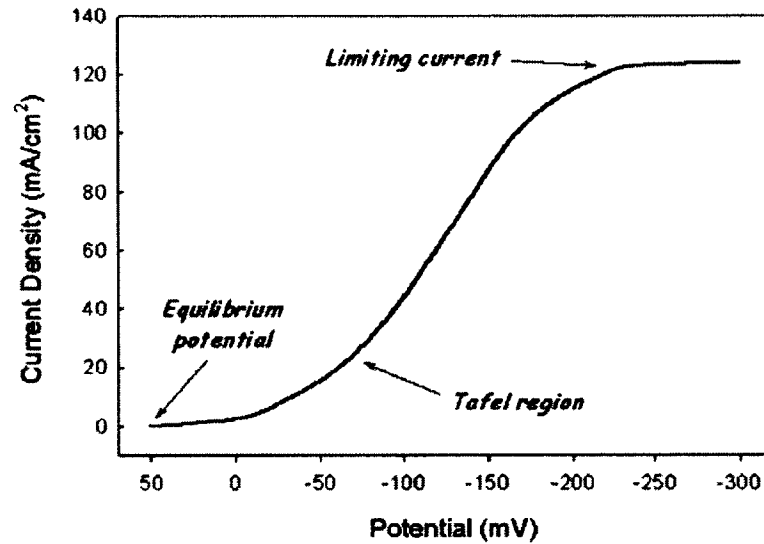
Figure 24: Current-potential relationship for a Cu electrodeposition [77]

(i) Kinetic region (Equilibrium potential): in this region, the surface concentration of metal ions is equal to the bulk concentration ($C^s = C^b$); the deposition rate and applied potential are related exponentially.

(ii) Mass transport region (Tafel region): in this region the surface concentration of ions is less than the bulk concentration ($C^s < C^b$) due to the rising reaction rate from the increasing overpotential. The deposition rate and applied potential are linearly related.

(iii) Saturation region (Limiting current): As the overpotential continues to increase, the surface concentration drops significantly ($Cs \sim 0$) as the reaction rate begins to saturate. As the reaction increases, the ion mobility governs the amount of current flowing between the anode and cathode. This current is also known as the "limiting current".

# CHAPTER 5

# NANOWIRE FABRICATION

## 5.1 Nanowire Fabrication using Template Assisted Method

Nanowires are nanostructures with diameters in the nanometer range that possess very high aspect ratios. Nanowires can be conductive, semiconducting, or insulating depending on their material makeup and fabrication method. Template assisted nanowire fabrication is an inexpensive and relatively simple method for producing nanowires through electrodeposition. The template has many nano size pores that serve as a mold for the formation of a single nanowire. Usually the bottom of the template is made conductive by sputtering a metal, such as gold, in order to form a base substrate for the formation of nanowires. Figure 25 shows the electrochemical setup for template assisted nanowire fabrication.
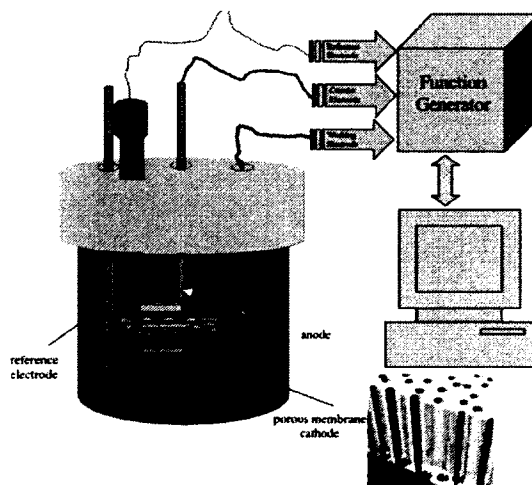


Figure 25: Redox electrochemical setup for template assisted nanowire fabrication [78]

## 5.2 Templates

Polycarbonate membranes were the first widely used templates to create nanowires. Traditionally, polycarbonate membranes are used as filters but their pore sizes made them excellent candidates as templates for nanowire fabrication. Eventually, aluminum oxide membrane templates were used for nanowire fabrication because they possessed a higher uniformity of pores at a much higher density than polycarbonate membranes. Figure 26 shows SEM images of a polycarbonate membrane and an aluminum oxide membrane. Table 3 gives a comparison of polycarbonate and aluminum oxide membranes.
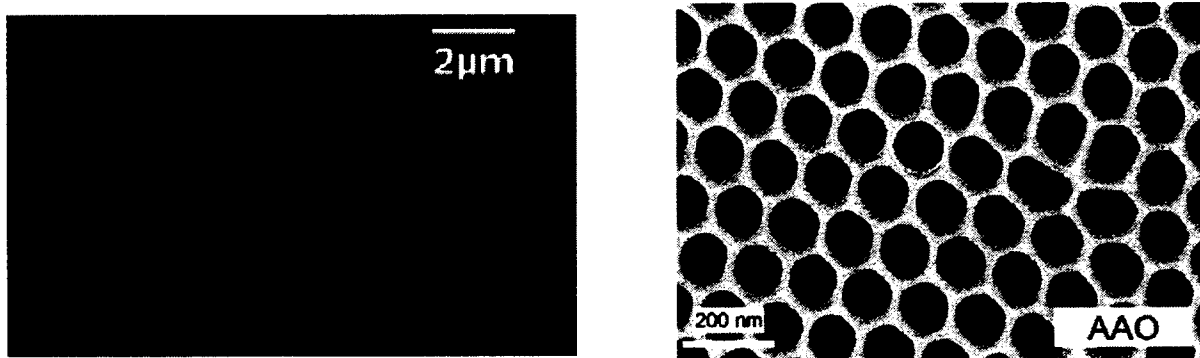


Figure 26: SEM images of (a) polycarbonate membrane and (b) anodic aluminum oxide membrane [78]

Table 3: Comparison of commercially available polycarbonate and aluminum oxide membranes

|  | Polycarbonate | Aluminum Oxide |
|---|---|---|
| Pore Size | 15 nm to 12 μm | 13 nm-200 nm |
| Pore Uniformity | Good | Excellent |
| Thickness | 7-20 μm | 50-100 μm |
| Density | $10^5$ to 6 x $10^8$ pores/cm$^2$ | 2 x $10^9$ to 1 x$10^{11}$ pores/cm$^2$ |
| Thermal Range | Up to 140°C | Up to 500°C |
| Relative Cost | Low | High |

## 5.3 Alloy Nanowires

Electroplating inside the membrane required one side of the template to be conductive, which can be accomplished by either sputtering or coating the membrane with a metal. Figure 27 shows three pores of a membrane with a conductive substrate serving as a cathode. When a constant DC voltage is applied to the electrochemical setup metal ions from the electrolyte solution will travel inside the nanopores and bond with the substrate and as the deposition continues to take place, metal nanowires are formed inside the pores.
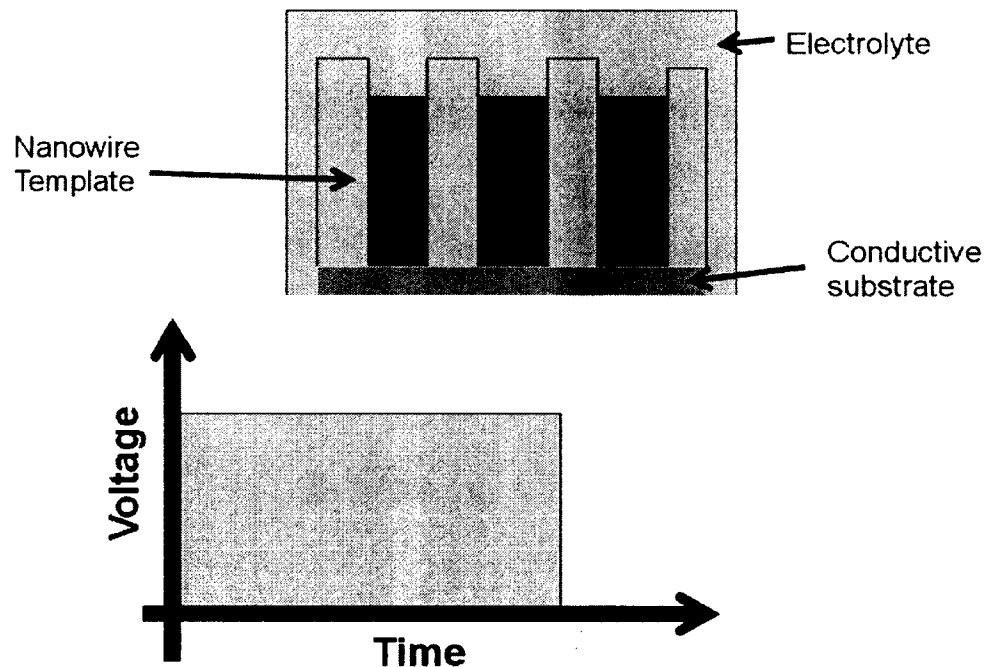


Figure 27: Constant potential electroplating scheme for nanowires

If more than one type of metal ion is in the electrolyte solution, a combination of the ions will deposit at the substrate creating an alloy. The magnitude of the applied potential to the electrodes determines the deposition rate of each type of metal ion and the

chemical makeup of the deposited alloy. It is also important to note that higher potentials lead to overall faster deposition times.

## 5.4 Multilayer Nanowires

Electroplating multilayers of two separate metals or alloys is very advantageous in many applications and was first done by Brenner in 1939 [79]. Brenner accomplished electrodeposition of multilayer thin films by utilizing two separate baths for the two-deposited metals making up the multilayer deposition by periodically transferring the substrate between two electrolyte solutions. Using two separate baths for deposition is very cumbersome for many layer systems, so in 1983 Cohen studied the deposition of multilayers from one electrolyte solution [80]. By choosing metals with high differences in standard potentials, Cohen deposited multilayers by alternating the deposition potential between two values. Cohen observed that he was not getting clean multilayers of the two-deposited metals but rather two different alloy layers in the multilayer system.

In 1986, Yahalom and Zadok found a method to overcome the problem of depositing alloys instead of pure metals in electrodeposited multilayer materials [81]. Their solution was to only allow traces of metal A ions to be introduced in an electrolyte solution with a high concentration of metal B ions (assuming that metal A has a higher standard electrode potential than metal B). At an adequately low polarization potential the rate of deposition of metal B is high while the rate of deposition of metal A is slow because it is controlled by diffusion. When the potential is at a considerably less negative polarization potential, only metal A is deposited. As the potential is cycled between the two potentials, multilayers of pure metal A and metal B with traces of metal A are formed, as seen in Figure 28.

48
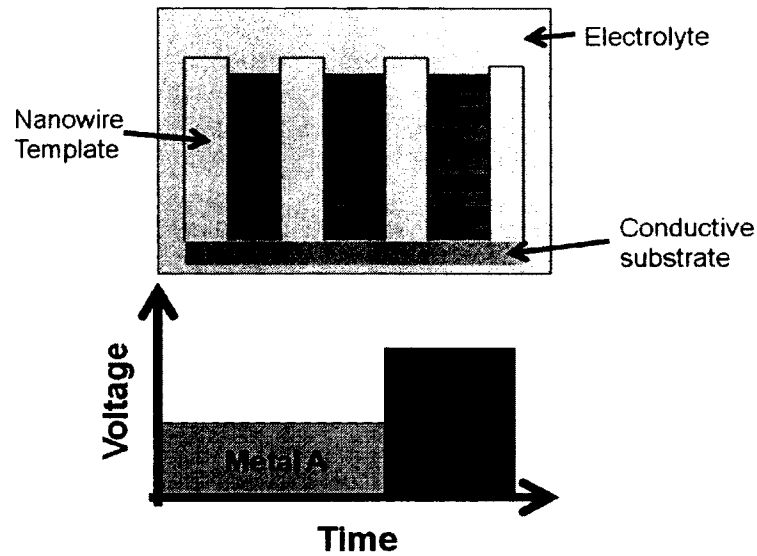


Figure 28: Pulsed potential scheme for electrodeposition of multilayer nanowires

After the nanowires are electrodeposited into the pores of the anodic aluminum oxide (AAO) membrane templates, the template can be dissolved with strong base freeing the nanowires. After the template is completely dissolved, the nanowires can then be rinsed and suspended in a carrier solution, such as DI water or isopropyl alcohol. When the nanowires are needed for further fabrication steps, ultrasonication can be used to better disperse the nanowires inside the carrier solution.

Figure 29 shows the overall steps for the template assisted nanowire fabrication. In summary, an empty template is made conductive on one side in order for metals to be deposited inside the pores. After deposition, the nanowires are freed by dissolving the template and then suspending them in a carrier fluid until needed for further fabrication steps.
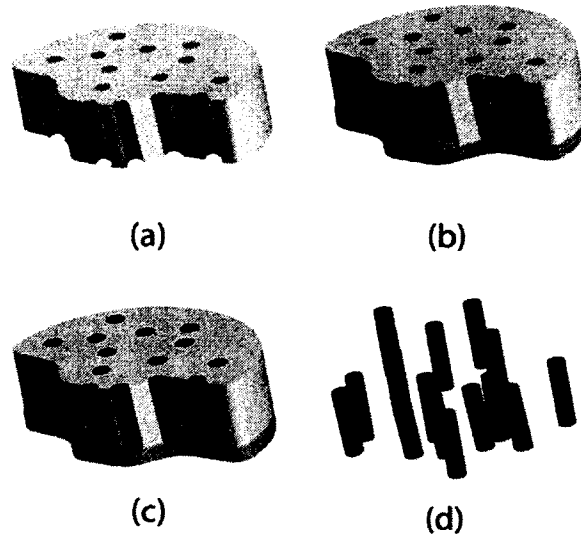
Figure 29: Template assisted nanowire fabrication (a) empty template membrane (b) template membrane coated with conductive metal on bottom (c) nanowires electroplated inside template membrane (d) nanowires released from template

# CHAPTER 6

# EXPERIMENTAL DETAILS

## 6.1 Electrochemical Setup

Research presented in this dissertation was done with a standard electrochemical setup, as seen in Figure 30.
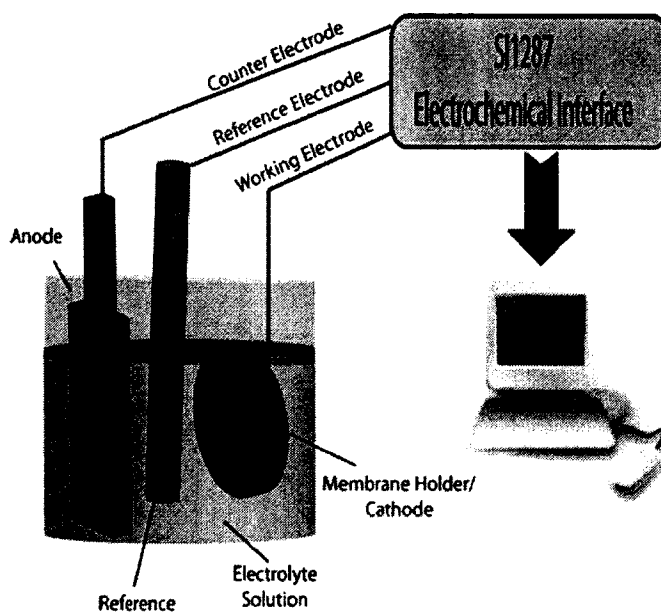


Figure 30: Diagram showing experimental setup for electrodeposition

A membrane holder was fabricated to hold 25 mm anodic aluminum oxide (AAO) membranes during electrodeposition. The holder purpose is to clasp membranes securely in place while providing a conductive substrate for membranes during electrodeposition. An o-ring and grommet were used to protect the conductive substrate from coming into

contact with electrolyte solutions and to make sure the electrolyte only encountered membranes from above. The holder was machined out of two cylinder pieces of chlorinated polyvinyl chloride (CPVC) and was fastened together with four nylon thumbscrews. CPVC material and nylon screws were chosen because of their high chemical resistance to the electrolyte solutions. The top piece had a hole drilled into the center that allowed the electrolyte solution to pass through while the bottom piece had a copper substrate that served as the cathode as seen in Figure 31.



(a)　　　　　　(b)

(c)
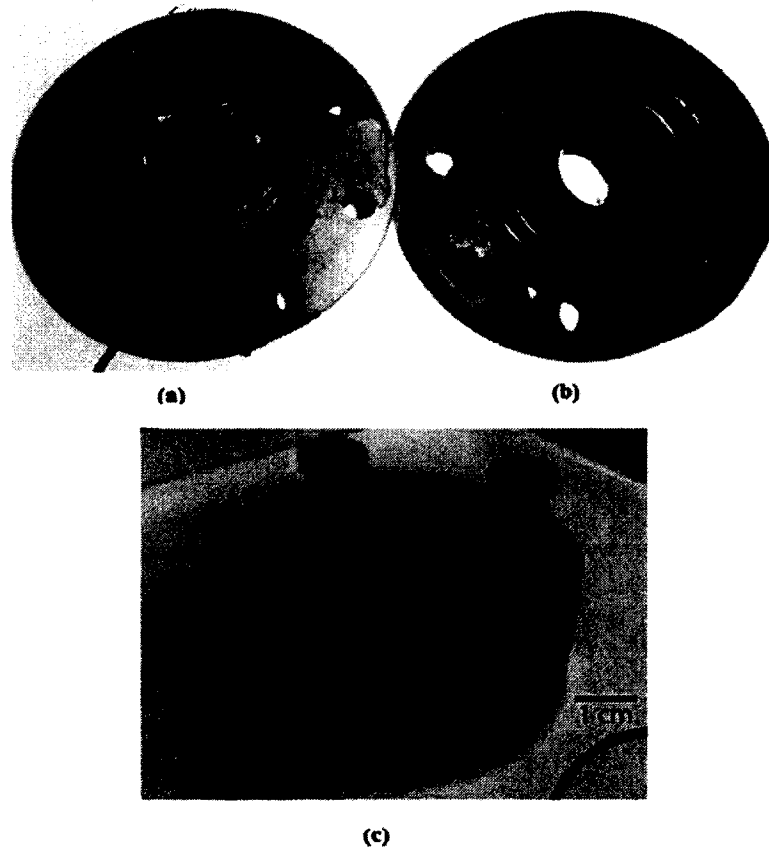
Figure 31: Pictures of the fabricated membrane holder for Electrodeposition (a) bottom part of the holder serving as cathode (b) top part of holder with rubber seals (c) holder held together with nylon screws

A platinized titanium anode from SRA Soldering Products was used as the counter electrode along with a saturated KCL electrode as a reference electrode in the electrochemical setup. An Electrochemical Interface from Solartron Analytical serves as the potentiostat for all experiments and was controlled from a standard computer.

## 6.2 Electrolyte Solutions

All electrolyte solutions were prepared by mixing various metallic salts with DI water. Table 4 summarize the electrolyte bath used to create GMR nanowires for this research project.

Table 4: Components for GMR electrolyte

| No | Compound | Concentration |
| --- | --- | --- |
| 1 | Copper(II) Sulfate Pentahydrate ($CuSO_4.5H_2O$) | 8 mM |
| 2 | Cobalt(II) Sulfate Heptahyrate ($CoSO_4.7H_2O$) | 50 mM |
| 3 | Nickel (II) Sulfamate Hydrate ($Ni(SO_3NH_2).XH_2O$ | 32 mM |
| 4 | Iron (II) Sulfate Hydrate ($FeSO_4.7H_2O$) | 1 mM |
| 5 | Potassium Sodium Tartrate ($C_4H_4KNaO_6.4H_2O$) | 24 mM |
| 6 | Sulfamic Acid ($H_3NO_3S$) | 10.5 mM |

The electrolyte bath contains sulfamic acid to help facilitate electrodeposition by keeping the pH of the electrolyte bath acidic. In addition, the electrolyte bath contains sodium potassium tartarate to help avoid precipitation of compounds during the electrodeposition process.

A polarization study was performed on the bath in a previous research study to determine the best plating potentials for alloy and copper deposition [82]. The potentiostat was programmed to generate a sweeping voltage between the anode and cathode at a rate of 2 mV/sec and the resulting polarization curve can be seen in Figure 32.
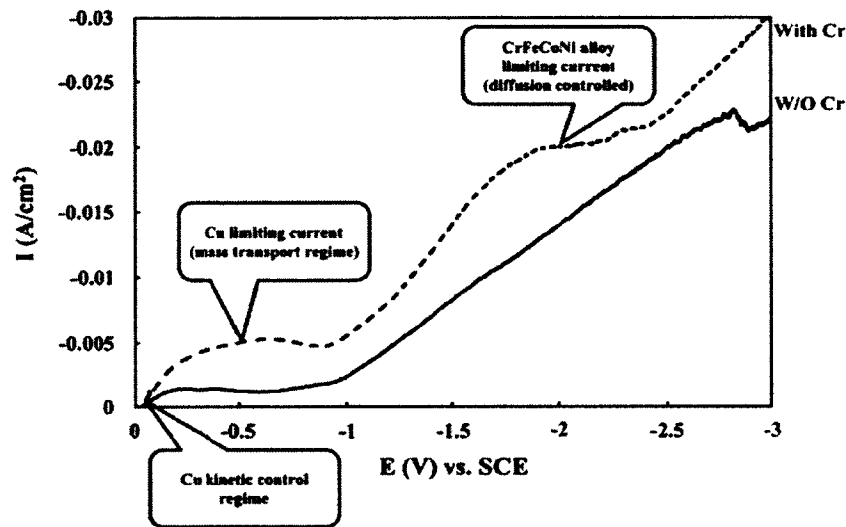


Figure 32: Polarization curve of electrolyte, highlighting the kinetic and limiting current regions [82]

Looking at Figure 32, when the potential is greater than –.35V, Cu is in the mass transport region and is the dominant element depositing because Cu is nobler than Co, Ni, and Fe. However, as the potential is increased the current density starts to increase rapidly at –1V and then begins to level off at –2 V. This region is described as the alloy kinetic control region and the Co/Ni/Fe alloy is the dominant deposited material with traces amounts of Cu also being deposited. Compositional analysis was performed at various potentials to determine the elemental makeup of the deposited nanowires and can be seen in Table 5.

Table 5: Composition analysis of deposited metal alloys at various potentials [82]

| Potential (V) | Cu (At%) | Fe (At%) | Co (At%) | Ni (At%) |
|---|---|---|---|---|
| -0.25 | 96.21 | 0.50 | 2.02 | 1.25 |
| -0.30 | 98.76 | 0.16 | 0.79 | 0.28 |
| -0.35 | 93.93 | 0.70 | 4.42 | 0.94 |
| -0.40 | 94.75 | 2.21 | 2.57 | 0.46 |
| -1.40 | 14.27 | 1.56 | 64.52 | 19.64 |
| -1.60 | 14.72 | 1.36 | 56.31 | 27.59 |
| -1.80 | 15.54 | 2.23 | 55.83 | 26.40 |
| -2.00 | 28.67 | 3.90 | 44.60 | 22.82 |
| -2.20 | 39.59 | 1.12 | 41.53 | 17.74 |
| -2.40 | 12.44 | 2.00 | 60.25 | 25.30 |
| -2.60 | 9.78 | 1.90 | 52.57 | 35.74 |

From the Table 5, it can be seen that at lower potentials Cu is the dominate metal being deposited and, as the potential increases, Fe, Co and Ni make up a larger percentage of the deposited metal alloy.

## 6.2 Electrodeposition of Multilayer GMR Nanowires

The thickness of the copper and alloy multilayers of the GMR nanowires determine the maximum %MR possible. The thickness of the copper layer should be smaller than the spin diffusion length of copper, which is approximately 50 nm at room temperature [83]. Once the thickness of both the copper and alloy layers are decided, the amount of charge needed to create each layer is calculated. Appendix A shows the calculations for charge needed to form each layer. Figure 33 shows how the amount of charge corresponds to the thickness of both copper and alloy layers.
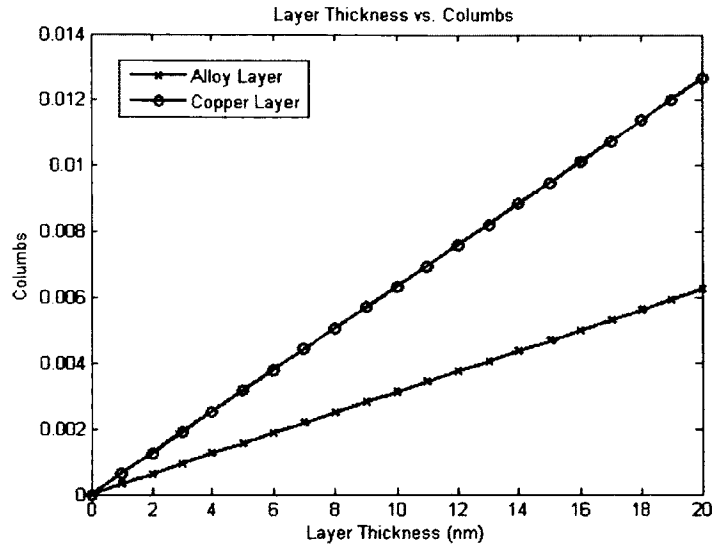
**Figure 33:** Charge vs. thickness of copper and alloy layers

For nanowire GMR fabrication, 25 mm Anodisc® with 20 nm pores were used. The membranes were coated with a thin layer (~100 nm) of gold before being layered with GaIn to make one side conductive at the bottom of the pores for electroplating, as seen in Figure 34.
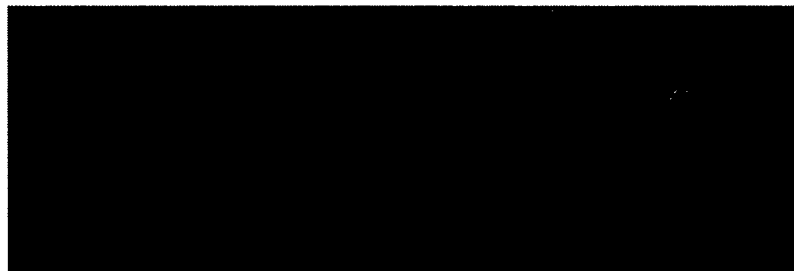


Figure 34: AAO membrane throughout the coating process: From left to right-Blank AAO membrane, gold coated AAO membrane, gold and GaIn coated membrane

Next, the membrane was secured inside the holder before being placed in the prepared electrolyte solution. A pulsing potential scheme was used to electrodeposit the multilayer GMR nanowires, as given in the following flowchart in Figure 35.
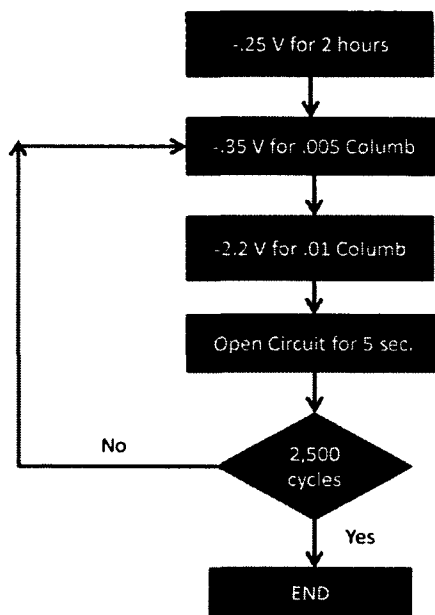
Figure 35: Flowchart of electrodeposition scheme

In order to make sure that the layers that are deposited are flat, a copper base is formed at the bottom of the membrane by keeping the potential at -.25 V for 2 hrs. After the Cu base was formed, the multilayers were deposited by first keeping the potential at -.35 V until a total amount of .005 C of charge passed through the cathode for copper layers and then changing the potential to -2.2 V for .01 C of charge for the alloy layers. After deposition of the alloy layer, the potentiostat went into open circuit to prevent severe alloy dissolution during the copper deposition cycle that could damage the interfaces and leave the alloy layer thickness inexact [34]. Following the open circuit interruption the entire cycle was repeated over again starting with the copper layer. The length of the nanowires depended on the number of cycles performed during electrodeposition. On average, it took 30s for a copper layer, less than 1s for an alloy layer, and 5s for the open circuit stage for a total of 36s for a complete cycle. Combing

the 2 hrs for the copper base at the beginning of the fabrication process with the deposition of the multilayers, it took 17 hrs to form 1,500 multilayer GMR nanowires.

## 6.4 Nanowire Thin Film Fabrication

Once the electrodeposition of the nanowires into the AAO membrane was complete, the membrane was removed from the holder and rinsed with DI water. Next, a cotton applicator dipped in concentrated nitric acid was used to gently remove the GaIn and gold coatings, being careful not to remove the deposited nanowires from the membrane. After the membrane was rinsed with DI water, it was placed in a 6 M solution of NaOH for 10 mins to dissolve the membrane and release the nanowires. A strong magnet was used to pull the nanowires toward the side of the beaker, as seen in Figure 36, so the NaOH could be siphoned off with a pipette.



(a)                              (b)
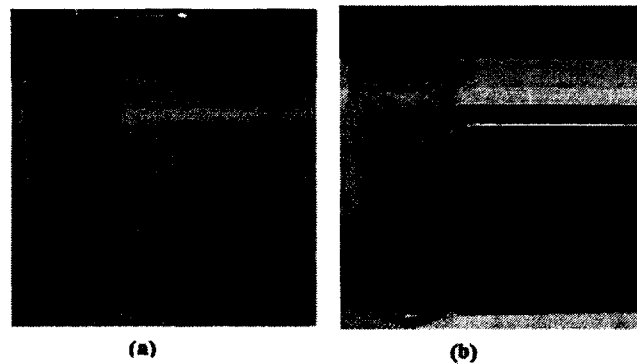
**Figure 36:** (a) Suspended GMR nanowires (b) Nanowires being attracted with magnet to the side of a vial

The nanowires were then rinsed with DI water twice, before being suspended in 30 ml of isopropyl alcohol. Isopropyl alcohol was chosen as the buffer solution because the nanowires showed less aggregation and longer suspension times than when suspended in DI water. When the nanowires were needed in further fabrications steps, they were

ultrasonicated for 20 mins with a 100-watt Bransonic® ultrasonic cleaner to separate any aggregates of nanowires. Once the nanowires were fabricated and suspended, they were turned into thin films using vacuum filtration and metering rod methods.

### 6.4.1 Vacuum Filtration Method

The first method used vacuum filtration and a PDMS stamp to transfer the nanowires to a receiving substrate. Two milliliters of the suspended GMR nanowire solution was vacuum filtered onto a 200 nm pore AAO membrane with a vacuum flask and pump. After allowing the membrane to dry, a cylindrical PDMS stamp was used to gather the nanowires from the membrane by forming conformal contact between the stamp and nanowires. After collecting the nanowires, the PDMS stamp was used to transfer the nanowires to a heated (120 °C) receiving substrate. Figure 37 highlights the vacuum filter nanowire thin film process steps. Figure 38 shows nanowires on AAO membranes after vacuum filtration.

(a) (b)

(c) (d)
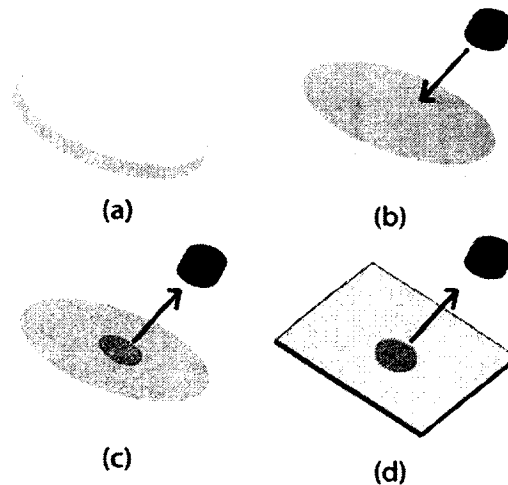
Figure 37: Nanowire thin film fabrication process (a) empty filter membrane (b) filter membrane with thin layer of GMR nanowires (c) PDMS stamp collecting the GMR nanowires (d) PDMS stamp transferring the nanowires to a receiving substrate

Figure 38: Nanowires on AAO membranes after vacuum filtration

After creating the nanowire thin films on the receiving substrate, electrical contacts were placed on the films with silver paint. An electrolysis oxidation removal technique was performed to increase the conductivity of the film. The electrolysis process included submerging the thin film in 10% acetic acid and then applying an anode to the film and a cathode to the acid. Next, 1.25 V was applied to the electrodes for approximately 1 min. The electrolysis process removed oxidation from the nanowires and helped fuse the nanowires together through Joule heating of the nanowires. Once the electrical contacts were made, the entire sensor was sealed with a protective cover to keep the sensor safe from the environment.

### 6.4.2 Metering Rod Method

In order to evaluate the possibility of covering large areas with nanowire GMR thin films, liquid surface coating technologies were investigated. Liquid surface coating technology finds a variety of applications in industry including applying paints, color photographic films, X-ray films, printing plates for papers/books/magazines, magnetic storage media, optical disks, wallpaper and adhesive tapes [84]. Table 6 lists a number of liquid surface coating techniques along with their key parameters.

Table 6: Overview of some of the liquid coating technologies [84]

| Process | Viscosity (Pa·s) | Wet Thickness (μm) | Coating Accuracy (%) | Speed Max (m/min) | Effect of Web Roughness |
|---|---|---|---|---|---|
| Rod (wire wound) | 0.02-1 | 5-50 | 10 | 250 | Large |
| Reverse roll | 0.1-50 | 5-400 | 5 | 300 | Slight |
| Forward roll | 0.02-1 | 10-200 | 8 | 150 | |
| Air knife | 0.005-.5 | 2-40 | 5 | 500 | Large |
| Knife over roll | 0.1-50 | 25-750 | 10 | 150 | Large |
| Blade | 0.5-40 | 1-30 | | 1500 | Large |
| Gravure | 0.001-5 | 1-25 | 2 | 700 | |
| Slot | 0.005-20 | 15-250 | 2 | 400 | Slight |
| Extrusion | 50-5000 | 15-750 | 5 | 700 | |
| Slide | 0.005-0.5 | 15-250 | 2 | 300 | Slight |
| Curtain, precision | 0.005-.5 | 2-500 | 2 | 300 | Slight |

After investigating the many coating techniques, a wire-wound metering rod method was implemented to create nanowire GMR thin films due to the method being low cost and simple. Charles W. Mayer, who founded the Mayer Coating Machines Company located in Rochester, New York in 1905, invented the wire-wound metering rod, also known as the Meyer Rod, to coat large surfaces with thin films of liquids. Figure 39 shows an example of a simple wire-wound metering rod.
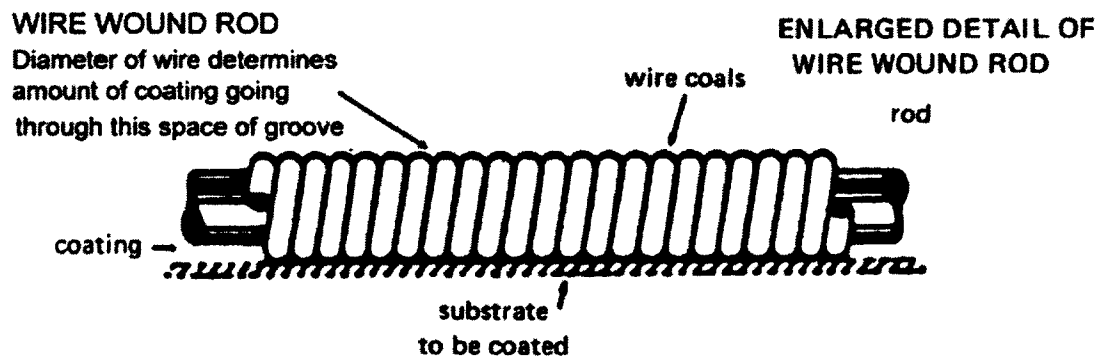


Figure 39: A typical wire-wound metering rod [85]

A wire, usually made of stainless steel, is wound tightly around a rod also made out of stainless steel. As the rod glides across a substrate, the diameter of the wound wire determines the thickness of the wet film left behind. Initially, the shape of the coating is a series of stripes spaced apart proportional to the spacing of the wire windings before the stripes are pulled together due to the surface tension in the liquid film. As the film dries from either natural air convection or a heat source, a flat and smooth film is formed. A 1:10 ratio is usually observed between the wet film thickness and the wire diameter along with 2.54 $\mu$m accuracy in the film thickness [85]. Many factors affect the films final thickness including the viscosity of the liquid, substrate tension, moving speed of the metering rod with respect to the substrate, wettability of the liquid, and penetration of the liquid into the substrate. The metering rod method has the advantages of being low cost, having accurate thickness control, easy setup, and a moderate coating speed of up to 305 m per min.

A 40.64 cm long #10 metering rod was purchased from Diversified Enterprises. The #10 metering rod is designed to give a 25.4 $\mu$m film thickness and has a coverage area of 39.4 $m^2$ per liter of liquid. GMR nanowires suspended in isopropyl alcohol were dispensed onto a PET plastic substrate before the metering rod was used to spread the solution uniformly over the PET surface. As the PET film was allowed to dry a GMR nanowire film adhered to the PET substrate. Multiple coatings of GMR nanowires could be applied using the metering rod. Once the desired thickness of GMR nanowires was reached, the PET film was allowed to completely dry before PDMS stamps were used to collect the nanowires onto their surfaces for transfer to PET substrates. Silver paint was used to create electrodes for testing the GMR thin films and, as with the vacuum filter

method, an acid could be used to remove the oxidation layer from the nanowires to promote conductivity. Figure 40 shows the process steps for the metering rod method while Figure 41 shows the actual GMR thin film on the PET substrate using the metering rod method.
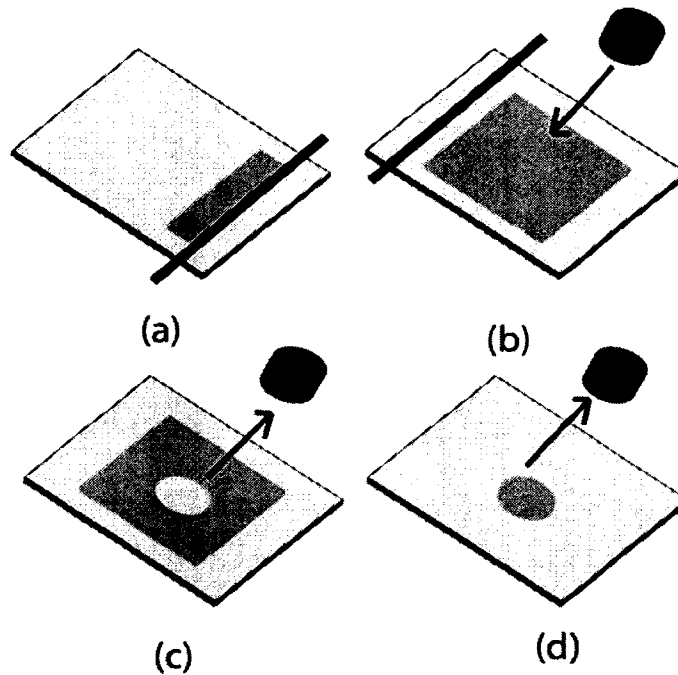


Figure 40: GMR thin film applied with a metering rod method: (a)-(b) GMR nanowire thin film being applied to a PET substrate (c) PDMS stamp being used to transfer nanowires (d) PDMS stamp transferring nanowires to heated PET substrate

(a)

(b)

(c)
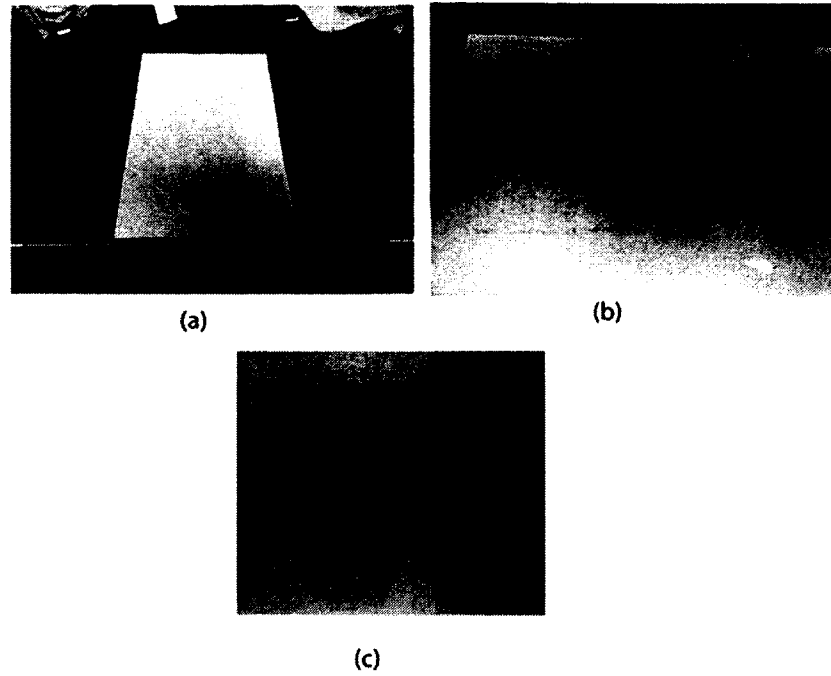
Figure 41: (a) Metering rod setup (b) GMR nanowire thin film on PET substrate (c) GMR nanowire thin film sensor fabricated with the metering rod method

# CHAPTER 7

# CHARACTERIZATION EQUIPMENT

## 7.1 Scanning Electron Microscope (SEM)

A Hitachi S-4800, field emission scanning electron microscope (FESEM), was used to characterize the GMR nanowire thin film visually along with determining the density and average length of the nanowires. The SEM works by focusing a beam of electrons in a square TV–type raster pattern across the sample and detecting any backscattered and secondary electrons emitted from the surface of the sample. The spatial resolution of the SEM was 1 nm with magnification capability of 30 x to 800,000 x.



Figure 42: Hitatchi S-4800 FESEM

## 7.2 Energy Dispersive Spectroscopy (EDS)

In order to determine the elemental makeup of the multilayer nanowires Energy Dispersive Spectroscopy (EDS) was performed with an Hitachi S4800 field scanning electron microscope. The EDS is carried out by detecting the characteristic x-rays generated from a sample that is bombarded with electrons from the SEM electron beam. The electron beam interacts with the sample to produce different kinds of emissions created by electrons ejected from their ground states. The EDS detector segregates the characteristic x-rays of the various elements in the energy spectrum and supplies that information to a computer used to determine the composition of the elements in the sample.

## 7.3 Hall-Effect Measurement System

A Lakeshore 7603, Hall measurement system, was used to measure the magnetoresistance of the GMR nanowire thin film samples. Although the Hall Effects of the samples were not measured with the Lakeshore 7603, it did provide the capability of producing a ±1 T magnetic field with the ability to measure resistances between 10 n$\Omega$ to 10 M$\Omega$, which made it a valuable tool in this study. Sample preparation included mounting a GMR nanowire thin film sensor onto a sample holder module, Lakeshore 75011. MR curves were obtained by programming the system to produce variable magnetic fields, while applying a constant current. The resistance of the samples were taken at each magnetic field step and plotted to a graph.
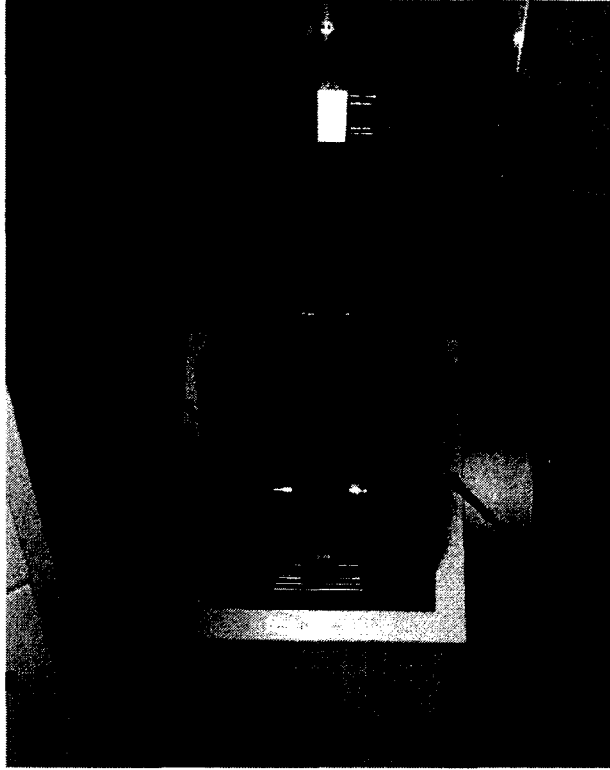
Figure 43: Picture of Lakeshore 7603 Hall Measurement System

# CHAPTER 8

## GMR NANOWIRE THIN FILMS

### 8.1 Oxidation Removal

The conductivity of the nanowire GMR thin films depends profoundly on the amount of oxidation present. Routinely, after a GMR nanowire thin film was fabricated, its resistance was above the range limit of a standard multimeter ($>80$ M$\Omega$). A variety of techniques were tried to remove the oxide layer from the nanowires. Chemical etching with various acids at different concentrations were explored for oxidation removal with little success. The tested acids included 5-10% acetic acid, 5-20% boric acid, 5-20% citric acid and 5 to 10% oxalic acid. 99% nitric acid was tested on a film and a strong chemical reaction took place making the GMR thin film useless. BPS-172 from Air Products was also tested to see if it could remove the oxide layer from the thin film without destroying the nanowires. BPS-172 was developed for the removal and regrowth retardation of copper oxides, however, it has not been proving effective with oxide layers on metal alloys. After testing the BPS-172 at various concentrations it was found ineffective at making the thin films more conductive.

An electrolysis oxidation removal technique that is commonly used to remove rust from iron was tried by submerging GMR thin films in a liter of deionized water with a tablespoon of baking soda. The negative electrode was applied to the film and the positive electrode was placed in the water. Various voltages between 1 to12 V were

applied to the electrode and electrical currents were observed between the electrodes, but after testing the dried films their resistances were still extremely high.

Finally, a technique was discovered to successfully remove oxidation from the thin films. A 10% acetic acid solutioin was applied to a thin film with two electrodes; a voltage was then applied to the electrodes producing a current flow through the film. Next, the samples were rinsed with isopropanol alcohol and then the film was allowed to air dry for 20 mins. After testing the thin films, it was found that their resistances decreased dramatically after the treatment. This difference in resistances can be contributed to the removal of oxidation and a fusion of the GMR nanowires. Care had to be taken not to destroy the multilayers in the nanowires by burning them with excessive current. It was observed that if higher voltages were used initially it was ok because the thin films resistances were high, but over time as the films resistance decreased from the treatment, the current became higher. If the current became too high, the nanowires burned leaving behind a charred thin film. In addition to the magnitude of the applied voltage, the amount of time the thin film was undergoing the oxidation removal treatment affected the amount of oxidation removed from the film, ultimately affecting the final resistance. Figure 44 shows a pictorial example of how the nanowires undergo oxidation removal.
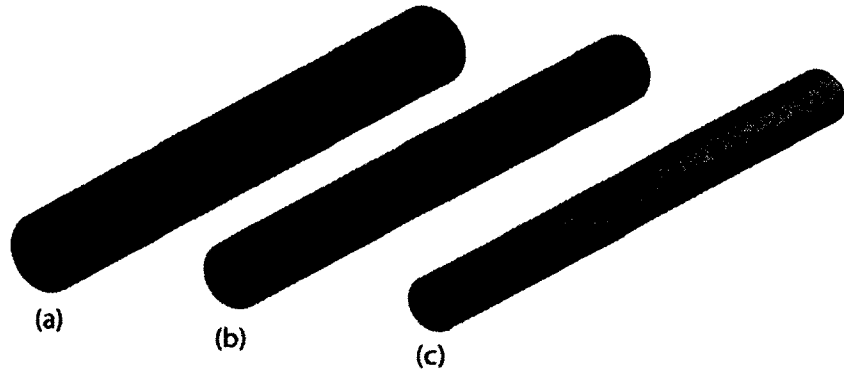
**Figure 44:** GMR nanowires with various oxidation thicknesses, with (a) having the largest oxidation thickness and (c) having no oxidation present

As the oxidation thickness decreased, less potential energy is needed to overcome the oxide barrier, as seen in Figure 45. On average the thin films resistances decreased over 99% after undergoing a full oxidation removal treatment.
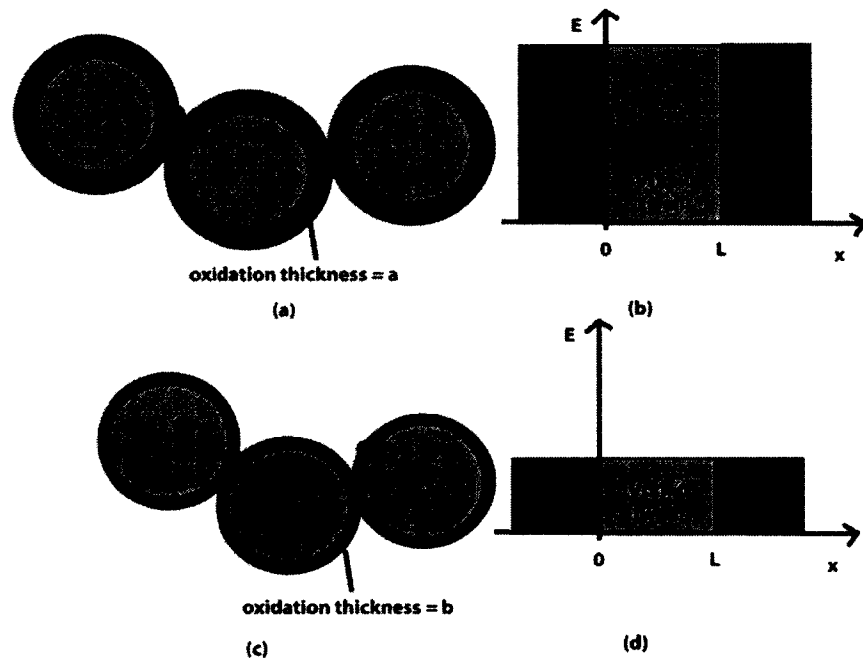


**Figure 45:** (a) Cross sectional view of nanowires with a thick oxidation layer (b) particle in a box model for nanowires with a thick oxidation layer (c) cross sectional view of nanowires with a thin oxidation layer (d) particle in a box model for nanowires with a thin oxidation layer

## 8.2 EDS Analysis

One way to measure the amount of oxidation present in the nanowire thin films is to take EDS measurements. Figure 46 shows EDS measurements taken of bare PET plastic and a nanowire thin film sample before and after the sample experienced an oxidation removal treatment.

| Element | Wt% | At% |
|---------|-------|-------|
| C | 70.04 | 77.91 |
| O | 25.17 | 21.02 |
| Co | 04.19 | 00.95 |
| Cu | 00.60 | 00.13 |
| Matrix | Correction | ZAF |

(a)

| Element | Wt% | At% |
|---------|-------|-------|
| C | 63.71 | 78.85 |
| O | 17.96 | 16.69 |
| Co | 09.53 | 02.40 |
| Cu | 08.80 | 02.06 |
| Matrix | Correction | ZAF |

(b)

| Element | Wt% | At% |
|---------|-------|-------|
| C | 63.37 | 79.79 |
| O | 15.98 | 15.11 |
| Co | 10.11 | 02.59 |
| Cu | 10.54 | 02.51 |
| Matrix | Correction | ZAF |

(c)
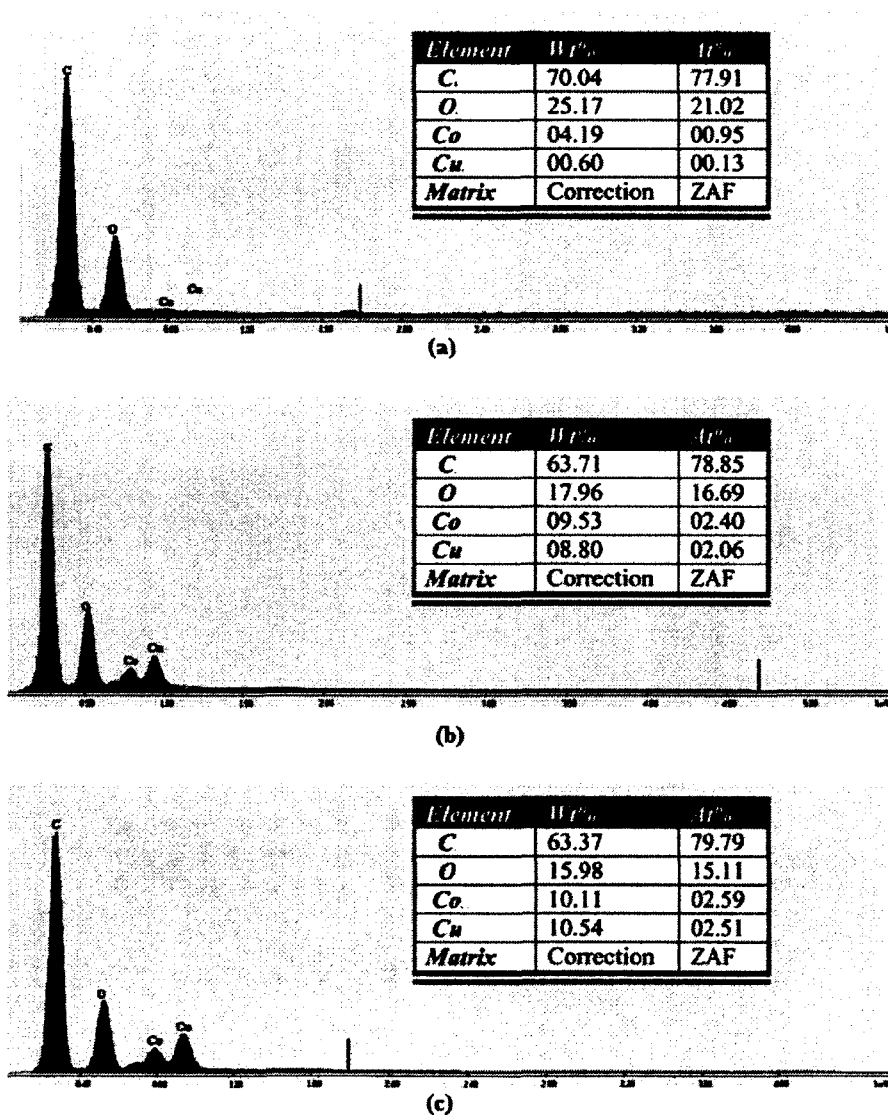
**Figure 46:** (a) EDS measurement of bare PET plastic (b) EDS measurement of GMR nanowire thin film on PET plastic with no oxidation removal (c) EDS measurement of GMR nanowire thin film on PET plastic after 10% acetic acid treatment with a 50 μA current applied to the film for 400 sec.

Figure 46(a) shows the EDS measurements taken of bare PET plastic. Figure 46(b) shows the EDS measurement of a nanowire GMR thin film on PET plastic with no oxidation removal treatment. Figure 46(c) shows the EDS measurement of GMR nanowire thin film on PET plastic after 10% acetic acid treatment with a 50 μA constant current applied to the film for 400 sec. It can be seen that the percent weight of oxygen decreased after the oxidation removal treatment when compared to the EDS sample with no oxidation removal treatment.

## 8.3 Imaging

Figure 47 shows four nanowire GMR thin films that were deposited on a PET substrate with a cylindrical PDMS stamp. It can be seen in Figure 47(b) that the nanowire GMR thin films are flexible and transparent, which are two properties current magnetic sensors do not posses. The density of the GMR nanowires determines how transparent they appear.



(a)                                    (b)

Figure 47: (a) Four nanowire GMR thin films on arched PET substrate to exhbit their flexability (b) same thin films from (a) over Louisiana Tech logo to demostrate the sensor transparency

Figure 48 shows a SEM image of one of the GMR nanowire thin films. Most of the nanowires fall between 10 and 20 μm in length.



Figure 48: SEM image of nanowire GMR thin film on PET substrate



Figure 49: Closer view of nanowire GMR thin film on PET substrate

Initially, it was assumed the nanopores of the membrane were uniform throughout the length of the membrane. However, after viewing SEM images it became clear that the nanowire diameters were not 20 nm as expected but 200 nm. After investigating, it was found that the template pores are not uniform but have a 20 nm opening on the top and 200 nm at the bottom. Figure 50(a) shows the initially assumed dimensions of the AAO nanopores, and Figure 50 (b) shows the actual dimensions. Fortunately, even with the unexpected dimensions of the nanowires, they still exhibited the GMR effect.
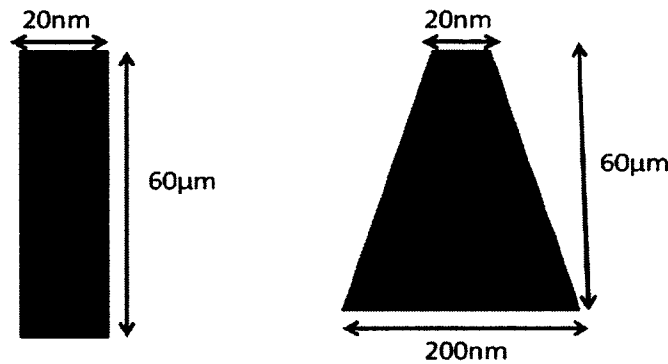


Figure 50: (a) Initially assumed nanopore dimensions of AAO templates (b) actual nanopore dimension of AAO templates

## 8.4 Testing

After placing electrodes on the thin films to create magnetic sensors, they were tested by using a small neodymium magnet as well as a Lakeshore 7603 Hall Measurement System. After testing the sheet resistance before and after bending multiple sensors, resistance changes were observed due to the nanowires shifting throughout the film. However, the %MR was unaltered after moderate bending.

Silver paint was used to make electrodes for electrical contact with a GMR thin film leaving a 10 mm x 5 mm sensor test area, as seen in Figure 51.

Figure 51: Nanowire GMR thin film with silver paint electrodes

Figure 52 shows the output voltage and resistance change of the GMR thin film when a constant 0.5 mA current was passed between the electrodes of the thin film. The square wave represents a small neodymium magnetic being brought in close proximity (2mm) and removed from the magnetic sensor in 1 min intervals.
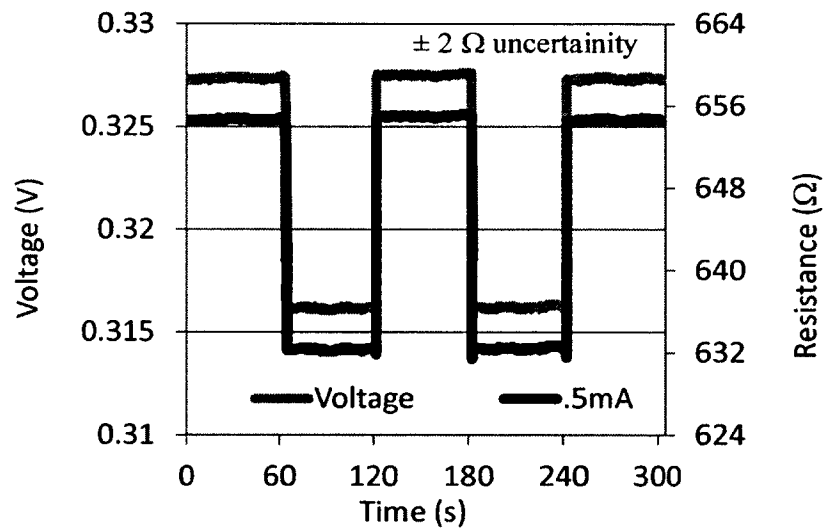


Figure 52: (a) Voltage output and resistance of a GMR thin film when a .5 mA current passes between the electrodes of a magnetic sensor. The square wave represents a small magnet being brought in close proximity and removed from the sensor in 1 min intervals

The same magnetic sensor was tested again at 1 mA and 3 mA, and Figure 53

shows the resistance as the magnet was in close proximity and removed in 1 min intervals

from the thin film. Figure 54 shows a 4 mA test with the same conditions as the previous

test. When the film was tested at 4 mA, there was considerable noise and hysteresis due

to self-generating heat. Table 7 shows the maximum % GMR and the signal-to-noise

ratio at different currents. As the current increased, so did the starting resistance due to

heating of the nanowires. The heat also leads to a decrease in the signal-to-noise ratio as

the current increased with a significant drop off at 4 mA.
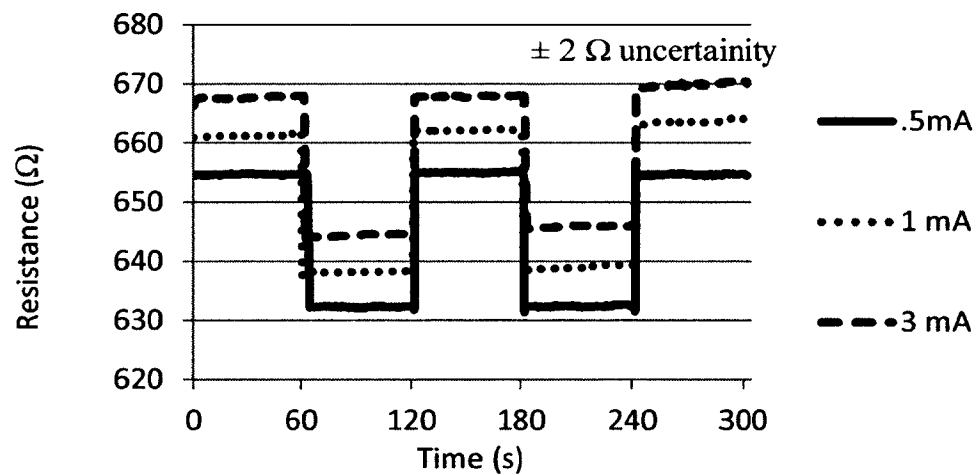


Figure 53: Resistance of the nanowire GMR thin film as a magnet was placed in close
proximity and then removed in 1-min intervals at .5 mA, 1 mA, and 3 mA
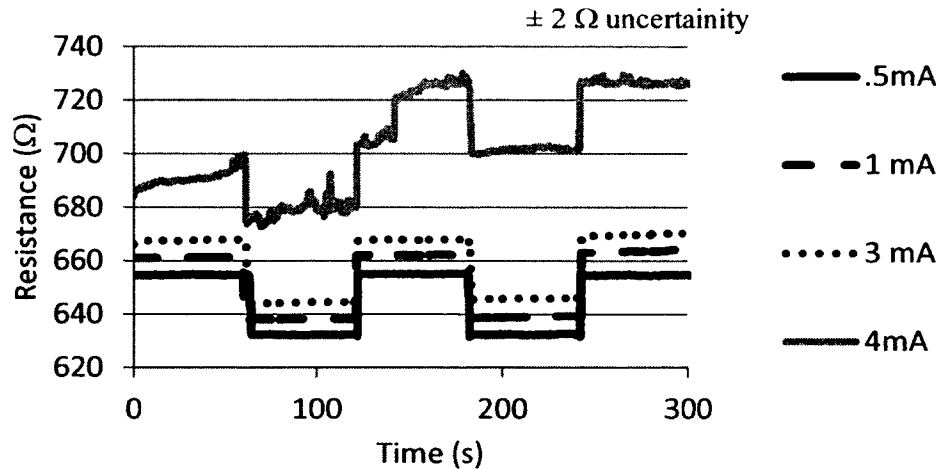
Figure 54: Resistance of the nanowire GMR thin film as a magnet was placed in close proximity and then removed in 1 min intervals at .5 mA, 1 mA, 3 mA and 4 mA

Table 7: Summary of data obtained from Figure 43

| Current | Starting Resistance (Ω) | %GMR | SNR |
|---------|------------------------|------|------|
| .5 mA | 654.5 | 3.63 | 33dB |
| 1 mA | 660.9 | 4.02 | 27dB |
| 3 mA | 666.2 | 4.04 | 26dB |
| 4 mA | 684.2 | - | - |

Figure 55 shows the GMR curve of the same thin film obtained by varying a magnetic field from ± 1 T. The graph is not completely smooth due to hysteresis, but there is a clear correlation between the magnetic field and resistance. Figure 56 shows a GMR curve of a magnetic sensor that had a more thorough oxidation removal procedure by increasing the time the thin film was exposed to the acid and current. As can be seen, the curve is a lot smoother, however the resistance is much lower and the curve is not as symmetric as the % GMR curve in Figure 55. The overall % MR change is roughly 5 % for both curves.
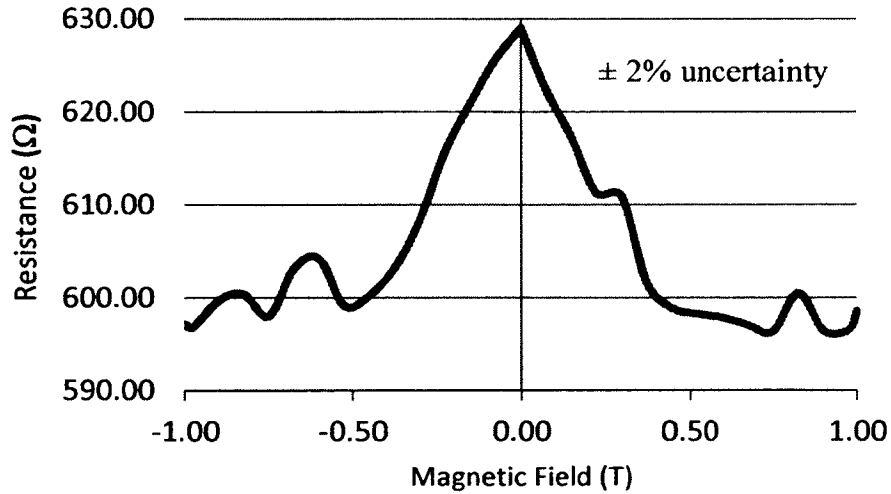
Figure 55: % GMR curve of nanowire-GMR magnetic sensor
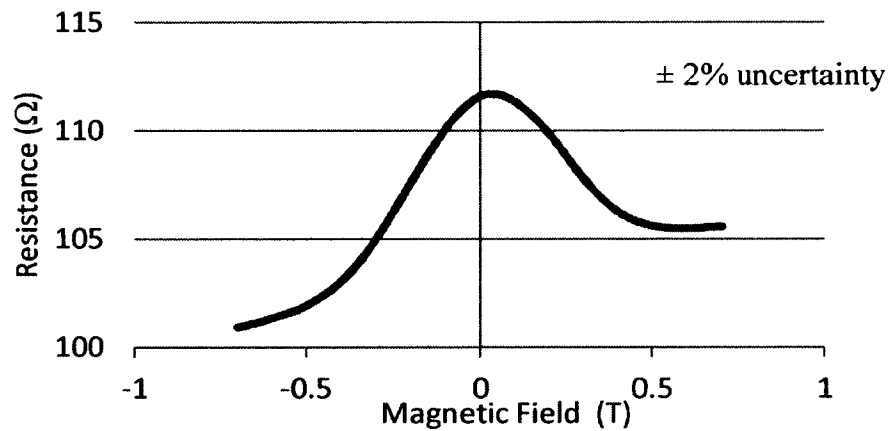


Figure 56: %GMR curve of nanowire GMR magnetic sensor after further oxidation removal

Figure 57 shows a MR curve of a sensor obtained by cycling the magnetic field from 0 to 1 T and then from 1 to -1 T and finally from -1 to1T. As can be seen the resistance increased for the same magnetic field values the longer the test was conducted. This increase in resistance could be due to the senor heating up. Another explanation could be the sensor has hysteresis and does not return to its zero state when no magnetic field is present.
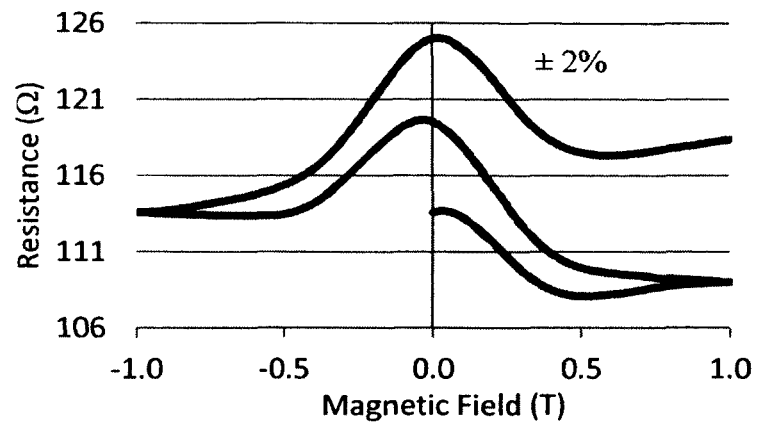
Figure 57: A MR curve obtained by a variable magnetic field from 0 to 1 T and then from 1 to -1 T and finally from -1 to1T.

# CHAPTER 9

## PERCOLATION THEORY

A simulation model was created in Matlab to determine the minimum density and length of nanowires needed for electrical conductivity of the thin film. If the nanowire density of the film was too low, the film was not able to conduct electricity. The amount of aggregation of the nanowires also affected the conductivity of the fabricated thin films, as seen in Figure 58.
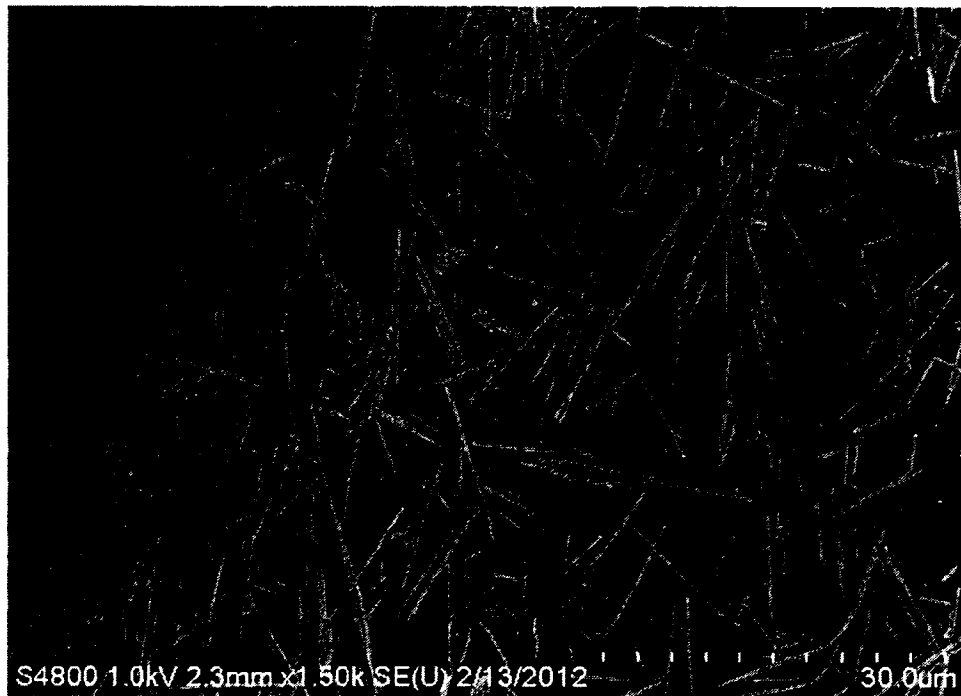


Figure 58: Example of deposited nanowires not suited for conductivity due to low density and aggregated nanowires

A branch of mathematics called percolation theory was utilized. Percolation theory allows users to solve problems dealing with the connectivity of randomly placed clusters. Each nanowire was treated as a stick or line segment with length $L$ in the percolation model. All nanowires have a random coordinate position $(x_i, y_i)$ on a grid and is assumed to be parallel to the substrate surface $(z_i=0)$. Every nanowire also has a random azimuthal orientation, $\pi \geq \theta_i \geq 0$, as seen in Figure 59.
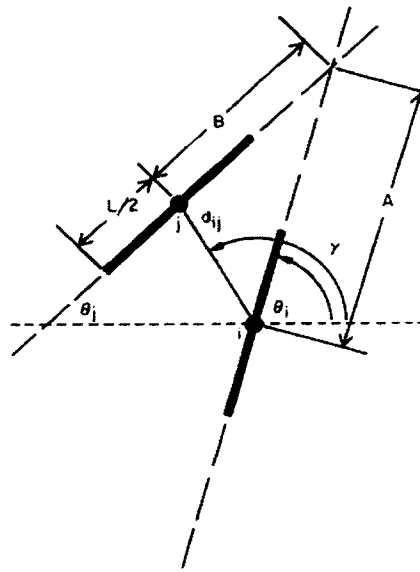


Figure 59: Diagram for determining bonding criterion for a nanowire percolation model. Each nanowire of length $L$ is centered on a site and has some randomly assigned orientation angle $\theta_i$. If bonding occurs when two nanowires overlap, then the bonding criterion is $A \leq L/2$ and $B \leq L/2$ [86]

Conductivity between two nanowires will occur when they overlap each other. A bonding model can be used to calculate when this occurs. When $B_{ij}$ from equation 8 equals 1, nanowire $i$ and $j$ overlap.

$$B_{ij} = H(L - 2A)H(L - 2B).$$ Eq. (9)

$$H(x) = \begin{cases} 0 & \text{if } x < 0 \\ 1 & \text{if } x \geq 0 \end{cases}.$$ Eq. (10)

$$A = d_{ij} \left| \frac{\sin(\gamma - \theta_j)}{\sin(\theta_i - \theta_j)} \right|.$$  Eq. (11)

$$B = d_{ij} \left| \frac{\sin(\gamma - \theta_i)}{\sin(\theta_i - \theta_j)} \right|.$$  Eq. (12)

$$\gamma = \tan^{-1} \left[ \frac{y_i - y_j}{x_i - x_j} \right].$$  Eq. (13)

$$d_{ij} = \sqrt{(x_i - x_j)^2 + (y_i - y_j)^2}.$$  Eq. (14)

Using the previous equations, a Matlab graphical user interface (GUI) was made to simulate the random nanowire networks. The GUI inputs were the number of nanowires, length of the nanowires, area of the sample, number of simulations, force field strength, and force field angle. The force field strength and angle simulated a magnetic field being used to align the nanowires in the direction of a magnetic field. Once the inputs were entered and a simulation was run, the GUI outputed the density (nanowires per $mm^2$), average connections per nanowire, standard deviation of the average number of connections per nanowire for each simulation, and the percentage of nanowires that were not connected to any other nanowries. Figure 60 and Figure 61 show screen shots of the Matlab GUI.
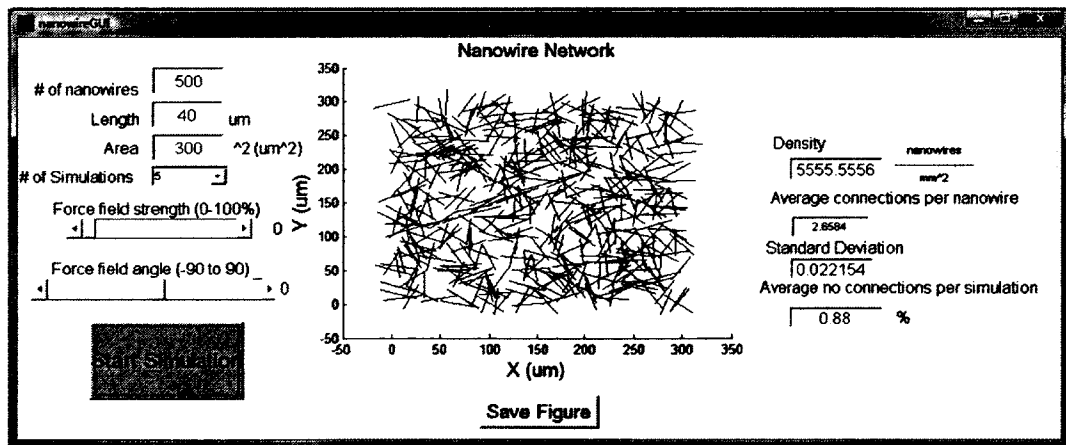


Figure 60: Matlab GUI interface
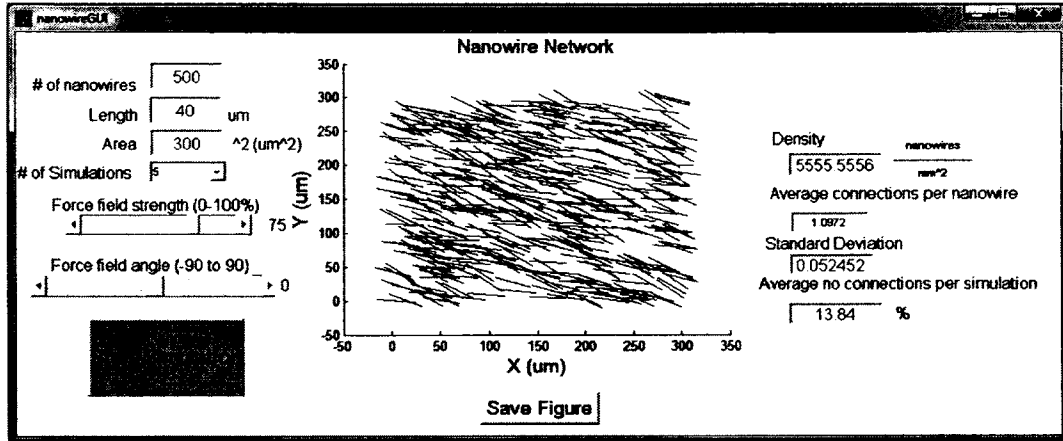
Figure 61: Matlab GUI interface with force field strength set to 75% and force field angle set to 0°

One of the reasons the Matlab GUI was created was to study how density and length of nanowires affected the conductivity of GMR thin films. As seen in Figure 62 and Table 8, as the nanowire density increases, the average number of connections per nanowire increased leading to more conductive paths for electrons to travel throughout the thin film. In addition to more conductive paths, increasing the density leads to a lower percentage of non-connected nanowires.
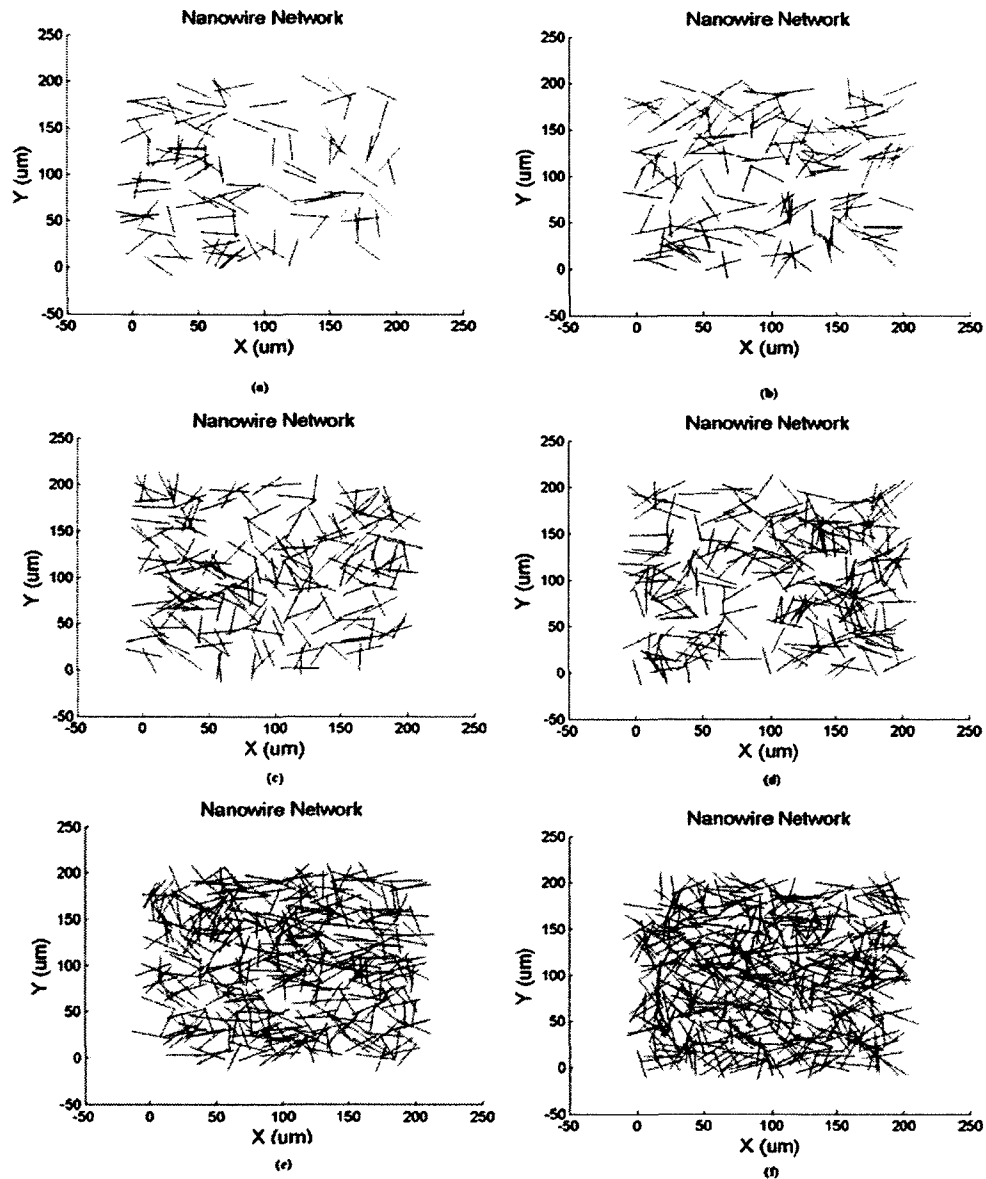
Figure 62: Nanowire networks with various densities (a) 2,500 nanowires/mm² (b) 3,750 nanowires/mm² (c) 5,000 nanowires/mm² (d) 6,250 nanowires/mm² (e) 10,000 nanowires/mm² (f) 12,500 nanowires/mm²

Table 8: Statistics for various densities of nanowires with uniform length

| Density (nanowires/mm$^2$) | Length (μm) | Average Connections | Standard Deviation | Average no connections |
|---|---|---|---|---|
| 2,500 | 30 | 0.619 | 0.0848 | 28.80% |
| 3,750 | 30 | 1.035 | 0.1009 | 15.60% |
| 5,000 | 30 | 1.261 | 0.0922 | 7.75% |
| 6,250 | 30 | 1.6588 | 0.0667 | 3.96% |
| 10,000 | 30 | 2.681 | 0.1074 | 0.65% |
| 12,500 | 30 | 3.3106 | 0.1047 | 0.20% |

Figure 63 shows simulations with a constant density of nanowires and various length nanowires (40μm, 60μm, 80μm and 100μm) in a 40,000μm$^2$ grid space. From the Figure, it can clearly be seen that increasing the length of the nanowires also increased the chances of overlapping nanowires, which increases the conductivity of the thin film. Table 9 shows statistics from the simulations.
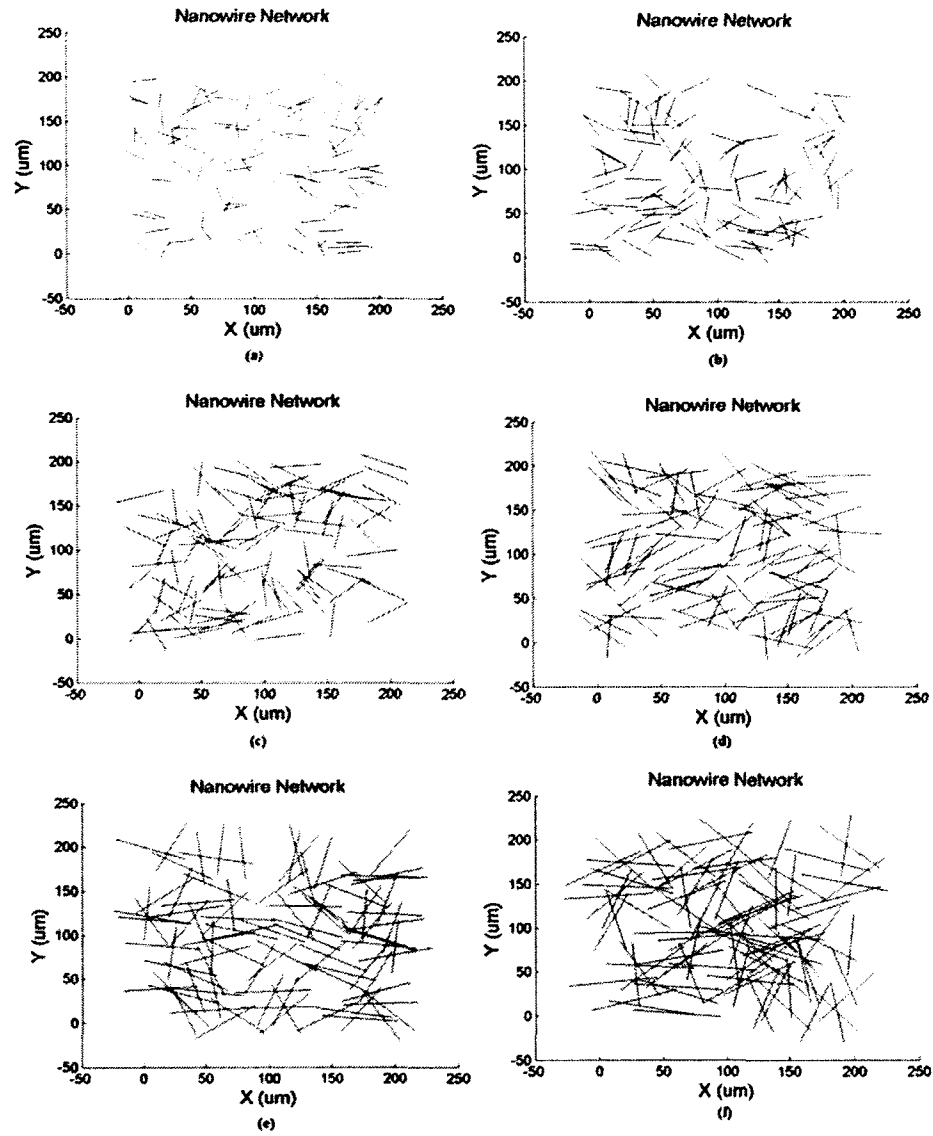
Figure 63: Nanowire network with various length nanowires (a) 20 μm (b) 30 μm (c) 40 μm (d) 50 μm (e) 60 μm (f) 70 μm

Table 9: Statistics for various lengths of nanowires with uniform densities

| Length (μm) | Density | Average Connections | Standard Deviation | Average no connections |
|---|---|---|---|---|
| 20 | 2500 | 0.29 | 0.086 | 54.70% |
| 30 | 2500 | 0.66 | 0.064 | 27.70% |
| 40 | 2500 | 1.11 | 0.091 | 9.30% |
| 50 | 2500 | 1.72 | 0.15 | 4.20% |
| 60 | 2500 | 2.531 | 0.177 | 0.80% |
| 70 | 2500 | 3.213 | 0.209 | 0.20% |
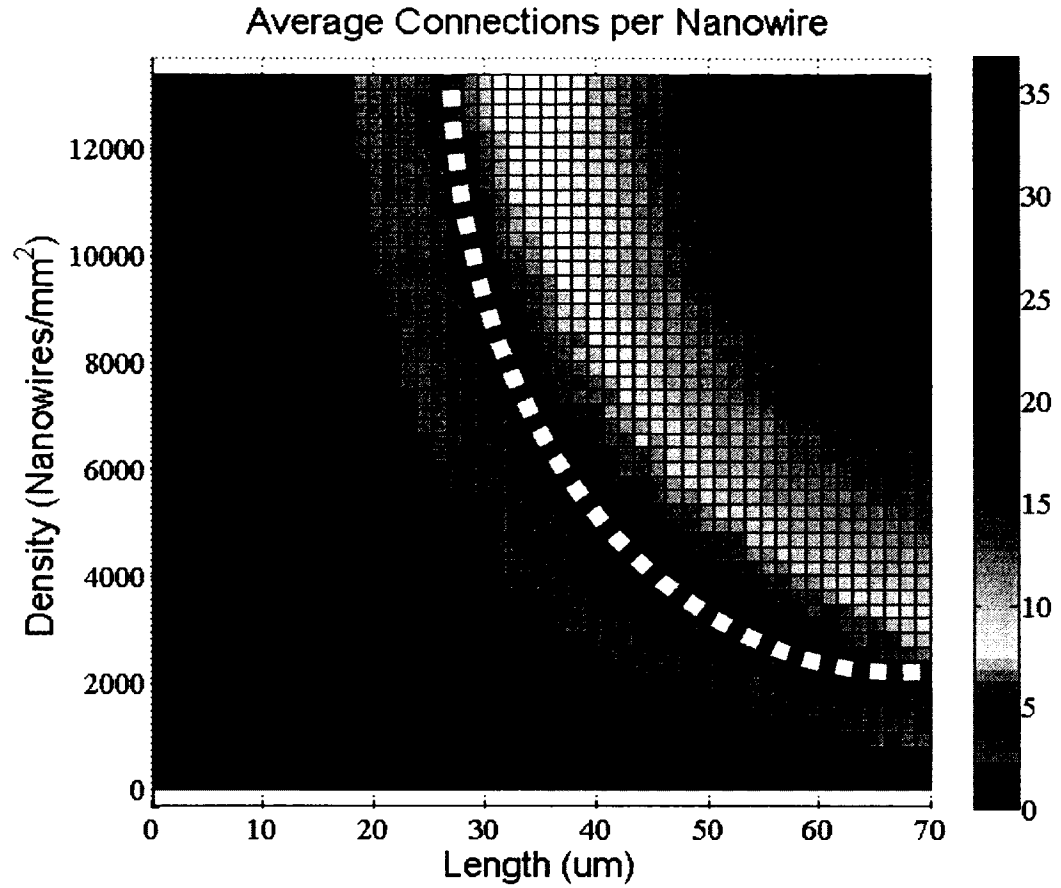
Figure 64: Plot showing how the length and density of nanowires affects the average number of connections per nanowire. The white dotted line corresponds to an average of 5 connections per nanowire.

# Chapter 10

## GMR NANOWIRE THIN FILM APPLICATIONS

### 10.1 Position sensor

Simple position sensors, created with nanowire GMR thin film magnetic sensors, were deposited on PET plastic in straight-line patterns. A magnet position could be tracked along the glass slide by the changing resistance of the nearest sensor, as seen in Figure 65, with actual fabricated sensing arrays in Figure 66. The 1D concept could be extended to 2D magnetic sensing arrays as well, as illustrated in Figure 67.
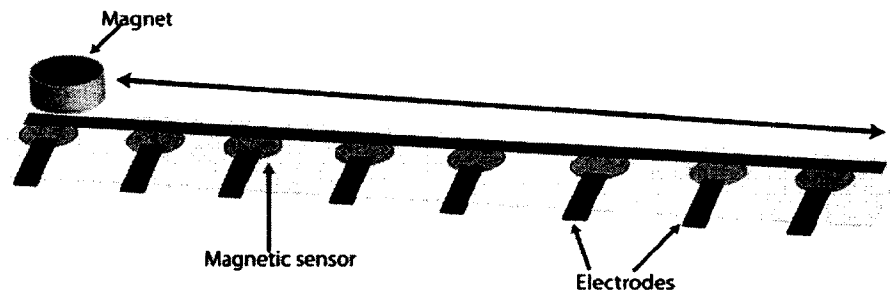
Figure 65: Position sensor concept
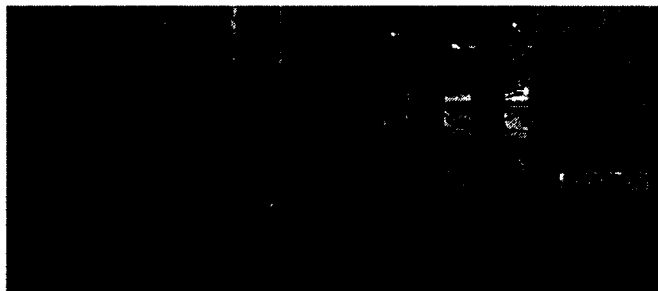
Figure 66: Fabricated 1D position sensor
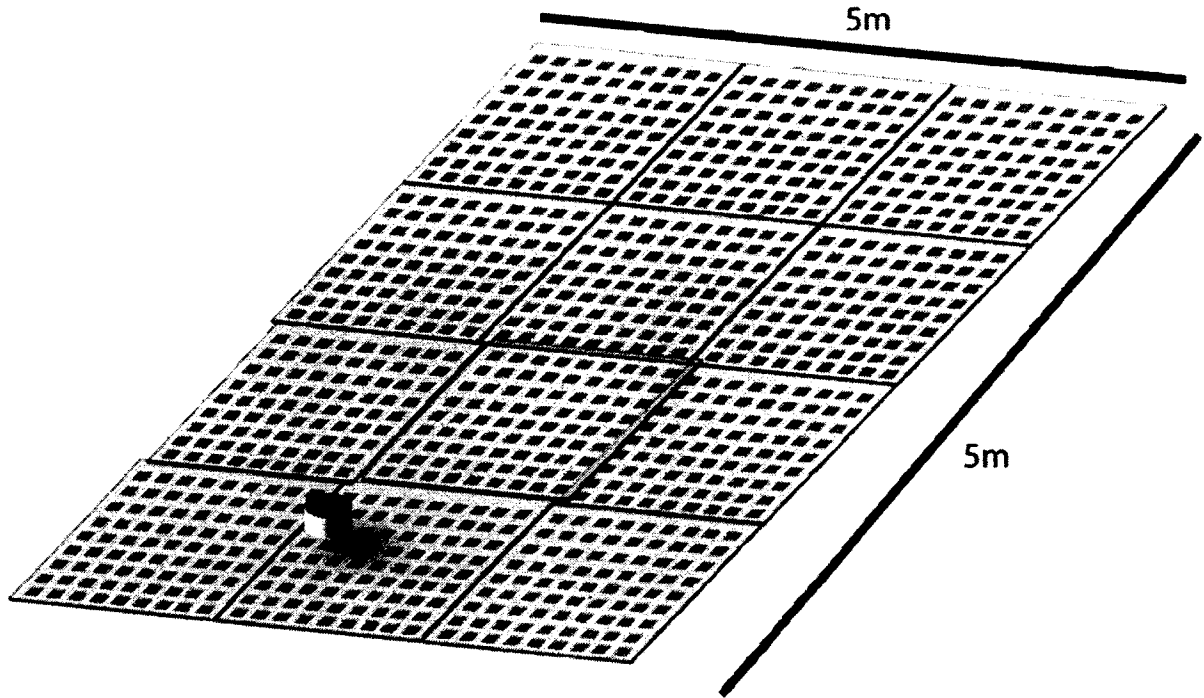
Large Scale Magnetic Sensing
Array

Figure 67: 2D magnetic sensor array concept

## 10.2 Touch/Pressure sensor

A low cost magnetic pressure sensor was created using a GMR nanowire thin film magnetic sensor. The pressure sensor consisted of a rubber gasket with a top rubber layer and a bottom metal layer. The metal layer had a GMR nanowire magnetic sensor with electrical contacts. The top rubber layer had a small neodymium magnet glued to its surface. When the top surface with the magnet was pressed, the magnet moved closer to the sensor creating a change in resistance of the magnetic sensor. Figure 68 illustrates the pressure sensor concept.
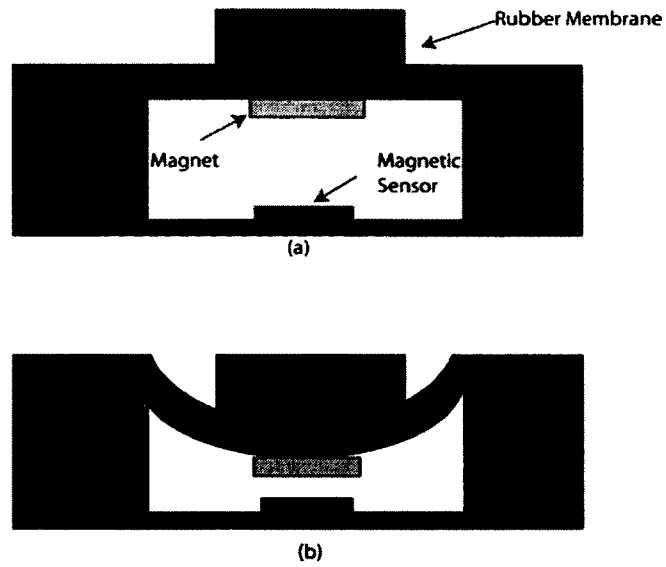
Figure 68: Illustration of pressure sensor concept (a) pressure sensor in normal state (b) pressure sensor in pressed state
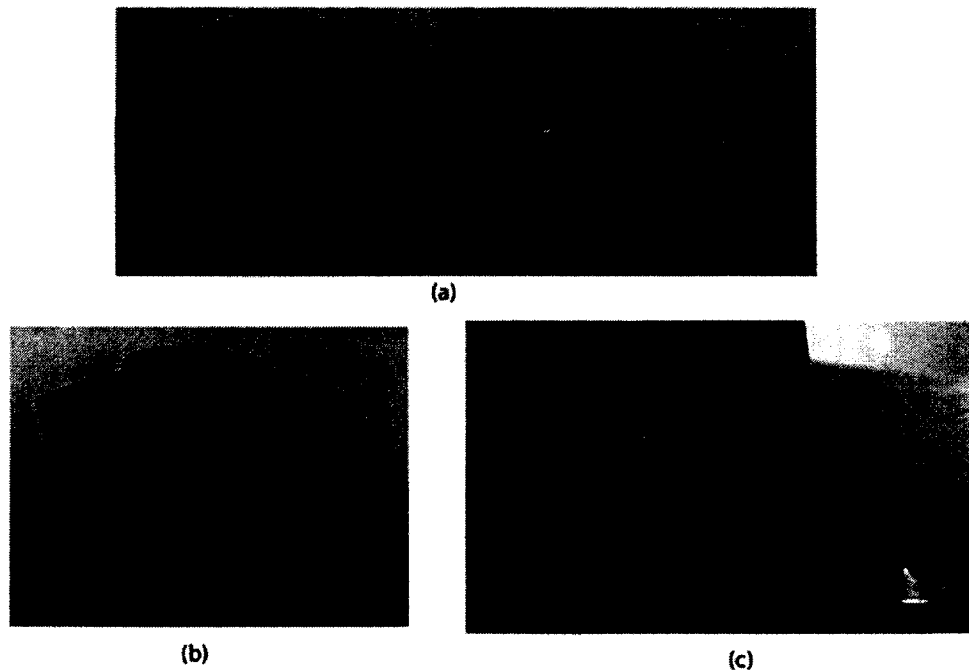


Figure 69: Photos of fabricated pressure sensor using GMR nanowire thin film magnetic sensor. (a) Top rubber part with magnet and bottom metal part with magnetic sensor (b) Pressure sensor in normal state (c) Pressure sensor in pressed state

Pressure sensors based on GMR nanowire thin films can be low cost and fabricated with variable pressure ranges depending on the flexibility and stiffness of the rubber membrane used for the diaphragm. Further research is needed to test the repeatability and sensitivity of the pressure sensor design. Figure 70 shows the output graph of the pressure sensor as it was pressed and depressed at approximately five second intervals.

**Pressure Sensor Output Graph**
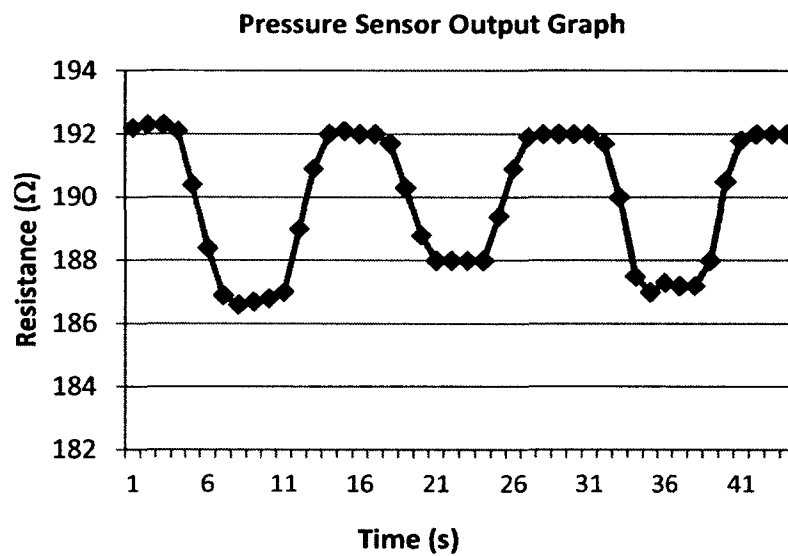
Figure 70: Output graph of pressure sensor with GMR nanowire thin film magnetic sensor

# CHAPTER 11

## CONCLUSION AND FUTURE WORK

The relative recent discovery of the GMR phenomenon has changed society in many ways. GMR sensors will have improvements made in their sensitivity as new materials and fabrication techniques are used for their manufacture. This work presented an elegant technique for the fabrication of CoNiFeCu/Cu multilayer GMR nanowire thin films for magnetic sensing applications. Using an electrodeposition technique, current perpendicular to plane (CPP) multilayer GMR nanowires were fabricated inside of nanoporous templates. After GMR nanowires are fabricated, they are transferred to receiving substrates, such as PET plastic, using a vacuum filtration technique and a PDMS stamp. Using this technique, each 3.4 $cm^2$ template yields sufficient nanowires for a GMR sensor coverage of approximately 300 $cm^2$. Additionally, the magnetic sensors were transparent, flexible, and scalable. The electrical sheet resistance of these sensors is approximately 100-10k $\Omega$ per square, with a %MR on the order of 5% at room temperature. It was found that the % MR was independent of the sheet resistance of the film. Operating the sensors at a higher current increased the % MR slightly but decreased the signal to noise ratio.

The advantages of magnetic sensors created with nanowire-GMR thin films versus traditional commercially available magnetic sensors are that these thin film sensors can be patterned on transparent and flexible substrates, are less expensive to

fabricate, require less power, and have a potentially higher signal to noise ratios than existing GMR sensor technologies. A low cost pressure and position sensor was created using nanowire magnetic sensors and the sensors could be turned into large arrays of pressure and position sensors for a variety of applications.

Future research includes studying how oxidation removal techniques, length and density of nanowires, nanowire composition, and annealing affect the performance of the magnetic sensors. In addition, different methods for applying GMR nanowire thin films to substrates will be tested, such as a spray coating technique and printing method.

Spray coating methods entail using an airbrush to evenly distribute GMR nanowires over substrate surfaces. Figure 71 shows a spray coating technique were an airbrush is used to coat a patterned PDMS stamp. After being coating with a thin layer of GMR nanowires, the stamp is then used to transfer the nanowires to a heated receiving substrate.
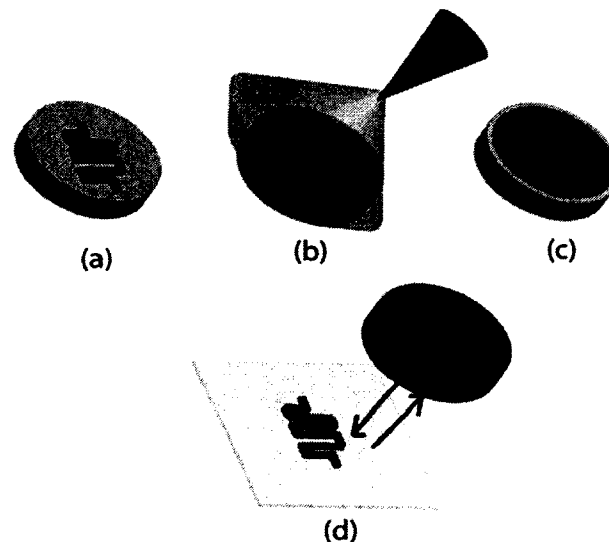


Figure 71: Spray coating method 1: (a) Patterned PDMS stamp (b) PDMS stamp being spray coated with GMR Nanowires (c) PDMS stamp with GMR Nanowire Thin Film (d) PDMS stamp transferring Nanowires to PET substrate

Figure 72 shows a spray coating technique that uses an airbrush to spray a PET

substrate with a patterned mask on top. After spraying the GMR nanowires, the mask can

be removed and the pattern that is left behind can be transferred to a receiving substrate

with a PDMS stamp.
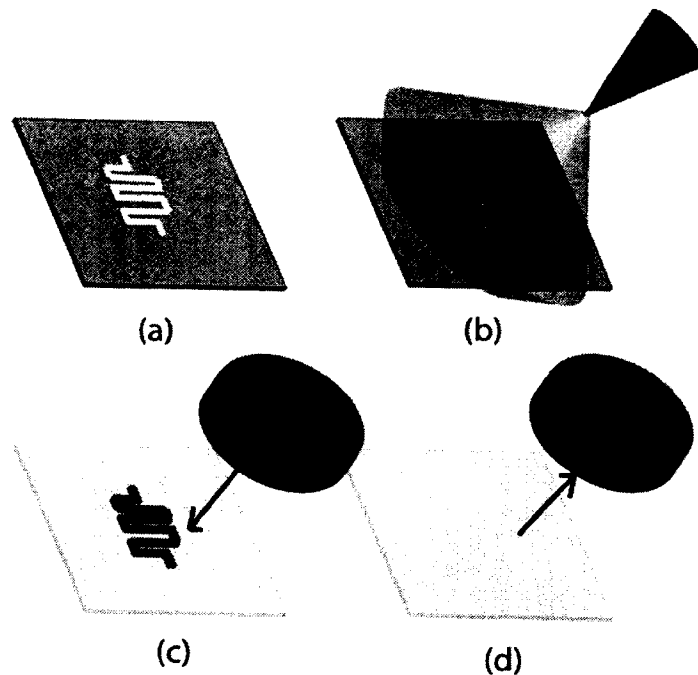


Figure 72: Spray Coating Thin Film Method 2 (a) PET substrate covered with pattered
Kapton tape (b) GMR nanowires being spray coated over the PET substrate
(c) PET substrate with the Kapton tape removed, leaving behind the nanowire
pattern (d) Blank PDMS stamp transferring the nanowires to a receiving
substrate

Another fast and economical way to create GMR nanowire magnetic sensors is to

print them directly to a substrate with a standard printer. This technique can be used to

create low cost custom-made position sensors that can be easily drawn on a computer and

printed.

**APPENDIX A:**

**CHARGE PER LAYER MATLAB CODE**

```
numOfPores = 900000000 %number of pores per membrane

%Nanowire Charactersitcs
N_length = 60*10^-6; %length of Nanowires in um
N_length2 = 30;
N_density = 8.9; %g/ml
N_diamter=200*10^-9;
N_volume = pi*(N_diamter/2)^2*N_length %volume of signle Nanowire
N_weight =  N_density*100*100*100*N_volume %weight of single Nanowire
(g)
total_weight = numOfPores*N_weight %total weight of all Nanowires

%Alloy Characerstics
average_oxidation = 2; %average oxidation number of metal ions
atomic_weight = 58.933195+(18*14); %approximate atomic weight of alloy
atomic_weight_copper = 63.546+(5*18); %approximate atomic weight of
copper

Columbs = ((total_weight/atomic_weight)*mole)*average_oxidation*eC
ColumbsC =
((total_weight/atomic_weight_copper)*mole)*average_oxidation*eC;

% ColumbPerLayer = (Layer/N_length2)*Columbs;
% ColumbPerLayer = (Layer/N_length2)*ColumbsC;

x =0:.001:.02;
ColumbPerLayer = (x/N_length2)*Columbs;
ColumbPerLayerC = (x/N_length2)*ColumbsC;
x=0:1:20;
plot(x,ColumbPerLayer,'x-',x,ColumbPerLayerC,'o-','LineWidth',2)
xlabel('Layer Thickness (nm)')
ylabel('Columbs')
title('Layer Thickness vs. Columbs')
hold on;
```

**APPENDIX B:**

**NANOWIRE DENSITY MATLAB GUI CODE**

```
function varargout = nanowireGUI(varargin)
% NANOWIREGUI M-file for nanowireGUI.fig
% NANOWIREGUI, by itself, creates a new NANOWIREGUI or raises the existing
% singleton*.
%
% H = NANOWIREGUI returns the handle to a new NANOWIREGUI or the handle to
% the existing singleton*.
%
% NANOWIREGUI('CALLBACK',hObject,eventData,handles,...) calls the local
% function named CALLBACK in NANOWIREGUI.M with the given input arguments.
%
% NANOWIREGUI('Property','Value',...) creates a new NANOWIREGUI or raises the
% existing singleton*.  Starting from the left, property value pairs are
%        applied to the GUI before nanowireGUI_OpeningFunction gets called.  An
%        unrecognized property name or invalid value makes property application
%        stop.  All inputs are passed to nanowireGUI_OpeningFcn via varargin.
%        *See GUI Options on GUIDE's Tools menu.  Choose "GUI allows only one
%        instance to run (singleton)".
% See also: GUIDE, GUIDATA, GUIHANDLES
% Edit the above text to modify the response to help nanowireGUI
% Last Modified by GUIDE v2.5 07-May-2012 18:59:22
% Begin initialization code - DO NOT EDIT

gui_Singleton = 1;
gui_State = struct('gui_Name',       mfilename, ...
                   'gui_Singleton',  gui_Singleton, ...
                   'gui_OpeningFcn', @nanowireGUI_OpeningFcn, ...
                   'gui_OutputFcn',  @nanowireGUI_OutputFcn, ...
                   'gui_LayoutFcn',  [] , ...
                   'gui_Callback',   []);
if nargin && ischar(varargin{1})
    gui_State.gui_Callback = str2func(varargin{1});
end

if nargout
    [varargout{1:nargout}] = gui_mainfcn(gui_State, varargin{:});
else
    gui_mainfcn(gui_State, varargin{:});
end
% End initialization code - DO NOT EDIT

% --- Executes just before nanowireGUI is made visible.
function nanowireGUI_OpeningFcn(hObject, eventdata, handles, varargin)
% This function has no output args, see OutputFcn.
% hObject     handle to figure
% eventdata   reserved - to be defined in a future version of MATLAB
% handles     structure with handles and user data (see GUIDATA)
% varargin    command line arguments to nanowireGUI (see VARARGIN)

% Choose default command line output for nanowireGUI
handles.output = hObject;

% Update handles structure
guidata(hObject, handles);

% UIWAIT makes nanowireGUI wait for user response (see UIRESUME)
% uiwait(handles.figure1);


% --- Outputs from this function are returned to the command line.
function varargout = nanowireGUI_OutputFcn(hObject, eventdata, handles)
% varargout  cell array for returning output args (see VARARGOUT);
% hObject    handle to figure
```

```
% eventdata   reserved - to be defined in a future version of MATLAB
% handles     structure with handles and user data (see GUIDATA)

% Get default command line output from handles structure
varargout{1} = handles.output;

function numOfNanowires_Callback(hObject, eventdata, handles)
% hObject     handle to numOfNanowires (see GCBO)
% eventdata   reserved - to be defined in a future version of MATLAB
% handles     structure with handles and user data (see GUIDATA)

% Hints: get(hObject,'String') returns contents of numOfNanowires as text
%        str2double(get(hObject,'String')) returns contents of numOfNanowires
as a double

num = get(hObject,'String');
set(hObject,'UserData',str2num(num));

% --- Executes during object creation, after setting all properties.
function numOfNanowires_CreateFcn(hObject, eventdata, handles)
% hObject     handle to numOfNanowires (see GCBO)
% eventdata   reserved - to be defined in a future version of MATLAB
% handles     empty - handles not created until after all CreateFcns called

% Hint: edit controls usually have a white background on Windows.
%       See ISPC and COMPUTER.
if ispc && isequal(get(hObject,'BackgroundColor'),
get(0,'defaultUicontrolBackgroundColor'))
    set(hObject,'BackgroundColor','white');
end

function lengthOfNanowires_Callback(hObject, eventdata, handles)
% hObject     handle to lengthOfNanowires (see GCBO)
% eventdata   reserved - to be defined in a future version of MATLAB
% handles     structure with handles and user data (see GUIDATA)

% Hints: get(hObject,'String') returns contents of lengthOfNanowires as text
%        str2double(get(hObject,'String')) returns contents of
lengthOfNanowires as a double
num = get(hObject,'String');
set(hObject,'UserData',str2num(num));

% --- Executes during object creation, after setting all properties.
function lengthOfNanowires_CreateFcn(hObject, eventdata, handles)
% hObject     handle to lengthOfNanowires (see GCBO)
% eventdata   reserved - to be defined in a future version of MATLAB
% handles     empty - handles not created until after all CreateFcns called

% Hint: edit controls usually have a white background on Windows.
%       See ISPC and COMPUTER.
if ispc && isequal(get(hObject,'BackgroundColor'),
get(0,'defaultUicontrolBackgroundColor'))
    set(hObject,'BackgroundColor','white');
end

function Area_Callback(hObject, eventdata, handles)
% hObject     handle to Area (see GCBO)
% eventdata   reserved - to be defined in a future version of MATLAB
% handles     structure with handles and user data (see GUIDATA)

% Hints: get(hObject,'String') returns contents of Area as text
%        str2double(get(hObject,'String')) returns contents of Area as a double
num = get(hObject,'String');
```

```
set(hObject,'UserData',str2num(num));

% --- Executes during object creation, after setting all properties.
function Area_CreateFcn(hObject, eventdata, handles)
% hObject    handle to Area (see GCBO)
% eventdata  reserved - to be defined in a future version of MATLAB
% handles    empty - handles not created until after all CreateFcns called

% Hint: edit controls usually have a white background on Windows.
%       See ISPC and COMPUTER.
if ispc && isequal(get(hObject,'BackgroundColor'),
get(0,'defaultUicontrolBackgroundColor'))
    set(hObject,'BackgroundColor','white');
end

 % --- Executes on selection change in numOfSimulations.
function numOfSimulations_Callback(hObject, eventdata, handles)
% hObject    handle to numOfSimulations (see GCBO)
% eventdata  reserved - to be defined in a future version of MATLAB
% handles    structure with handles and user data (see GUIDATA)

% Hints: contents = get(hObject,'String') returns numOfSimulations contents as
cell array
%        contents{get(hObject,'Value')} returns selected item from
numOfSimulations
val = get(hObject,'Value');
string_list = get(hObject,'String');
selected_string = string_list{val};
set(hObject,'UserData',str2num(selected_string));

% --- Executes during object creation, after setting all properties.
function numOfSimulations_CreateFcn(hObject, eventdata, handles)
% hObject    handle to numOfSimulations (see GCBO)
% eventdata  reserved - to be defined in a future version of MATLAB
% handles    empty - handles not created until after all CreateFcns called

% Hint: popupmenu controls usually have a white background on Windows.
%       See ISPC and COMPUTER.
if ispc && isequal(get(hObject,'BackgroundColor'),
get(0,'defaultUicontrolBackgroundColor'))
    set(hObject,'BackgroundColor','white');
end

% --- Executes on button press in StartButton.
function StartButton_Callback(hObject, eventdata, handles)
% hObject    handle to StartButton (see GCBO)
% eventdata  reserved - to be defined in a future version of MATLAB
% handles    structure with handles and user data (see GUIDATA)
axes(handles.axes1)
cla(handles.axes1,'reset')
GridSize =get(handles.Area,'UserData'); %Size of Grid for Nanowires
Samples =get(handles.numOfNanowires,'UserData'); %# of Nanowires
L=get(handles.lengthOfNanowires,'UserData'); %Length of Nanowires
firstTime=0;

set(handles.density,'String',num2str((Samples/(GridSize*10^-3)^2)));
%startBuffer = zeros(Samples/5,1);
list=get(handles.numOfSimulations,'String');
val=get(handles.numOfSimulations,'Value');
str=list{val};
maxSim=str2num(str);
average=zeros(maxSim,1);
zeroConnects=zeros(maxSim,1);
```

```
warning off all;
for simCount=1:1:maxSim
XY = rand(Samples,2)*GridSize;
XY = sortrows(XY,1);
angles=(get(handles.ForceFieldAngle,'Value')/180*pi)-
(rand(Samples,1)*pi)*((100-get(handles.FieldStrength,'Value'))/100);
%angles = rand(Samples,1)*pi;
d= zeros(Samples,Samples);
A = zeros(Samples,Samples);
B = zeros(Samples,Samples);
C = zeros(Samples,Samples);
y = zeros(Samples,Samples);
count=0;
count2=0;
    for i=1:1:Samples-1
        for j=1:1:Samples
            if i~=j
                d(i,j)=sqrt((XY(i,1)-XY(j,1))^2+(XY(i,2)-XY(j,2))^2);
            end
        end
    end
    for j=1:1:Samples
            d(Samples,j)=sqrt((XY(Samples,1)-XY(j,1))^2+(XY(Samples,2)-
XY(j,2))^2);
    end


    for i=1:1:Samples-1
        for j=1:1:Samples
            if i~=j
                y(i,j)= atan((XY(i,2)-XY(j,2))/(XY(i,1)-XY(j,1)));
            end
        end
    end
    for j=1:1:Samples
        y(Samples,j)= atan((XY(Samples,2)-XY(j,2))/(XY(Samples,1)-XY(j,1)));
    end

    for i=1:1:Samples
        for j=1:1:Samples
            if i~=j
                A(i,j) = d(i,j)*abs((sin(y(i,j)-angles(j,1)))/(sin(angles(i,1)-
angles(j,1))));
            end

        end
    end

    for i=1:1:Samples
        for j=1:1:Samples
            if i~=j
                B(i,j) = d(i,j)*abs((sin(y(i,j)-angles(i,1)))/(sin(angles(i,1)-
angles(j,1))));
            end
        end
    end

    for i=1:1:Samples
        for j=1:1:Samples
            if ((L-2*A(i,j))>0) && ((L-2*B(i,j))>0)&& i~=j
                B(i,j)=1;
            else
```

```
                        B(i,j)=0;
                end
            end
    end
    if firstTime==0
        firstTime=1;
            X1 = zeros(Samples,1);
            X2 = zeros(Samples,1);
            Y1 = zeros(Samples,1);
            Y2 = zeros(Samples,1);
            deltaX = zeros(Samples,1);
            deltaY = zeros(Samples,1);
            %f = figure();
            %axes(handles.axes1)
            hold on

            for i=1:1:Samples
                if angles(i)>(pi/2)
                    deltaX(i,1)= (L/2)*cos(pi-angles(i));
                    deltaY(i,1)= (L/2)*sin(pi-angles(i));
                    X1(i,1)=XY(i,1)-deltaX(i,1);
                    X2(i,1)=XY(i,1)+deltaX(i,1);
                    Y1(i,1)=XY(i,2)+deltaY(i,1);
                    Y2(i,1)=XY(i,2)-deltaY(i,1);
                    plot([X1(i,1),X2(i,1)],[Y1(i,1),Y2(i,1)]);
                else
                    deltaX(i,1)= (L/2)*cos(angles(i));
                    deltaY(i,1) = (L/2)*sin(angles(i));
                    X1(i,1)=XY(i,1)+deltaX(i,1);
                    X2(i,1)=XY(i,1)-deltaX(i,1);
                    Y1(i,1)=XY(i,2)+deltaY(i,1);
                    Y2(i,1)=XY(i,2)-deltaY(i,1);
                    plot([X1(i,1),X2(i,1)],[Y1(i,1),Y2(i,1)]);
                end
            end

            for i=1:1:Samples
                for j=1:1:Samples
                    if B(i,j) ==1
                        count=count+1;
                        plot(XY(i,1),XY(i,2),'LineWidth',4)
                    end
                end
            end
            xlabel('X (um)')
            ylabel('Y (um)')
            title('Nanowire Network')
    end


    D=sum(B);
    zeroCount=0;
    for i=1:1:Samples
        if D(1,i)==0
            zeroCount=zeroCount+1;
        end
    end

 average(simCount,1)=(mean(sum(B))/2);
 zeroConnects(simCount,1)=((zeroCount/Samples)*100);


end
set(handles.averageConnections,'String',num2str(mean(average)));
```

```
set(handles.medianConnections,'String',num2str(median(sum(B))/2));
zeroCount=(num2str((zeroCount/Samples)*100));
set(handles.averageNoConnections,'String',num2str(mean(zeroConnects)));
hhh=num2str(std(average));
set(handles.standardDeviation,'String',num2str(std(average)));
dsfsd=2;


function averageConnections_Callback(hObject, eventdata, handles)
% hObject    handle to averageConnections (see GCBO)
% eventdata  reserved - to be defined in a future version of MATLAB
% handles    structure with handles and user data (see GUIDATA)


% Hints: get(hObject,'String') returns contents of averageConnections as text
%        str2double(get(hObject,'String')) returns contents of
averageConnections as a double


 % --- Executes during object creation, after setting all properties.
function averageConnections_CreateFcn(hObject, eventdata, handles)
% hObject    handle to averageConnections (see GCBO)
% eventdata  reserved - to be defined in a future version of MATLAB
% handles    empty - handles not created until after all CreateFcns called


% Hint: edit controls usually have a white background on Windows.
%       See ISPC and COMPUTER.
if ispc && isequal(get(hObject,'BackgroundColor'),
get(0,'defaultUicontrolBackgroundColor'))
    set(hObject,'BackgroundColor','white');
end


 function medianConnections_Callback(hObject, eventdata, handles)
% hObject    handle to medianConnections (see GCBO)
% eventdata  reserved - to be defined in a future version of MATLAB
% handles    structure with handles and user data (see GUIDATA)


% Hints: get(hObject,'String') returns contents of medianConnections as text
%        str2double(get(hObject,'String')) returns contents of
medianConnections as a double


 % --- Executes during object creation, after setting all properties.
function medianConnections_CreateFcn(hObject, eventdata, handles)
% hObject    handle to medianConnections (see GCBO)
% eventdata  reserved - to be defined in a future version of MATLAB
% handles    empty - handles not created until after all CreateFcns called


% Hint: edit controls usually have a white background on Windows.
%       See ISPC and COMPUTER.
if ispc && isequal(get(hObject,'BackgroundColor'),
get(0,'defaultUicontrolBackgroundColor'))
    set(hObject,'BackgroundColor','white');
end


 % --- Executes on slider movement.
function ForceFieldAngle_Callback(hObject, eventdata, handles)
% hObject    handle to ForceFieldAngle (see GCBO)
% eventdata  reserved - to be defined in a future version of MATLAB
% handles    structure with handles and user data (see GUIDATA)


% Hints: get(hObject,'Value') returns position of slider
%        get(hObject,'Min') and get(hObject,'Max') to determine range of slider
set(handles.text20,'String',(num2str(get(hObject,'Value'))));


% --- Executes during object creation, after setting all properties.
function ForceFieldAngle_CreateFcn(hObject, eventdata, handles)
```

```
% hObject      handle to ForceFieldAngle (see GCBO)
% eventdata    reserved - to be defined in a future version of MATLAB
% handles      empty - handles not created until after all CreateFcns called

% Hint: slider controls usually have a light gray background.
if isequal(get(hObject,'BackgroundColor'),
get(0,'defaultUicontrolBackgroundColor'))
    set(hObject,'BackgroundColor',[.9 .9 .9]);
end


% --- Executes on slider movement.
function FieldStrength_Callback(hObject, eventdata, handles)
% hObject      handle to FieldStrength (see GCBO)
% eventdata    reserved - to be defined in a future version of MATLAB
% handles      structure with handles and user data (see GUIDATA)

% Hints: get(hObject,'Value') returns position of slider
%        get(hObject,'Min') and get(hObject,'Max') to determine range of slider
set(handles.text19,'String',(num2str(get(hObject,'Value'))));

% --- Executes during object creation, after setting all properties.
function FieldStrength_CreateFcn(hObject, eventdata, handles)
% hObject      handle to FieldStrength (see GCBO)
% eventdata    reserved - to be defined in a future version of MATLAB
% handles      empty - handles not created until after all CreateFcns called

% Hint: slider controls usually have a light gray background.
if isequal(get(hObject,'BackgroundColor'),
get(0,'defaultUicontrolBackgroundColor'))
    set(hObject,'BackgroundColor',[.9 .9 .9]);
end


 function averageNoConnections_Callback(hObject, eventdata, handles)
% hObject      handle to averageNoConnections (see GCBO)
% eventdata    reserved - to be defined in a future version of MATLAB
% handles      structure with handles and user data (see GUIDATA)

% Hints: get(hObject,'String') returns contents of averageNoConnections as text
%        str2double(get(hObject,'String')) returns contents of
averageNoConnections as a double

% --- Executes during object creation, after setting all properties.
function averageNoConnections_CreateFcn(hObject, eventdata, handles)
% hObject      handle to averageNoConnections (see GCBO)
% eventdata    reserved - to be defined in a future version of MATLAB
% handles      empty - handles not created until after all CreateFcns called

% Hint: edit controls usually have a white background on Windows.
%        See ISPC and COMPUTER.
if ispc && isequal(get(hObject,'BackgroundColor'),
get(0,'defaultUicontrolBackgroundColor'))
    set(hObject,'BackgroundColor','white');
end


 function edit7_Callback(hObject, eventdata, handles)
% hObject      handle to edit7 (see GCBO)
% eventdata    reserved - to be defined in a future version of MATLAB
% handles      structure with handles and user data (see GUIDATA)

% Hints: get(hObject,'String') returns contents of edit7 as text
%        str2double(get(hObject,'String')) returns contents of edit7 as a
double
```

```
% --- Executes during object creation, after setting all properties.
function edit7_CreateFcn(hObject, eventdata, handles)
% hObject    handle to edit7 (see GCBO)
% eventdata  reserved - to be defined in a future version of MATLAB
% handles    empty - handles not created until after all CreateFcns called

% Hint: edit controls usually have a white background on Windows.
%       See ISPC and COMPUTER.
if ispc && isequal(get(hObject,'BackgroundColor'),
get(0,'defaultUicontrolBackgroundColor'))
    set(hObject,'BackgroundColor','white');
end


function edit8_Callback(hObject, eventdata, handles)
% hObject    handle to edit8 (see GCBO)
% eventdata  reserved - to be defined in a future version of MATLAB
% handles    structure with handles and user data (see GUIDATA)

% Hints: get(hObject,'String') returns contents of edit8 as text
%        str2double(get(hObject,'String')) returns contents of edit8 as a
double


% --- Executes during object creation, after setting all properties.
function edit8_CreateFcn(hObject, eventdata, handles)
% hObject    handle to edit8 (see GCBO)
% eventdata  reserved - to be defined in a future version of MATLAB
% handles    empty - handles not created until after all CreateFcns called

% Hint: edit controls usually have a white background on Windows.
%       See ISPC and COMPUTER.
if ispc && isequal(get(hObject,'BackgroundColor'),
get(0,'defaultUicontrolBackgroundColor'))
    set(hObject,'BackgroundColor','white');
end


function density_Callback(hObject, eventdata, handles)
% hObject    handle to density (see GCBO)
% eventdata  reserved - to be defined in a future version of MATLAB
% handles    structure with handles and user data (see GUIDATA)

% Hints: get(hObject,'String') returns contents of density as text
%        str2double(get(hObject,'String')) returns contents of density as a
double


% --- Executes during object creation, after setting all properties.
function density_CreateFcn(hObject, eventdata, handles)
% hObject    handle to density (see GCBO)
% eventdata  reserved - to be defined in a future version of MATLAB
% handles    empty - handles not created until after all CreateFcns called

% Hint: edit controls usually have a white background on Windows.
%       See ISPC and COMPUTER.
if ispc && isequal(get(hObject,'BackgroundColor'),
get(0,'defaultUicontrolBackgroundColor'))
    set(hObject,'BackgroundColor','white');
end


function standardDeviation_Callback(hObject, eventdata, handles)
% hObject    handle to standardDeviation (see GCBO)
% eventdata  reserved - to be defined in a future version of MATLAB
% handles    structure with handles and user data (see GUIDATA)
```

```
% Hints: get(hObject,'String') returns contents of standardDeviation as text
%        str2double(get(hObject,'String')) returns contents of
standardDeviation as a double

% --- Executes during object creation, after setting all properties.
function standardDeviation_CreateFcn(hObject, eventdata, handles)
% hObject    handle to standardDeviation (see GCBO)
% eventdata  reserved - to be defined in a future version of MATLAB
% handles    empty - handles not created until after all CreateFcns called

% Hint: edit controls usually have a white background on Windows.
%       See ISPC and COMPUTER.
if ispc && isequal(get(hObject,'BackgroundColor'),
get(0,'defaultUicontrolBackgroundColor'))
    set(hObject,'BackgroundColor','white');
end
```

# REFERENCES

[1]     Kostoff, R.N., R.G. Koytcheff, and C.G.Y. Lau, *Global nanotechnology research literature overview*. Technological Forecasting and Social Change, 2007. **74** (9): p. 1733-1747.

[2]     Wang, J. and P. Dortmans, *A review of selected nanotechnology topics and their potential military applications* 2004, Defence Science and Technology Organisation Salisbury (Australia) Systems Sciences Lab.

[3]     *Peter Grünberg - Autobiography*. Nobelprize.org, 2007.

[4]     Osaka, T., *Electrodeposition of highly functional thin films for magnetic recording devices of the next century*. Electrochimica Acta, 2000. **45** (20): p. 3311-3321.

[5]     Sulitanu, N.D., *Electrochemical deposition of novel nanostructured magnetic thin films for advanced applications*. Materials Science and Engineering B, 2002. **95**(3): p. 230-235.

[6]     Wang, Z.L., Y. Liu, and Z. Zhang, *Handbook of nanophase and nanostructured materials*, 2003, New York: Kluwer Academic/Plenum.

[7]     Nagasaka, K., *CPP-GMR technology for magnetic read heads of future high-density recording systems*. Journal of Magnetism and Magnetic Materials, 2009. **321**(6): p. 508-511.

[8]     Takagishi, M., et al., *The applicability of CPP-GMR heads for magnetic recording*. Magnetics, IEEE Transactions on, 2002. **38**(5): p. 2277-2282.

[9]     Pratt, W.P., et al., *Perpendicular giant magnetoresistances of Ag/Co multilayers*. Physical Review Letters, 1991. **66**(23): p. 3060.

[10]    Ross, C.A., *Electrodeposited multilayer thin films*. Annual Review of Materials Science, 1994. **24**: p. 159-188.

[11]    Wood, R., *Future hard disk drive systems*. Journal of Magnetism and Magnetic Materials, 2009. **321**(6): p. 555-561.

[12]    Thomson, W., *On the Electric Conductivity of Commercial Copper of Various Kinds*. Proceedings of the Royal Society of London, 1856. **8**: p. 550-555.

[13]    Nickel, J., *Magnetoresistance overview*. Vol. HPL-95-60. 1995: HP.

[14]    Jose, M. and C. Prieto, *Magnetic and electric properties of systems with colossal magnetoresistance*, in *Instituto de Ciencia de Materiales de Madrid (CSIC)*, 2001, Universidad Autonoma de Madrid.

[15]    Evans, P.R., G. Yi, and W. Schwarzacher, *Current perpendicular to plane giant magnetoresistance of multilayered nanowires electrodeposited in anodic aluminum oxide membranes*. Applied Physics Letters, 2000. **76** (4): p. 481-483.

[16]    Narisetti, R., in *Wall Street Journal* 1997. p. B8.

[17]    Julliere, M., *Tunneling between ferromagnetic films*. Physics Letters A, 1975. **54** (3): p. 225-226.

[18]    Jonker, G.H. and J. Van Santen, H, Physica, 1950. **16**: p. 377.

[19]    Baibich, M.N., et al., *Giant magnetoresistance of (001)Fe/(001)Cr magnetic superlattices*. Physical Review Letters, 1988. **61** (21): p. 2472.

[20]    Mott, N.F., *Electrons in transition metals*. Advanced Physics, 1964. **13**: p. 325.

[21]    Parkin, S.S.P., *Giant Magnetoresistance in Magnetic Nanostructures*. Annual Review of Materials Science, 1995. **25**(1): p. 357-388.

[22]    Zhang, J., et al., *Electrochemical inspection of electrodeposited giant magnetoresistance CoNiCu/Cu multilayer films*. Journal of The Electrochemical Society, 2005. **152**(9): p. C626-C630.

[23]    Gong, J., W.H. Butler, and G. Zangari, *High magnetoresistive sensitivity in electrodeposited FeCoNi/Cu multilayers*. Applied Physics Letters, 2005. **87**(1): p. 012505-012505-3.

[24]    Elshabini-Riad, A.A.R. and F.D. Barlow, *Thin film technology handbook*, 1998, New York: McGraw-Hill.

[25]    *On the path to full spectrum photovoltaic solar cells*. New Energy and Fuel, 2010.

[26]    Camarero, J., et al., *Surfactant-mediated modification of the magnetic properties of Co/Cu (111) thin films and superlattices*. Physical Review Letters, 1996. **76** (23): p. 4428-4431.

[27]    Mao, M., et al., *GMR in DC magnetron sputtered Ni{sub 81}Fe{sub 19}/Cu multilayers*. Journal Name: IEEE Transactions on Magnetics; Journal Volume: 34; Journal Issue: 4Pt1; Conference: 7. joint MMM-intermag conference, San Francisco, CA (United States), 6-9 Jan 1998;  p. 915-917.

[28]    Valet, T. and A. Fert, *Theory of the perpendicular magnetoresistance in magnetic multilayers*. Physical Review B  1993. **48** (10): p. 7099.

[29]    Blondel, A., et al., *Giant magnetoresistance of nanowires of multilayers*. Applied Physics Letters, 1994. **65** (23): p. 3019-3021.

[30]    Dubois, S., et al., *Evidence for a short spin diffusion length in permalloy from the giant magnetoresistance of multilayered nanowires*. Physical Review B, 1999. **60** (1): p. 477.

[31]    Piraux, L., et al., *Anisotropic transport and magnetic properties of arrays of sub-micron wires*. Journal of Magnetism and Magnetic Materials, 1997. **165** (1-3): p. 352-355.

[32]    Piraux, L., et al., *Giant magnetoresistance in magnetic multilayered nanowires*. Applied Physics Letters, 1994. **65**.

[33]    Davis, D., et al., *Electrodeposited, GMR CoNiFeCu Nanowires and Nanotubes from Electrolytes Maintained at Different Temperatures*. Journal of The Electrochemical Society, 2010. **157** (6): p. D317-D322.

[34]    Liu, K., et al., *Perpendicular giant magnetoresistance of multilayered Co/Cu nanowires*. Physical Review B, 1995. **51** (11): p. 7381.

[35]    Davis, D., *Electrodeposition of magnetic nanowires and nanotubes*, 2010: Lambert Academic Publishing

[36]    Lenz, J. and S. Edelstein, *Magnetic sensors and their applications*. IEEE Sensors Journal, 2006. **6** (3): p. 631-649.

[37]    Lenssen, K.M.H., et al., *Robust giant magnetoresistance sensors*. Sensors and Actuators A:Physical, 2000. **85** (1-3): p. 1-8.

[38]    Guedes, A., et al., *Improving Magnetic Field Detection Limits of Spin Valve Sensors Using Magnetic Flux Guide Concentrators*. IEEE Transactions on Magnetics, 2007. **43** (6): p. 2376-2378.

[39]    *GMR sensor catalog*, N. Corporation, Editor: Eden Prairie, MN.

[40]    Hahm, J.-i. and C.M. Lieber, *Direct ultrasensitive electrical detection of DNA and DNA sequence variations using nanowire nanosensors*. Nano Letters, 2003. **4** (1): p. 51-54.

[41] Liu, H., et al., *Polymeric nanowire chemical sensor.* Nano Letters, 2004. **4** (4): p. 671-675.

[42] Virji, S., et al., *Polyaniline nanofiber gas sensors: Examination of response mechanisms.* Nano Letters, 2004. **4** (3): p. 491-496.

[43] Dixon, R. *iSuppli: Silicon magnetic sensors head for big time.* 2010.

[44] Keiichi, N., *CPP-GMR technology for magnetic read heads of future high-density recording systems.* Journal of Magnetism and Magnetic Materials, 2009. **321** (6): p. 508-511.

[45] Prinz, G.A., *Magnetoelectronics.* Science, 1998. **282** (5394): p. 1660-1663.

[46] Holman, P., *Magnetoresistance (MR) transducers and how to use them as sensors,* 1st, Editor 2004, Honeywell.

[47] Vo-Dinh, T. and B. Cullum, *Biosensors and biochips: advances in biological and medical diagnostics.* Fresenius J Anal Chem, 2000. **366** (6-7): p. 540-551.

[48] Toner, M. and D. Irimia, *BLOOD-ON-A-CHIP.* Annual Review of Biomedical Engineering, 2005. 7(1): p. 77-103.

[49] Li, G., et al., *Spin valve sensors for ultrasensitive detection of superparamagnetic nanoparticles for biological applications.* Sensors and Actuators A:Physical, 2006. **126** (1): p. 98-106.

[50] Baselt, D.R., et al., *A biosensor based on magnetoresistance technology.* Biosensors and Bioelectronics, 1998. **13** (7-8): p. 731-739.

[51] Edelstein, R.L., et al., *The BARC biosensor applied to the detection of biological warfare agents.* Biosensors and Bioelectronics, 2000. **14** (10-11): p. 805-813.

[52] Rife, J.C., et al., *Design and performance of GMR sensors for the detection of magnetic microbeads in biosensors.* Sensors and Actuators A:Physical, 2003. **107** (3): p. 209-218.

[53] Megens, M. and M. Prins, *Magnetic biochips: a new option for sensitive diagnostics.* Journal of Magnetism and Magnetic Materials, 2005. **293**(1): p. 702-708.

[54] Wang, S.X. and L. Guanxiong, *Advances in giant magnetoresistance biosensors with magnetic nanoparticle Tags: Review and Outlook.* IEEE Transactions on Magnetics, 2008. **44** (7): p. 1687-1702.

[55] Graham, D.L., H.A. Ferreira, and P.P. Freitas, *Magnetoresistive-based biosensors and biochips.* Trends in Biotechnology, 2004. **22** (9): p. 455-462.

[56]    Eberbeck, D., et al., *Quantification of specific bindings of biomolecules by magnetorelaxometry.* Journal of Nanobiotechnology, 2008. **6** (1): p. 4.

[57]    Lankvelt, P., J. Nieuwenhuis, and H. Van Zon. 2008. *Microelectronic sensor device with an array of detection cells.* US patent application.

[58]    Li, Y., Y. Jing, and X. Yao. *Biomarkers identification and detection based on GMR sensor and sub 13 nm magnetic nanoparticles.* in *Engineering in Medicine and Biology Society.* 2009.

[59]    Chalmers, J.J., et al., *Flow through, immunomagnetic Cell Separation.* Biotechnology Progress, 1998. **14** (1): p. 141-148.

[60]    Tondra, M., et al., *Design of integrated microfluidic device for sorting magnetic beads in biological assays.* IEEE Transactions on Magnetics, 2001. **37** (4): p. 2621-2623.

[61]    Porter, M., J. Ni, and G.B. Dawson. 2004. *Method and apparatus for magnetoresistive monitoring of analytes in flow streams.* US patent application.

[62]    Pekas, N., M. Porter, and M. Tondra, *Giant magnetoresistance monitoring of magnetic picodroplets in an integrated microfluidic system.* Applied Physics Letters, 2004. **85**.

[63]    Evans-Pughe, C., *Close encounters of the magnetic kind [near field communications].* IEEE Reviews, 2005. **51**(5): p. 38-42.

[64]    *Health, Medicine & Nanobio*, in *Implants, Surgery and Coatings,* 2008, Observatory NANO.

[65]    Prutchi, D., P. Paul, and D. Genzer. 1995. *Apparatus and method for the control of an implantable medical device.* US patent application.

[66]    Digby, D., D. Wiggins, and R. Berthelsdat. 2008. *Implantable medical device comprising magnetic field detector.* US patent application.

[67]    Nordling, J., et al., *Giant Magnetoresistance Sensors. 1. Internally Calibrated Readout of Scanned Magnetic Arrays.* Analytical Chemistry, 2008. **80** (21): p. 7930-7939.

[68]    Sacha, M. 2008. *Switching structures for hearing aid.* US patent application.

[69]    Paunovic, M. and M. Schlesinger, *Fundamentals of electrochemical deposition.* Second ed 2006, Hoboken, New Jersey: Wiley.

[70]   Tafel, J., Phys. Chem., 1905. **50**: p. 641.

[71]   Shacham-Diamand, Y., V. Dubin, and M. Angyal, *Electroless copper deposition for ULSI.* Thin Solid Films, 1995. **262** (1-2): p. 93-103.

[72]   L.T, R., *A path: from electroplating through lithographic masks in electronics to LIGA in MEMS.* Electrochimica Acta, 1997. **42** (20-22): p. 2985-3005.

[73]   Hu, C.K. and J.M.E. Harper, *Copper interconnections and reliability.* Materials Chemistry and Physics, 1998. **52** (1): p. 5-16.

[74]   Andricacos, P.C. and L.T. Romankiw, *Magnetically soft materials in data storage: Their properties and electrochemistry,* in *Advances in Electrochemical Science and Engineering*2008, Wiley-VCH Verlag GmbH. p. 227-321.

[75]   Parkin, S.S.P., Z.G. Li, and D.J. Smith, *Giant magnetoresistance in antiferromagnetic Co/Cu multilayers.* Applied Physics Letters, 1991. **58** (23): p. 2710-2712.

[76]   Schlesinger, M., *Electroplating* in *Electrochemistry Encyclopedia* 2002.

[77]   Reid, J. *Introduction to Cu electroplating.* Semiconductor Online, 2000.

[78]   Davis, D., *Electrodeposition of multilayered nanostructures for giant magnetoresistance and thermoelectric applications,* 2007, Louisiana State University: Baton Rouge, LA.

[79]   Brebber, A., *Ph.D Dissertation,* 1939, University of Maryland.

[80]   Cohen, U., F.B. Koch, and R. Sard, *Electroplating of Cyclic Multilayered Alloy (CMA) Coatings.* Journal of The Electrochemical Society, 1983. **130** (10): p. 1987-1995.

[81]   Yahalom, J. and O. Zadok, *Formation of composition-modulated alloys by electrodeposition.* Journal of Materials Science, 1987. **22**(2): p. 499-503.

[82]   Shakya, P., B. Cox, and D. Davis, *Giant magnetoresistance and coercivity of electrodeposited multilayered FeCoNi/Cu and CrFeCoNi/Cu.* Journal of Magnetism and Magnetic Materials, 2012. **324** (4): p. 453-459.

[83]   Kimura, T., T. Sato, and Y. Otani, *Temperature evolution of spin relaxation in a NiFe/Cu lateral spin valve.* Physical Review Letters, 2008. **100**(6): p. 066602.

[84]   Tracton, A., in *Coatings Technology: Fundamentals, Testing and Processing Techniques,* 2006, CRC Press.

[85]    Satas, D. and A. Tracton, *Coatings Technology Handbook*. 2nd ed2000: Marcel Dekker.

[86]    Pike, G.E. and C.H. Seager, *Percolation and conductivity: A computer study. I.* Physical Review B, 1974. **10** (4): p. 1421-1434.

# PUBLICATIONS

Cox, B., et al., *GMR sensors: technologies and medical applications* Recent Patents on Nanomedicine, 2011. **1** (2): p. 130-137.

Shakya, P., B. Cox, and D. Davis, *Giant magnetoresistance and coercivity of electrodeposited multilayered FeCoNi/Cu and CrFeCoNi/Cu.* Journal of Magnetism and Magnetic Materials, 2012. **324** (4): p. 453-459.

Cox, B. and N. Crews, *Nanowire GMR thin films for magnetic sensors*, in *Nanotech Conference & Expo 2012*, 2012 Santa Clara, CA.

Cox, B. and N. Crews, *Creating magnetic sensors from nanowire arrays.* Sensors and Actuators A: Physical, 2012.: Submitted